

Studies of Evolved Stars with a Mid-Infrared Interferometer

by

Everett Arthur Lipman

B.A. (University of Chicago) 1991
M.A. (University of California at Berkeley) 1993

A dissertation submitted in partial satisfaction of the
requirements for the degree of
Doctor of Philosophy

in

Physics

in the

GRADUATE DIVISION
of the
UNIVERSITY of CALIFORNIA at BERKELEY

Committee in charge:

Professor Charles H. Townes, Co-Chair
Dr. William C. Danchi, Co-Chair
Professor Sumner P. Davis
Professor William J. Welch

Fall 1998

The dissertation of Everett Arthur Lipman is approved:

Chris H. Townes Sept. 16, 1998
Co-Chair Date

William C. Dandli Sept. 16, 1998
Co-Chair Date

Sumner P. Davis Sept. 16, 1998
Date

Wm Q Welch Sept. 17, 1998
Date

University of California at Berkeley

Fall 1998

Studies of Evolved Stars with a Mid-Infrared Interferometer

Copyright © 1998, 1999

by

Everett Arthur Lipman

Abstract

Studies of Evolved Stars with a Mid-Infrared Interferometer

by

Everett Arthur Lipman

Doctor of Philosophy in Physics

University of California at Berkeley

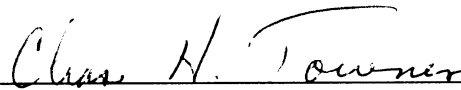
Professor Charles H. Townes, Co-Chair

Dr. William C. Danchi, Co-Chair

The University of California at Berkeley Infrared Spatial Interferometer (ISI) is a two-element stellar interferometer which employs heterodyne detection to gather starlight in the mid-infrared (9–12 μm) wavelength range. Each element of the ISI is a 1.65 m telescope, equipped with appropriate optical and detection systems. Successful operation of the ISI requires that the star image in each telescope be precisely centered on a signal detector. In order to accomplish this, near-infrared (2 μm) guiding and tip-tilt correction systems have been built and incorporated into the ISI telescopes. Each system uses an InSb infrared camera to determine small errors in the position of the source image. Slower fluctuations in position, occurring over a period of a few seconds, are corrected by adjusting the telescope tracking. Fast fluctuations are caused by the atmosphere, and are removed using a controllable tilting mirror. A significant improvement in signal quality, provided by this fast tip-tilt correction, is demonstrated by data taken on the supergiant α Orionis.

To be suitable for study by the ISI, a source must have substantial mid-infrared flux. Evolved stars, typically very luminous and surrounded by one or more shells of dust, are the most common type of target for the ISI. The new guiding system enables the ISI to track these objects, which, because of their dust shells, often have insufficient visible flux for a guiding system using a silicon detector. During the 1997 observing season, the evolved stars IRC +10011 and IRC +10420 were observed with the ISI. Fringe visibility data and mid-infrared spectra for these two sources were compared with

theoretical values generated by radiative transfer models of the stellar surroundings. IRC +10011 data were well fit by a spherical dust shell with inner radius $0.033''$ and a density profile falling off as $r^{-1.5}$, slightly slower than the r^{-2} expected for uniform dust outflow. IRC +10420 data could only be fit by a shell with a much slower drop in density, proportional to $r^{-0.5}$. This shell had an inner radius of $0.120''$. These observations will help to increase our understanding of the processes which govern the late stages of stellar evolution.



Professor Charles H. Townes
Dissertation Committee Co-Chair



Dr. William C. Danchi
Dissertation Committee Co-Chair

To my parents

Contents

List of Figures	vi
List of Tables	viii
1 Introduction	1
1.1 Limitations of Telescopic Imaging	1
1.2 Evolved Stars	5
2 Stellar Interferometry	8
2.1 History	8
2.2 Theoretical Background	10
2.2.1 Coherence Length and Starlight	10
2.2.2 Interference Fringes and Fringe Visibility	12
2.2.3 Fringe Visibility in Two Dimensions	16
2.2.4 Interpretation of Visibility Curves	20
2.2.5 Atmospheric Fluctuations	23
2.3 Radio Interferometry, Heterodyne Detection, and the ISI	26
3 The U.C. Berkeley Infrared Spatial Interferometer	34
3.1 Optical System	35
3.2 Fringe Detection	40
3.2.1 Heterodyne Signal Detection	40
3.2.2 Phase Locking	43
3.2.3 Signal Combination	45
3.2.4 Data Acquisition and Storage	48
3.3 Telescope Control	48
3.4 Telescope Guiding and Tip-Tilt Correction	50
3.4.1 Guiding System Hardware	53
3.4.2 Guider Camera Sensitivity	60
3.4.3 Guiding System Software	70
3.4.4 Guiding System Performance and Data Quality Improvement . .	82

4	Reduction of ISI Data	86
4.1	Obtaining Fringe Visibility Measurements from ISI Data	86
4.1.1	Theory	86
4.1.2	Visibility Values and Calibration	88
4.1.3	Sources of Uncertainty	92
4.2	Modeling and Source Image Reconstruction	97
4.2.1	Direct Inversion	97
4.2.2	Radiative Transfer Modeling	98
5	IRC +10011 and IRC +10420	102
5.1	IRC +10011	103
5.1.1	Background	103
5.1.2	ISI Results and Models	105
5.1.3	Discussion of Results	111
5.2	IRC +10420	112
5.2.1	Background	112
5.2.2	ISI Results and Models	114
5.2.3	Discussion of Results	119
6	Future Directions	122
6.1	Improvements to the ISI	122
6.2	Optical and Infrared Interferometry	123
A	1997 Results on CIT 6	125
B	ISI Guiding System Manual	129
B.1	Startup and Shutdown Procedures	130
B.2	Panic Abatement Guide	132
B.3	Camera Calibration Procedure	134
B.4	Pumping on the Liquid Nitrogen for Weak Star Observations	136
B.5	Camera Dewar Evacuation	138
B.6	Control Program and Network Interface	139
B.6.1	Source Code Description	139
B.6.2	Network Interface General Information	141
B.6.3	Picture Request	143
B.6.4	Trackball Commands	144
B.6.5	Guider Commands	147
B.6.6	Guider PC Hardware Configuration	154
	Bibliography	155
	Colophon	165

List of Figures

1.1	Illustration of small angles	3
1.2	Limitations of telescopic imaging	4
1.3	Evolution of a star similar to the Sun	6
2.1	Power spectrum of a finite harmonic pulse	11
2.2	Interference fringe visibility	13
2.3	Brightness distribution observed with an interferometer	17
2.4	Examples of visibility curves	21
2.5	Fringe signal power spectra	23
2.6	Fried coherence parameter	24
2.7	Star images	26
2.8	Heterodyne stellar interferometer	28
2.9	Schematic comparison between direct and heterodyne detection	29
3.1	Photograph of the ISI	35
3.2	ISI trailer diagram	36
3.3	Schwarzschild optical system	36
3.4	Dichroic beamsplitter, camera, and signal detector	37
3.5	Telescope 1 optics table	38
3.6	Telescope 2 optics table	39
3.7	ISI detection system block diagram	44
3.8	Correlator signal path	46
3.9	ISI computer configuration	49
3.10	ISI signal detector and beam	50
3.11	Atmospheric index of refraction	52
3.12	290 K blackbody distribution	54
3.13	Guider camera optical system	55
3.14	Spot diagram for guider lens	57
3.15	Guiding system configuration	58
3.16	Tip-tilt actuator	59
3.17	Tip-tilt range on the sky	60
3.18	Image of α Orionis	65
3.19	Background measurements on the AE4128 camera	66

3.20	Image of an $m_K = 3$ star	69
3.21	Histogram of $m_K = 3$ star image	69
3.22	The yguider interface	71
3.23	Guider camera field of view	73
3.24	Star search flow chart	76
3.25	Tip-tilt loop flow chart	79
3.26	Star detection algorithm	80
3.27	Spiral search	81
3.28	Tip-tilt tests on α Orionis	83
3.29	α Orionis visibility data from 1988–1994	85
3.30	α Orionis visibility data from 1997	85
4.1	Visibility curve for a $0.0207''$ uniform disk	89
4.2	Data points for IRC +10011.	91
4.3	Corrected data points for IRC +10011.	92
4.4	Visibility curve for IRC +10011.	93
4.5	Visibility drop at short baselines	95
4.6	Illustration of the radiative transfer model	99
5.1	IRC +10011 mid-infrared spectra	104
5.2	IRC +10011 1997 visibility data	105
5.3	IRC +10011 best-fit model	107
5.4	IRC +10011 model image	108
5.5	IRC +10011 best uniform outflow model	109
5.6	IRC +10011 spectral tail model	110
5.7	IRC +10420 mid-infrared spectra	113
5.8	IRC +10420 1997 visibility data	115
5.9	Raw and valid data points for IRC +10420	116
5.10	Fringe power histogram for IRC +10420	117
5.11	IRC +10420 best-fit model	118
5.12	IRC +10420 best uniform outflow model	119
A.1	CIT 6 data points	126
A.2	CIT 6 fringe visibility values	126
A.3	CIT 6 data with fit and $11\ \mu\text{m}$ intensity profile	128

List of Tables

3.1	Photon fluxes from a sample of ISI sources	52
3.2	Amber AE4128 camera characteristics	53
3.3	Guider camera optical system specifications	56
3.4	Photons per pixel per second from some ISI targets	62
3.5	Magnitude equivalents of the thermal background noise	63
3.6	Magnitude equivalents of measured total background noise	68
3.7	Results from tip-tilt testing	83
5.1	Properties of IRC +10011 and IRC +10420.	102
5.2	Position angles for IRC +10011 and IRC +10420.	103
5.3	Visibility values for IRC +10011.	106
5.4	Visibility values for IRC +10420.	115

Acknowledgements

During the course of my formal and informal studies, a number of people have provided me with assistance in one form or another—sometimes in many forms. These people have enriched my life and enabled me to reach this point.

I would like to begin by thanking my parents, who have given me every sort of support possible, and who, along with my brother Andrew, have encouraged me from the day I began my education 24 years ago.

The West Lafayette, Indiana school system, in particular my mathematics and science teachers William Trujillo, Robert Bryant, James Guy, and Cherie Lehman, provided me with a solid background which I still find reason to be grateful for on a daily basis. I would also like to thank Evan, Mike, and Bill from the West Lafayette Radio Shack for their help during the early stages of my experimental physics training.

While I was at the University of Chicago, Professors Albert Crewe, James Cronin, and Hellmut Fritzsche advised me and made important contributions to my background in physics.

One of the pleasures of my education has been interacting with and learning from other physics students. My friends Lorin Benedict, Chris Bowers, Charlie Hansen, Matt McCluskey, David Norris, David Reichman, Seth Rosenberg, and Kelly Truelove have all enhanced my understanding of the subject. Mark Arndt has given me useful advice regarding my transition to biological physics as well as my tuning during “It’s Only a Paper Moon.”

My first research experience at Berkeley was with Professor Roger Falcone’s short-pulse laser group. My work with Professor Falcone, Tom Donnelly, Ernie Glover, Martin Hofer and Alan Sullivan provided me with many important experimental skills.

A number of Physics and Astronomy faculty members have been helpful to me during graduate school. I would like to thank Professors Lars Bildsten and James Graham for serving on my candidacy exam committee, and Professor Jack Welch for serving on my dissertation committee. Professor Daniel Rokhsar provided me with valuable advice during my job search.

I owe a special debt of gratitude to Professor Sumner Davis, who, in addition to serving on my candidacy exam and dissertation committees, has gone out of his way to give me advice, support, and encouragement the entire time I have been at Berkeley.

I would like to thank Anne Takizawa, Donna Sakima, Marnie McElhiney, and Dianna Jacobs for the help they have given me with administrative tasks during graduate school.

It has been a pleasure interacting with the people in the Infrared Spatial Interferometer research group on a daily basis over the last 4 years. I am grateful to have had the opportunity to work with Professor Charles Townes, who has been very generous with his time and has set an excellent example of how to be a scientist. His persistence, industry, and ability in dealing with people have all been inspiring. Bill Danchi has given me important guidance, especially during the initial stages of the guiding system construction. Manfred Bester provided me with many hours of patient explanation of the ISI. His help and hard work on the instrument, both before and during our numerous trips to Mt. Wilson Observatory, were essential to the success of my project. Michael Johnson shared with me his knowledge of the instrument and keen experimental insight during the year which he spent working with our group.

I am grateful to David Hale for his tireless efforts in running the ISI, and for his company during many long nights of observing. Sean Hoss, in addition to being among the best of the 15 roommates I had during graduate school, was a pleasure to work with, both in Berkeley and at Mt. Wilson. I very much appreciate his willingness to drive across the country so that I could use my last week in California to finish this work.

John Monnier has shared with me his knowledge of stellar modeling and ISI data interpretation, which has been very helpful over the last few months. Peter Tuthill has given me useful suggestions, interesting additions to my vocabulary, and a congenial office atmosphere. Walt Fitelson designed and built the amplifiers for the tip-tilt system, gave me a lot of good advice about the instrument, and was a real pleasure to work with. Jerry Hudson shared with me the task of administering the ISI computers, and was a consummate team player in our research group. Robert Ullrich designed the mounts for the tip-tilt mirrors. These mounts were machined by Terry McDonald, whose excellent craftsmanship can be found throughout the guiding system and the rest of the ISI. I have also enjoyed working with Paul Barale, Jeff Cobb, Kyle McElroy, Jerry Penegor, and Ed Wishnow during my time at the Space Sciences Lab, and with our French collaborators Bruno Lopez, Djamel Mekarnia, and Yves Rabbia, both in Berkeley and at Mt. Wilson.

The CDS/SIMBAD astronomical database and the NASA ADS Abstract Ser-

vice have both been very useful to me during the course of my work in astrophysics.

Financial support for my graduate work has been provided by the Office of Naval Research (grant N00014-93-0775) and by a National Science Foundation graduate fellowship. The U.C. Berkeley Infrared Spatial Interferometer project in general has been funded by other grants from these two agencies. I hope that during the course of my career I will be able to provide a return, in the form of new and useful knowledge, on the investment which the taxpayers of the United States have made in my education.

Chapter 1

Introduction

The clear night sky is fascinating to behold. At a remote site, unpolluted by artificial lighting, one can see as many as a few thousand stars. These points of light, with their many colors and brightnesses, evoke an undeniable desire for more knowledge of their nature. During the last few hundred years, mankind has been turning ever more powerful optical instruments toward the sky in order to discover where the stars are, what they are made of, how big they are, and ultimately, how they live and die.

This dissertation describes observations of evolved stars which were made with the U.C. Berkeley Infrared Spatial Interferometer (ISI). The ISI is a special combination of two telescopes which is able to obtain information with very high angular resolution in the mid-infrared region of the electromagnetic spectrum. This range of wavelengths, around $10\ \mu\text{m}$, is where the thermal radiation from room-temperature objects is at its maximum. Evolved stars, those in the late stages of the stellar life cycle, are often surrounded by shells of relatively cool dust, and thus make ideal targets for study with the ISI.

1.1 Limitations of Telescopic Imaging

There are two primary reasons to use optical instruments to study the stars. The first is to gather more light. A typical dark-adapted human pupil is only 5 mm in diameter. By using binoculars with 50 mm objective lenses, one increases the amount of light in the retinal image by a factor of $(50/5)^2 = 100$. For any given detector (the cells of the retina, or a silicon charge-coupled detector, for example), increasing the amount of light

gathered will increase the number of objects available for study, and improve the signal-to-noise ratio on those already visible. Because of this advantage, larger telescopes are preferable, all other factors being equal.

The second reason to use optical instruments is to improve resolution. Because of the wave nature of light, any point in an object being viewed will be mapped, even in a perfect optical instrument, to a diffraction pattern in the image. In the common case of an instrument with a circular entrance pupil, this will be the Airy pattern (pictured in Fig. 1.2). The result of this effect is a fine-scale blurring, since distinct points with small separations in the object will become overlapping disks with faint rings surrounding them in the image.

The light intensity of the central maximum (known as the Airy disk) of the Airy pattern drops to zero at an angular distance of $1.22\lambda/D$ radians from the center,¹ where λ is the wavelength of the light forming the image, and D is the diameter of the instrument's entrance pupil. The diffraction-limited resolution angle of a telescope is usually given as this same angle, $1.22\lambda/D$. This is the Rayleigh criterion, which states that the smallest angle which can separate two resolved points in an object is that angle for which the edge (first intensity null) of the Airy disk due to one point in the image will coincide with the center of the other disk. Although this definition is somewhat arbitrary, it provides a useful measure for comparing optical systems. Using this criterion, the resolution of an eye with a 5 mm pupil, viewing green light,² would be about 30 arc seconds ($''$), where $1''$ is $1/3600$ of a degree of arc. By comparison, 20/20 vision is defined as the ability to read letters which are $300''$ tall with $60''$ features. At a distance of 17 mm, the approximate focal length of the eye, $30''$ corresponds to $2.5 \mu\text{m}$. Notably, the light-sensitive rod and cone cells in the retina have collecting areas of approximately 1 and $4 \mu\text{m}^2$, respectively. Thus these cells are just small enough to take advantage of the best possible resolution which the eye can have.

While a few arc seconds might seem to be a very small angle, and not a serious limitation to useful resolution, the enormous distances to the stars result in

¹The light intensity in the Airy pattern has the functional form $(\frac{J_1(\xi)}{\xi})^2$, where J_1 is a Bessel function of first order, and $\xi \equiv (\frac{\pi}{\lambda})D \sin \theta$. The first zero of $J_1(\xi)$ occurs at $\xi = 3.832$, so that $3.832 = (\frac{\pi}{\lambda})D \sin \theta_0$, or $D \sin \theta_0 = 1.22\lambda$. The angular distance from the center of the pattern, θ , is normally extremely small (around 5×10^{-7} rad at optical wavelengths with a 1 m aperture), so $\theta_0 \approx 1.22\lambda/D$. A derivation of this diffraction pattern is given by Lipson and Tammhauser [59].

²The eye's sensitivity peaks near the center of the visible spectrum, at a wavelength which corresponds to green light.

their having minuscule angular diameters. Figure 1.1 illustrates the sort of angle which must be resolved in order to see a star as a disk rather than a point of light. Even the

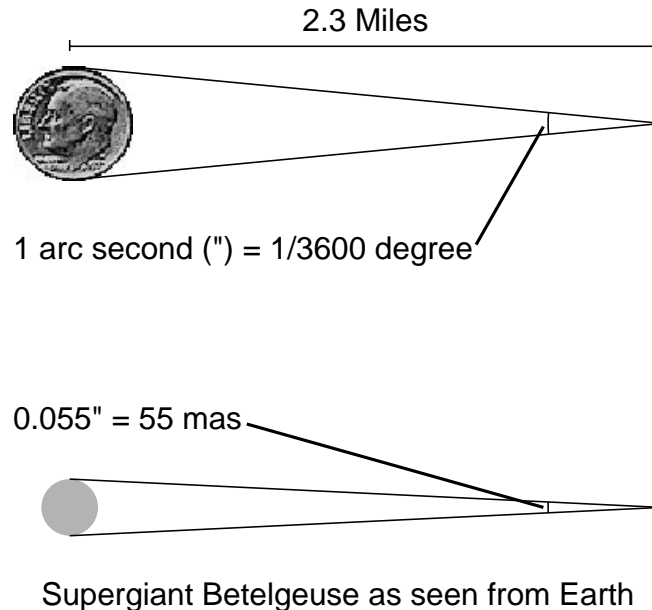


Figure 1.1: Illustration of small angles. As shown in the top part of the figure, 1" is the angle subtended by a dime at 2.3 miles. Betelgeuse (α Orionis), a star with one of the largest angular diameters, subtends 55 thousandths of an arc second as seen from Earth.

supergiant Betelgeuse, which is significantly larger than Jupiter's orbit, subtends only 55 mas (thousandths of an arc second) as seen from Earth. Using the Rayleigh criterion, we can quickly compute that in order to resolve, using visible light, two points with the angular separation θ of Betelgeuse's diameter, we would need a telescope with diameter $D \geq 1.22\lambda/\theta = 2.5$ m.

Although there are a number of such telescopes, long before we reach this size, another limitation comes into play. For any telescope with a diameter greater than about 25 cm, distortion of the visible-light image by the atmosphere is more of a limitation than diffraction. This situation is illustrated in Fig. 1.2. Recently, adaptive optics systems have been developed which correct for atmospheric fluctuations and allow large telescopes to enjoy nearly diffraction-limited performance.

Although atmospheric turbulence can be avoided by launching a telescope into orbit, or corrected with adaptive optics, diffraction presents a more fundamental

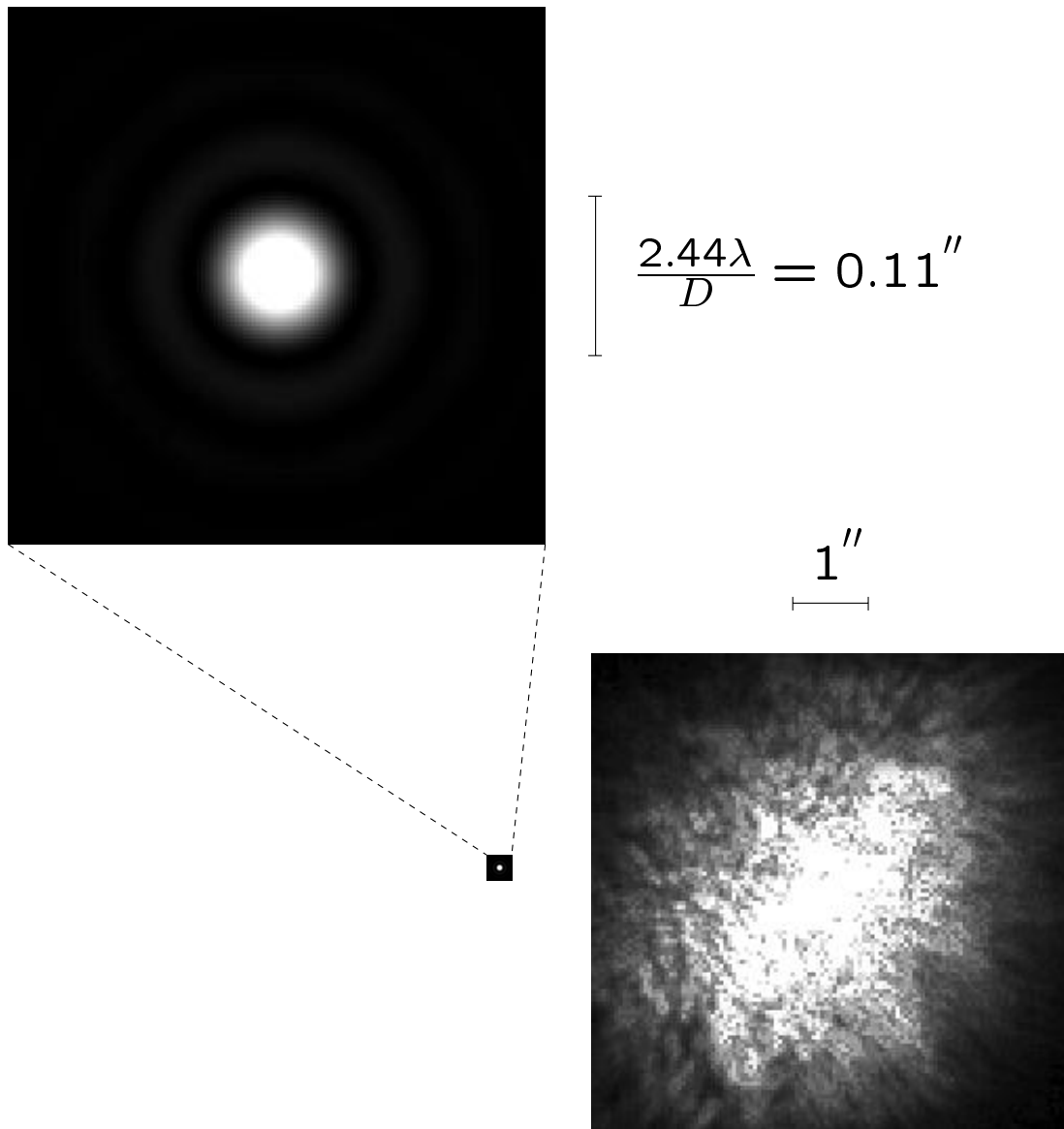


Figure 1.2: Limitations of telescopic imaging. At the top is the diffraction disk which would result from the imaging of a perfect point source in $2.2\ \mu\text{m}$ light by a 10 m telescope. Below, the diffraction disk is reproduced, to scale, next to a real image of a binary star taken at $2.2\ \mu\text{m}$ on the 10 m Keck telescope. For any telescope with an aperture larger than about 25 cm, blurring of the visible-light image due to the atmosphere is more of a limitation than diffraction.

problem. It is not currently possible to build telescopes much larger than 10 m in diameter. Because of this engineering limitation, we must use other methods in order to obtain resolutions higher than $0.01''$.

It was demonstrated late in the nineteenth century that by using optical interference, one can, to some extent, overcome both factors which limit the resolution of ordinary telescopes. This technique of stellar interferometry, described in chapter 2, has been used since the early 1920s to enhance our understanding of the stars. The ISI is one of a number of interferometers presently obtaining information about stars and their surroundings which would not otherwise be available.

1.2 Evolved Stars

As was mentioned earlier, evolved stars, with their shells of relatively cool dust, are ideal targets of observation for the ISI. Such stars are also interesting from a theoretical point of view, since our understanding of the late stages of stellar evolution is still incomplete.

Figure 1.3 illustrates the life cycle of a typical star, such as our own Sun. A complete qualitative description of this life cycle can be found in *The Physical Universe* by Shu [83], and a more technical treatment is given by Hansen and Kawaler in *Stellar Interiors* [35]. In the figure, known as a Hertzsprung-Russell diagram, the luminosity of the star (in units of solar luminosity L_{\odot}) is plotted against its effective temperature. The effective temperature is the temperature which a blackbody of the star's size would need to have in order to match the luminosity of the star. When plotted on this diagram, most stars fall within a band known as the main sequence. Position in the main sequence is determined by stellar mass.

Most of the life of a star is spent in the main sequence, as the initial supply of hydrogen is slowly fused into helium at the star's core. When this supply of hydrogen runs out, the core will contract, and fusion will begin in a shell around the helium ash. Helium produced by this "shell burning" accumulates in the core, the additional mass causing further contraction. This contraction will increase the gravity at the surface of the core, and the temperature and density of the shell will rise, enhancing the fusion reaction. Consequently, the star begins to expand, and its surface temperature drops, since the increased luminosity is not sufficient to maintain the larger surface area at the original temperature. These changes can be seen on the diagram as the initial departure

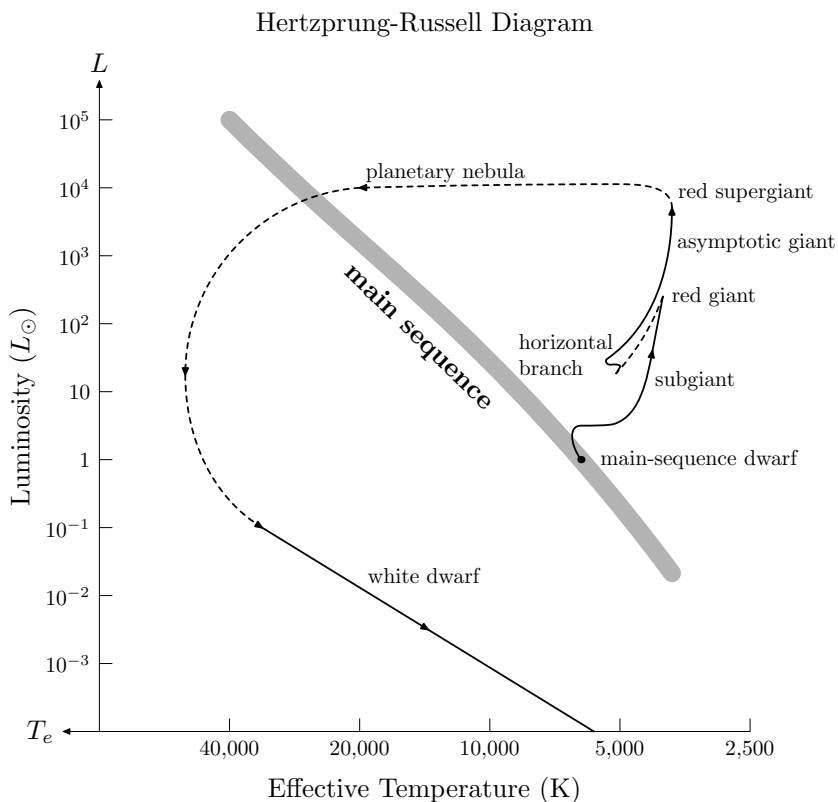


Figure 1.3: Evolution of a star similar to the Sun (after Shu [83]). The star spends most of its life burning hydrogen on the main sequence. After the hydrogen is exhausted in the star’s core, various changes occur which lead, in the end, to the star becoming a slowly cooling white dwarf. The dashed sections of the path are still poorly understood.

from the main sequence and subsequent horizontal movement as the star’s surface cools. At this stage, the star is known as a subgiant. Eventually, the free electrons in the star’s core become degenerate, and the extremely high gravity at the center of the star further stokes the reaction in the shell. The large energy output from the shell causes the star to ascend the red giant branch as its luminosity grows.

At the tip of the red giant branch, the core temperature in the star reaches the point where helium can be fused into carbon. When this “helium flash” occurs, it is thought that the hydrogen-burning shell is temporarily disrupted, causing the star’s luminosity to drop as it descends to the horizontal branch, which is characterized by a stable helium-burning core surrounded by a hydrogen-burning shell. After a period of time spent on the horizontal branch, the fuel at the star’s core is once again exhausted,

and shell burning begins, though this time in a helium shell. In a process similar to the ascent of the red giant branch, the star becomes an asymptotic giant, and possibly a red supergiant. Finally, the star will shed its envelope into a planetary nebula. The electron-degenerate core of the star, its heat production having ceased, will become a slowly cooling white dwarf.

As is indicated by the dashed lines in Fig. 1.3, some stages of the stellar life cycle are still poorly understood. During the ascents of the red giant and asymptotic giant branches, a star's envelope becomes distended, and matter can be ejected into the interstellar medium. The process by which this mass is lost is not yet well characterized, although asymptotic giant branch (AGB) stars are seen to be surrounded by dust shells, most of which are observed to have outward velocities. Both a star's position on the horizontal branch and eventual fate as an asymptotic giant depend on its mass. A star which manages to retain more than about $1.4 M_{\odot}$ (1.4 Solar masses, the "Chandrasekhar Limit") will become a neutron star, and possibly a supernova, instead of decaying to the white dwarf state. Before we can complete a theoretical description of stellar evolution and the composition of the interstellar medium, we must understand mass loss from evolved stars.

AGB stars and their dust shells are the most common objects observed with the ISI, and the high-resolution information gleaned from ISI data can be combined with spectroscopic data to characterize the sizes, shapes, densities, outflow velocities, and compositions of stellar dust shells. This new information is contributing to our understanding of the mass-loss processes which drive the late stages of stellar evolution.

Chapter 2

Stellar Interferometry

2.1 History

The use of optical interference to measure astronomical objects was first suggested by Fizeau in 1868 [29]. After an unsuccessful French attempt to make such a measurement, Michelson resurrected the idea in 1890 [63], and in 1891, he published the results of his interferometric measurements of the angular sizes of the moons of Jupiter [64]. Despite this initial success, Michelson did not attempt to measure stellar angular diameters for almost 20 years. At the time of Michelson's initial measurement, it was thought, based on the assumption that other stars were similar to the Sun, that stellar angular diameters could not be measured with an instrument of practical (at the time) size.

After the turn of the century, better understanding of blackbody radiation and stellar effective temperatures enabled more accurate theoretical predictions of angular diameters. In a 1920 publication [28], Eddington predicted a diameter of $0.051''$ for Betelgeuse (α Orionis), and stated that

Probably the greatest need of stellar astronomy at the present day, in order to make sure that our theoretical deductions are starting on the right lines, is some means of measuring the apparent angular diameters of stars. At present we can calculate them approximately from theory, but there is no observational check.

By the time of this publication, Michelson and Pease were already working at Mt. Wilson Observatory on the measurement of the angular diameter of Betelgeuse. Their result,

which was published in 1921 [65], was an angular diameter of $0.047'' \pm 10\%$, in agreement with Eddington's prediction. Pease attempted to continue the work at Mt. Wilson with a larger instrument, but the requirement of keeping the optical paths in the interferometer constant to within a few wavelengths of light proved insurmountable with the technology of the time. This problem essentially halted progress in optical interferometry for the next 30 years.

In 1956, Hanbury Brown and Twiss [19] realized that intensity correlations in the light impinging on two separated telescopes can be used to obtain stellar angular diameters. Intensity fluctuations have a characteristic time equal to the coherence time of the light being measured, thus the arrival times of various parts of the stellar wavefront at the photoelectric detector need only be matched to within a reasonable fraction of the coherence time. This allows the use of large light collectors whose optical quality can be relatively poor, and eliminates the effect of atmospheric fluctuations. In practice, intensity interferometers have very narrow bandwidths (on the order of 100 MHz) so that the detection electronics can follow the intensity fluctuations. Because of the narrow bandwidth and correspondingly large coherence length, an intensity interferometer is not subject to the problem which vexed Pease. Although this technique is only viable for the brightest stars, eventually a number of valuable results were obtained (Hanbury Brown *et al.* [18]).

The development of optical and electronic technology has spurred a resurgence of interest in amplitude interferometry over the last 25 years, and there are now a number of successful interferometers operating in the world. A collection of papers edited by Lawson [54] includes descriptions of these instruments, as well as early work in the field.

Although little progress was made in optical amplitude interferometry between the time of Pease and the recent past, many successful applications and extensions of stellar interferometry were made at radio wavelengths, beginning in 1946 with the work of Ryle and Vonberg [82]. Radio interferometry will be discussed in §2.3.

The U.C. Berkeley Infrared Spatial Interferometer has its origins both in optical and radio interferometry, and has pioneered long-baseline interferometric work in the mid-infrared (9–12 μm) wavelength range.

2.2 Theoretical Background

2.2.1 Coherence Length and Starlight

At first, it might seem counterintuitive to use an interferometer to study light from an incoherent, broad-band source such as a star. If one combines the light from two flashlights, the result will still be uniform illumination, with the intensity equal to the sum of the intensities of the two sources. Likewise, sunlight combined by reflection does not normally exhibit interference effects. There are, however, situations where interference effects are created by “white” light. An example of such a situation is the occurrence of brilliant colors in soap bubbles and thin films of oil floating on water. The condition necessary in all systems producing interference fringes from light is that the paths taken from the source to the point of interference by the interfering beams of light must be matched to within a distance l_c , the *coherence length*. For sunlight, $l_c \approx 1 \mu\text{m}$, so in order to see interference, we must have a pathlength difference, such as a round trip across the thickness of a soap bubble, of not much more than $1 \mu\text{m}$.

The light from a flashlight or a star is produced in the form of many photons, each resulting from the transition of a thermally-excited electron. Unlike photons from a laser, these are correlated neither in phase nor in frequency. We can represent a photon with an idealized harmonic pulse as shown in Fig. 2.1. This pulse has the following form:

$$f(t) = \begin{cases} \cos(2\pi\nu_0 t) & -\frac{1}{2}\tau < t < \frac{1}{2}\tau \\ 0 & \text{elsewhere,} \end{cases} \quad (2.1)$$

where τ , the time over which the pulse maintains a continuous phase, is called the *coherence time*. If we were to try to produce an interference pattern with many pulses of this form, for example by passing them through a beam splitter and recombining them on a screen, clearly the two parts of a split pulse would need to arrive at the screen with a relative delay of no more than τ in order for interference to occur. The coherence length l_c is defined as the distance over which a photon will travel during its coherence time, so

$$l_c = c\tau, \quad (2.2)$$

where c is the speed of light.

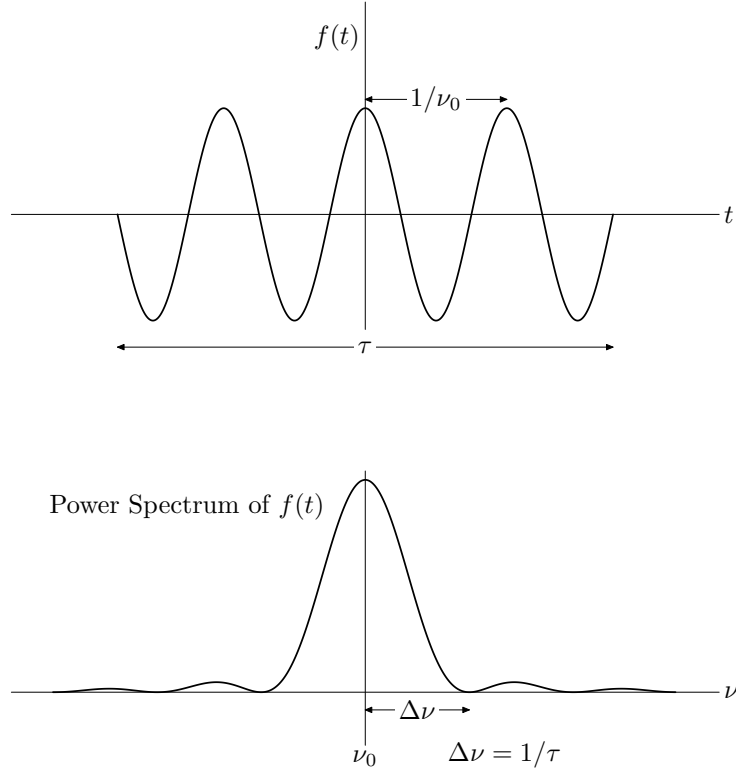


Figure 2.1: Power spectrum of a finite harmonic pulse. Pictured here is a harmonic pulse with duration τ and frequency ν_0 . The power spectrum of the pulse has two identical components. One, shown here, is centered about ν_0 , and the other is centered about $-\nu_0$. The first maximum in the power spectrum of the pulse has a half-width at its base of $\Delta\nu = 1/\tau$.

We can relate τ , and hence l_c , to the bandwidth of the light by examining the power spectrum of the pulse (Bracewell [17]), which is:

$$g(\nu) = A \operatorname{sinc}^2 [\pi(\nu \pm \nu_0)\tau], \quad (2.3)$$

where $\operatorname{sinc}(x) \equiv \sin(x)/x$, and A is a normalization constant, chosen such that the power of the pulse is the same in the time and frequency domains. The half-width $\Delta\nu$ of the central maximum of $g(\nu)$ at its base (Fig. 2.1) is usually chosen to represent the spread of frequencies contained in the pulse (as, for example, in Born & Wolf [14]). From (2.3) we can see that $g(\nu) = 0$ when

$$\Delta\nu = \nu - \nu_0 = 1/\tau. \quad (2.4)$$

Substituting from (2.2), we have

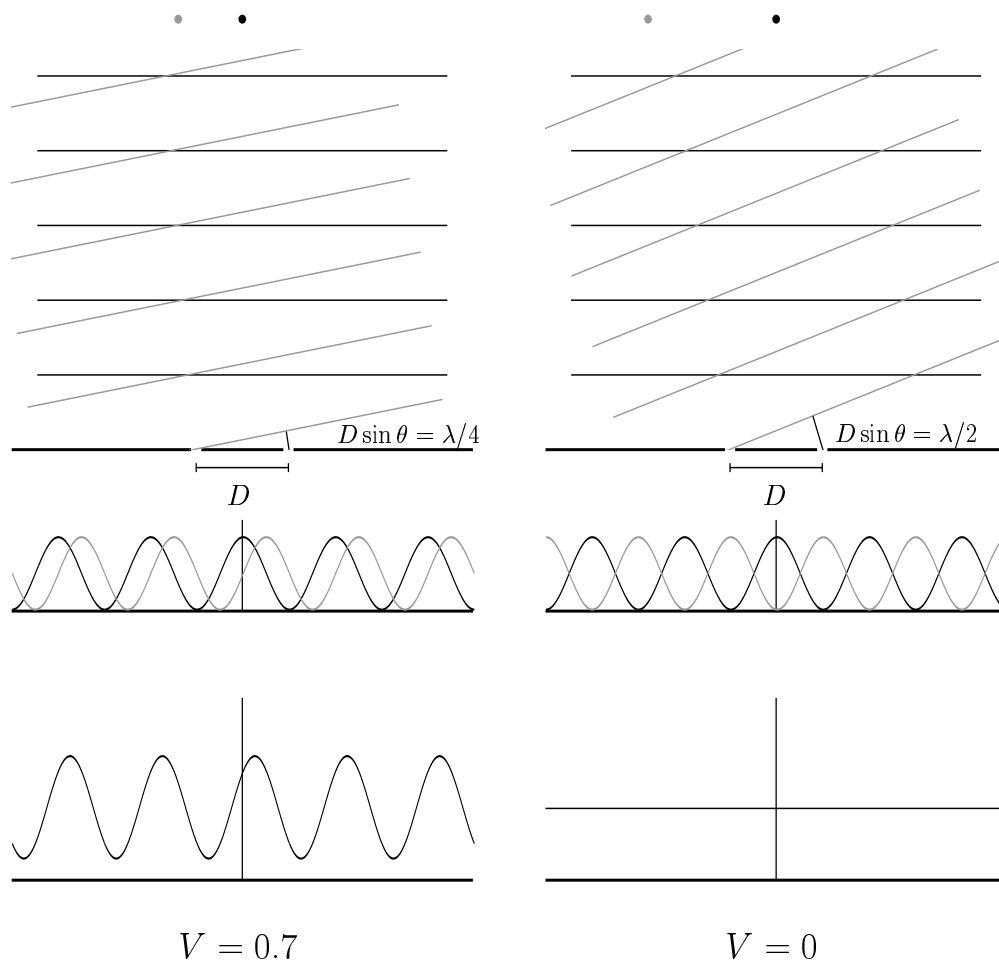
$$l_c = c\tau = c/\Delta\nu. \quad (2.5)$$

Thus there is an inverse relationship between the bandwidth and coherence length of light from a given source. For visible sunlight, which contains wavelengths between 400 and 700 nm, $\Delta\nu \approx 3 \times 10^{14}$ Hz, so $l_c \approx 1 \mu\text{m}$. Typical “monochromatic” light, as from a multimode laser with a bandwidth of 100 MHz, would have a coherence length $l_c = 3$ m.

As will be described in §2.2.2, a simple stellar interferometer consists of two separated telescopes. The light collected by the telescopes is combined to produce fringes, and from the contrast (also known as “fringe visibility”) of these fringes, we can recover high resolution information about the brightness distribution of the source on the sky. In order to obtain fringes and make an accurate measurement of the visibility, the interferometer must ensure that the paths taken by a stellar wavefront through the two telescopes to the point of combination are equal to within a fraction of l_c . This is accomplished by placing a variable delay in one of the arms of the interferometer, as pictured in Fig. 2.8. The detection bandwidth of the ISI is about 6 GHz ($l_c \approx 5$ cm), so the delay line, which is a computer-switched bank of cables, must be continually adjusted to maintain the equality of the signal paths to within about 1 cm as the Earth’s rotation changes the direction to the star, and hence the geometric delay (Fig. 2.8).

2.2.2 Interference Fringes and Fringe Visibility

The basic principle of stellar interferometry is illustrated in Fig. 2.2. The stellar interferometer is represented as a two-slit experiment, with each slit corresponding to one of the telescopes. The distance between the telescopes, D , is referred to as the *baseline*. The sources pictured are pairs of points, each being smaller than the resolution of the interferometer. They could be thought of as closely spaced binary stars, for example. Although the spacing in the figure has been exaggerated for clarity, it should be understood that *the points comprising each source are separated by an angle θ too small to be resolved by the individual telescopes*. Some typical numbers for the ISI would be $D = 32$ m, $\lambda = 11.15 \mu\text{m}$, and $\theta = 0.036''$. Each ISI telescope has a diameter of 1.65 m, so one can compare θ to the resolution of each telescope, which is given by the Rayleigh criterion (§1.1) as $1.7''$. The distances to all stars other than the Sun are so



$$\text{Fringe Visibility: } V_M \equiv \frac{I_{\max} - I_{\min}}{I_{\max} + I_{\min}}$$

$$\text{Resolution: } \theta_{\min} = \lambda/2D$$

Figure 2.2: Interference fringe visibility. Each of the two point sources, which are separated by an angle θ , produces a fringe pattern when received by the two-slit interferometer. Since the sources are mutually incoherent, the intensities of the individual fringe patterns add to yield the final pattern. The angles and the light wavelength are greatly exaggerated for clarity. See the text for a description of the fringe visibility and resolution.

enormous that the light from any point on a star arrives as a plane wave (excepting for atmospheric distortion, which will be discussed in §2.2.5).

Considering the components of the sources separately for the moment, we can see that the plane wave due to each unresolved point will form an interference pattern in the two-slit experiment. The intensities of the individual patterns are shown directly below the slits in Fig. 2.2. Because these individual patterns are formed by mutually incoherent points, there will be no interference between the two patterns, but rather, *the intensities of the individual fringes will add incoherently to produce the observed pattern*. This is analogous to what happens when two flashlights illuminate the same area. The intensities add, but there is no interference. The observed pattern, which is what would actually be seen on the screen of such a two-slit experiment, is shown below the individual patterns.

Even though the two source components are mutually incoherent, a fringe pattern is still observed in the example on the left-hand side of Fig. 2.2. One can easily see that if the source points were spatially coincident, the individual patterns would have the same phase, and the resulting sum would have full swings between zero and maximum intensity. If we observe sources with components that are separated by an angle θ , the contrast of the observed fringe pattern will decrease until the point shown on the right-hand side of Fig. 2.2, where uniform illumination is observed.

In order to express the degree of fringe contrast, Michelson defined the *fringe visibility*

$$V_M \equiv \frac{I_{\max} - I_{\min}}{I_{\max} + I_{\min}}, \quad (2.6)$$

where I_{\max} and I_{\min} are the maximum and minimum intensities in the observed fringe pattern, respectively. When V_M drops to zero, the source is said to be resolved. As shown on the right-hand side of Fig. 2.2, $V_M = 0$ when $\sin \theta = \lambda/2D$. Using the small-angle approximation,

$$\theta_{\min} = \lambda/2D, \quad (2.7)$$

where θ_{\min} is the angle taken to be the resolution limit for the interferometer. Comparing θ_{\min} to the Rayleigh criterion, we can see that the formal resolution of an interferometer is roughly the same as that of a telescope with radius D . Since the largest presently operating infrared telescope has an effective radius of 5 m, an interferometer such as the

ISI has a significant resolution advantage at a given wavelength. With a 32 m baseline, the ISI has a resolution $\theta_{\min} = 0.036''$.

An important feature of the observed fringe shown on the left-hand side of Fig. 2.2 is the offset in phase from the center of symmetry of the two-slit experiment. If the source were centered about the axis of symmetry, the fringe would also be centered, with zero phase. In actual practice, the phase of the fringe constantly changes during an observation. The rotation of the Earth moves the source with respect to the interferometer, sweeping the fringe past the center of symmetry. If a photodetector were placed so that it measured the intensity in a small area (\ll one cycle) of the fringe pattern, its output would be an oscillation at the *natural fringe frequency*, which is determined by D , λ , the position of the star, and the rotation rate of the Earth. The natural fringe frequency for the ISI would be about 210 Hz for a 32 m east-west baseline with the star due south on the celestial equator. It turns out that atmospheric fluctuations (§2.2.5), which introduce a random phase difference between the telescopes, make it difficult to measure the absolute phase of the fringe, and with a two-element interferometer, this information is lost. As will be discussed in §2.2.3, lack of phase information requires that some assumptions be made about the symmetry of the source if its brightness distribution is to be reconstructed.

Naturally, it is desirable to measure a wide range of sources with an interferometer, not just those whose angular size happens to coincide with a single combination of wavelength and baseline, as in Fig. 2.2. Recalling that $\theta_{\min} = \lambda/2D$, we can see that a source with a given angular size will be resolved if the baseline is increased until this equation is satisfied. In fact, in Michelson's original experiment, this is exactly what was done. A series of measurements was made with the interferometer mirrors at various separations until the fringe visibility dropped to zero, indicating the size of the source (which was the star α Orionis). Measurements at a wide range of baselines are made possible with a fixed interferometer by the technique of *Earth rotation synthesis*. Although the main collecting mirrors of an interferometer are separated by a baseline D , if the direction to the source is not perpendicular to the baseline, the resolution for a given measurement is determined by the *effective baseline* D_e . This is the projected baseline as seen from the direction of the source (Fig. 2.8). By situating the telescopes on an east-west baseline, the observer can make measurements with baselines D_e ranging from D when the source is on the meridian, all the way down to some small fraction

of D as it approaches the horizon. In principle, as the Earth rotates during the course of the night, the interferometer will measure the source's *visibility curve*, which is its fringe visibility V_M as a function of effective baseline D_e .

2.2.3 Fringe Visibility in Two Dimensions

If all sources were simple pairs of unresolved points, and all that was desired was the separation of the two points, it would be sufficient to find where the visibility curve for a given source drops to zero. One could then use (2.7) to compute the separation angle. Ultimately, however, the goal of interferometry is to take advantage of high angular resolution to discern structure in source images which appear only as points to a conventional telescope.

In the description that follows, and in the visibility curves shown later, the interferometer baseline will be represented by the *spatial frequency* $u = D/\lambda$, which is the length of the baseline in units of the observation wavelength. As shown in the previous section, $\lambda/2D$ is an angle, which is convenient to express in arcseconds. The spatial frequency will be expressed in inverse arcseconds (arcsec^{-1}), so

$$u \text{ (radians}^{-1}\text{)} = \left(\frac{180}{\pi}\right) \cdot 3600 \cdot u \text{ (arcsec}^{-1}\text{)}.$$

Figure 2.3 illustrates the situation when a real source, with a two-dimensional brightness distribution $B(\xi, \eta)$,¹ is observed with a two-element interferometer. Light from a point p in the source will arrive at each telescope, producing an electric field \mathbf{E}_{1p} at T_1 and \mathbf{E}_{2p} at T_2 , where

$$\begin{aligned} \mathbf{E}_{1p} &= E_{1p} e^{i(\omega t + \phi_{1p})} \quad \text{and} \\ \mathbf{E}_{2p} &= E_{2p} e^{i(\omega t + \phi_{2p})}. \end{aligned} \tag{2.8}$$

The phases ϕ_{1p} and ϕ_{2p} depend on the coordinates (ξ, η) of p , as well as the positions of the telescopes, expressed as spatial frequencies u and v . E_{1p} and E_{2p} are the (real) amplitudes after reception by the telescopes. These two fields are combined by the interferometer to produce a fringe pattern with field $\mathbf{E}_p = \mathbf{E}_{1p} + \mathbf{E}_{2p}$. Apart from a

¹Over a given bandwidth, $B(\xi, \eta)$ measures the power per unit area received at the ground from an element of the source subtending a given solid angle. It could have units of $\frac{\text{W}}{\text{m}^2 \cdot \text{steradian}}$, for example.

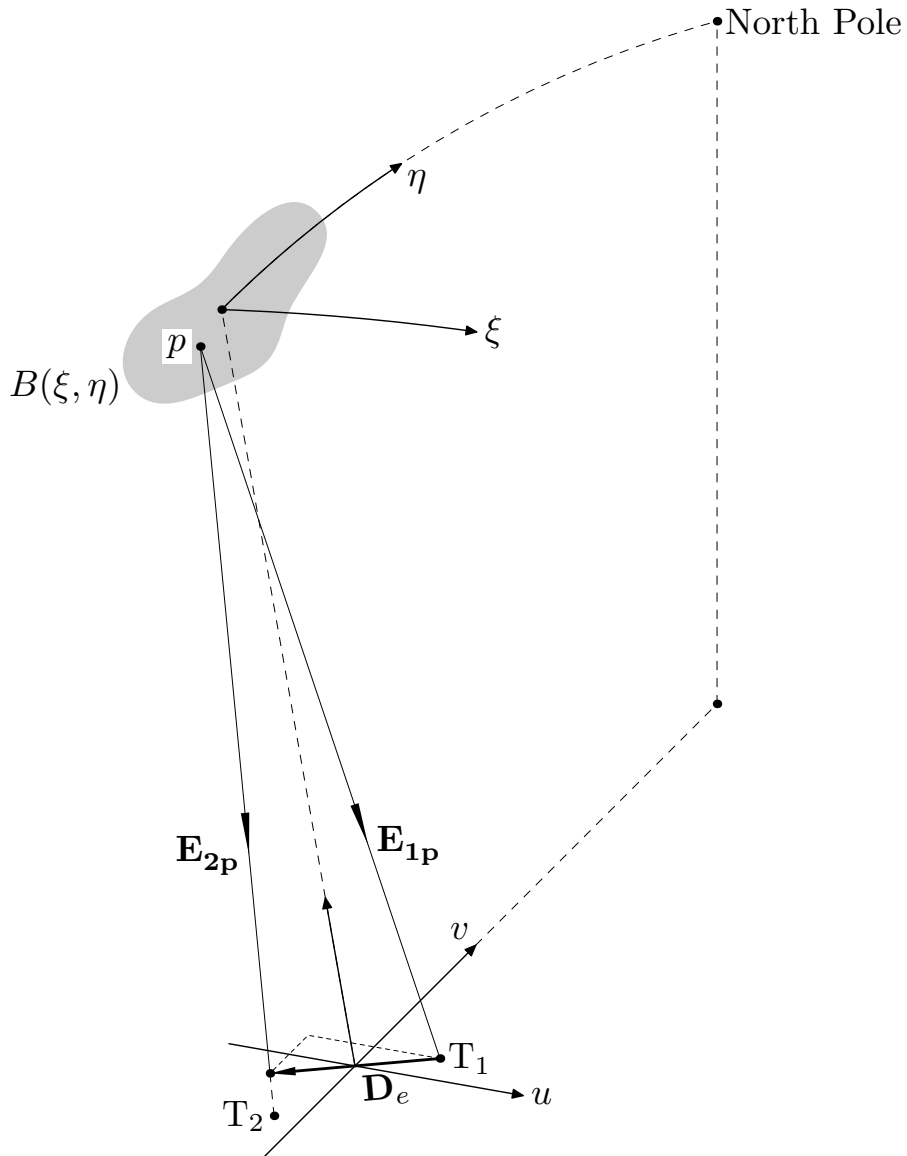


Figure 2.3: Brightness distribution $B(\xi, \eta)$ observed with a two-element interferometer. The source image is represented as a function of the two (small) angles, ξ and η . Effective baseline \mathbf{D}_e is the projection of the vector connecting telescopes T_1 and T_2 onto the (u, v) plane. This plane is perpendicular to a vector pointing at the center of the field of view. Radiation from a point p is collected by the telescopes and combined to produce a component fringe pattern. The complete fringe pattern is the sum of the components contributed by all points in $B(\xi, \eta)$.

constant factor ($\epsilon_0 c$), the irradiance of the fringe due to light from point p is

$$\begin{aligned}
I_p &= \langle \mathbf{E}_p \mathbf{E}_p^* \rangle \\
&= \langle (\mathbf{E}_{1p} + \mathbf{E}_{2p})(\mathbf{E}_{1p}^* + \mathbf{E}_{2p}^*) \rangle \\
&= \langle \mathbf{E}_{1p} \mathbf{E}_{1p}^* + \mathbf{E}_{2p} \mathbf{E}_{2p}^* + (\mathbf{E}_{1p} \mathbf{E}_{2p}^* + \mathbf{E}_{2p} \mathbf{E}_{1p}^*) \rangle \\
&= \langle \mathbf{E}_{1p} \mathbf{E}_{1p}^* \rangle + \langle \mathbf{E}_{2p} \mathbf{E}_{2p}^* \rangle + 2\Re\langle \mathbf{E}_{1p} \mathbf{E}_{2p}^* \rangle \\
&= I_{1p} + I_{2p} + 2\Re\langle \mathbf{E}_{1p} \mathbf{E}_{2p}^* \rangle, \tag{2.9}
\end{aligned}$$

where $\Re\langle \mathbf{E}_{1p} \mathbf{E}_{2p}^* \rangle$ is the real part of $\langle \mathbf{E}_{1p} \mathbf{E}_{2p}^* \rangle$. The angle brackets denote a time average over a period longer than one optical cycle, but shorter than the response time of the photodetector used to detect the fringe pattern. Substituting from (2.8) into the last term of (2.9), we have

$$\begin{aligned}
2\Re\langle \mathbf{E}_{1p} \mathbf{E}_{2p}^* \rangle &= 2\Re\langle E_{1p} E_{2p} e^{i(\omega t + \phi_{1p})} e^{-i(\omega t + \phi_{2p})} \rangle \\
&= 2E_{1p} E_{2p} \cdot \Re\langle e^{i(\phi_{1p} - \phi_{2p})} \rangle \\
&= 2E_{1p} E_{2p} \cdot \cos(\phi_{1p} - \phi_{2p}) \\
&= 2\sqrt{I_{1p} I_{2p}} \cdot \cos(\phi_{1p} - \phi_{2p}). \tag{2.10}
\end{aligned}$$

Finally,

$$I_p = I_{1p} + I_{2p} + 2\sqrt{I_{1p} I_{2p}} \cdot \cos(\phi_{1p} - \phi_{2p}). \tag{2.11}$$

Each point p will contribute a component fringe of the form (2.11), with irradiances determined by the value of $B(\xi, \eta)$ at p and the telescope responses, and phase $\phi_{1p} - \phi_{2p}$ determined by ξ , η , and \mathbf{D}_e .

The intensity I of the complete fringe pattern will be

$$I = I_1 + I_2 + 2\Re\langle \mathbf{E}_1 \mathbf{E}_2 \rangle, \tag{2.12}$$

where the quantities shown here are sums over all p in $B(\xi, \eta)$ of the corresponding subscripted variables in (2.9). If we define the complex *normalized correlation function*

$$\mu_{12}(\mathbf{D}_e) \equiv \frac{\langle \mathbf{E}_1 \mathbf{E}_2 \rangle}{\sqrt{I_1 I_2}}, \tag{2.13}$$

we can rewrite (2.12) as follows:

$$I = I_1 + I_2 + 2\sqrt{I_1 I_2} \cdot \Re\{\mu_{12}\}. \tag{2.14}$$

The maximum possible value of $\Re\{\mu_{12}\}$ is the modulus $|\mu_{12}|$. Likewise, the minimum value is $-|\mu_{12}|$. Thus,

$$\begin{aligned} I_{\max} &= I_1 + I_2 + 2\sqrt{I_1 I_2} \cdot |\mu_{12}| \quad \text{and} \\ I_{\min} &= I_1 + I_2 - 2\sqrt{I_1 I_2} \cdot |\mu_{12}|. \end{aligned} \quad (2.15)$$

Substituting into (2.6), we have

$$\begin{aligned} V_{\text{M}} &= \frac{2\sqrt{I_1 I_2}}{I_1 + I_2} \cdot |\mu_{12}| \\ &= |\mu_{12}| \quad \text{for } I_1 = I_2. \end{aligned} \quad (2.16)$$

Michelson's fringe visibility is therefore equal to the modulus of the complex normalized correlation function $\mu_{12}(\mathbf{D}_e)$. Using the small-angle approximation for ξ and η , as is done in the analysis of Fraunhofer diffraction, it can be shown (Thompson *et al.* [89]) that $\mu_{12}(\mathbf{D}_e)$ is the two-dimensional Fourier transform of $B(\xi, \eta)$:

$$\mu_{12}(\mathbf{D}_e) = \frac{1}{\sqrt{I_1 I_2}} \int_{-\infty}^{\infty} \int_{-\infty}^{\infty} B(\xi, \eta) e^{-2\pi i(D_u \xi + D_v \eta)} d\xi d\eta, \quad (2.17)$$

where D_u and D_v are the u and v components of the effective baseline vector \mathbf{D}_e . This result is known as the *Van Cittert-Zernike theorem*. It should be noted that only the component lengths of \mathbf{D}_e are important, not the position of the vector in the (u, v) plane.

Up until this point, we have been assuming that \mathbf{D}_e is well-defined by the positions of the two telescopes, so a given visibility measurement should yield the modulus of the two-dimensional function μ_{12} at a point (D_u, D_v) . In reality, however, the telescopes have sizes which can be an appreciable fraction of the baseline. Therefore, a visibility measurement actually samples a range of baselines between all of the pairs which can be made up of one point in \mathbf{T}_1 and one in \mathbf{T}_2 . This smearing of the effective baseline changes the visibility value obtained to that which would result from the convolution of $\mu_{12}(\mathbf{D}_e)$ with the telescope aperture. By the convolution theorem (Bracewell [17]), this operation is equivalent to multiplying $B(\xi, \eta)$ by $A(\xi, \eta)$, where $A(\xi, \eta)$ is the transform of the telescope aperture. We can define the *normalized complex visibility*

$$\mathbf{V}(\mathbf{D}_e) \equiv \frac{1}{\sqrt{I_1 I_2}} \int_{-\infty}^{\infty} \int_{-\infty}^{\infty} A(\xi, \eta) B(\xi, \eta) e^{-2\pi i(D_u \xi + D_v \eta)} d\xi d\eta, \quad (2.18)$$

the modulus of which is actually measured by the ISI. The visibility curves presented in the following sections are plots of $|\mathbf{V}(\mathbf{D}_e)|$ versus $|\mathbf{D}_e|$. For an ideal circular aperture,

the function $A(\xi, \eta)$ is just the familiar Airy pattern. In the modeling of ISI data, we use a Gaussian profile with a $2.5''$ full-width at half-maximum—based on measurements of the telescope beam—which takes into account atmospheric blurring.

By inverting (2.18), we should be able to reconstruct $B(\xi, \eta)$ if we can measure both the modulus *and the phase* of $\mathbf{V}(\mathbf{D}_e)$ for a large number of points in the (u, v) plane. Unfortunately, a two-element interferometer is limited to a small subset of the desired data. Because of atmospheric fluctuations (§2.2.5), measurement of the fringe phase is not practical. In addition, at best, two telescopes can have a range of baselines (using Earth-rotation synthesis) which forms a one-dimensional curve on the (u, v) plane.² These limitations force an assumption of axial symmetry about the center of the field of view in the reconstructed image.

The two-dimensional Fourier transform of an axially symmetric brightness distribution $B(\xi, \eta)$ will yield an axially symmetric $\mathbf{V}(\mathbf{D}_e)$. In this case, the function $\mathbf{V}(r')$ can be obtained by performing the one-dimensional Hankel transform (Bracewell [17]) of $B(r)$, where $r^2 = \xi^2 + \eta^2$, and $r'^2 = D_u^2 + D_v^2$. The Hankel transform is similar to the Fourier transform, except that Bessel functions are used in place of harmonic functions. This procedure (Hansen [36]), requires much less computation than a two-dimensional Fourier transform, and is therefore used when ISI data are modeled.

Despite the lack of (u, v) coverage and phase information, two-element interferometry provides scientifically useful high-resolution information which is not currently available by any other means.

2.2.4 Interpretation of Visibility Curves

Figure 2.4 shows three examples of intensity profiles for axially symmetric objects. The corresponding visibility curves, which would be measured by a two-element interferometer, are pictured next to the profiles.

The first example, at the top of the figure, is a Gaussian radial profile. The Hankel transform of a Gaussian is also Gaussian. The widths of the two curves are inversely related, such that the product of the full-width at half-maximum (FWHM) of the profile and the FWHM of the visibility curve is $-\frac{4}{\pi} \ln(\frac{1}{2})$. Because of the simplicity of this transform pair, Gaussian functions are useful as models when it is desirable to

²The telescopes can, of course, be moved to get more (u, v) coverage, but this is time-consuming, and baselines which are not oriented east-west make less effective use of Earth rotation synthesis.

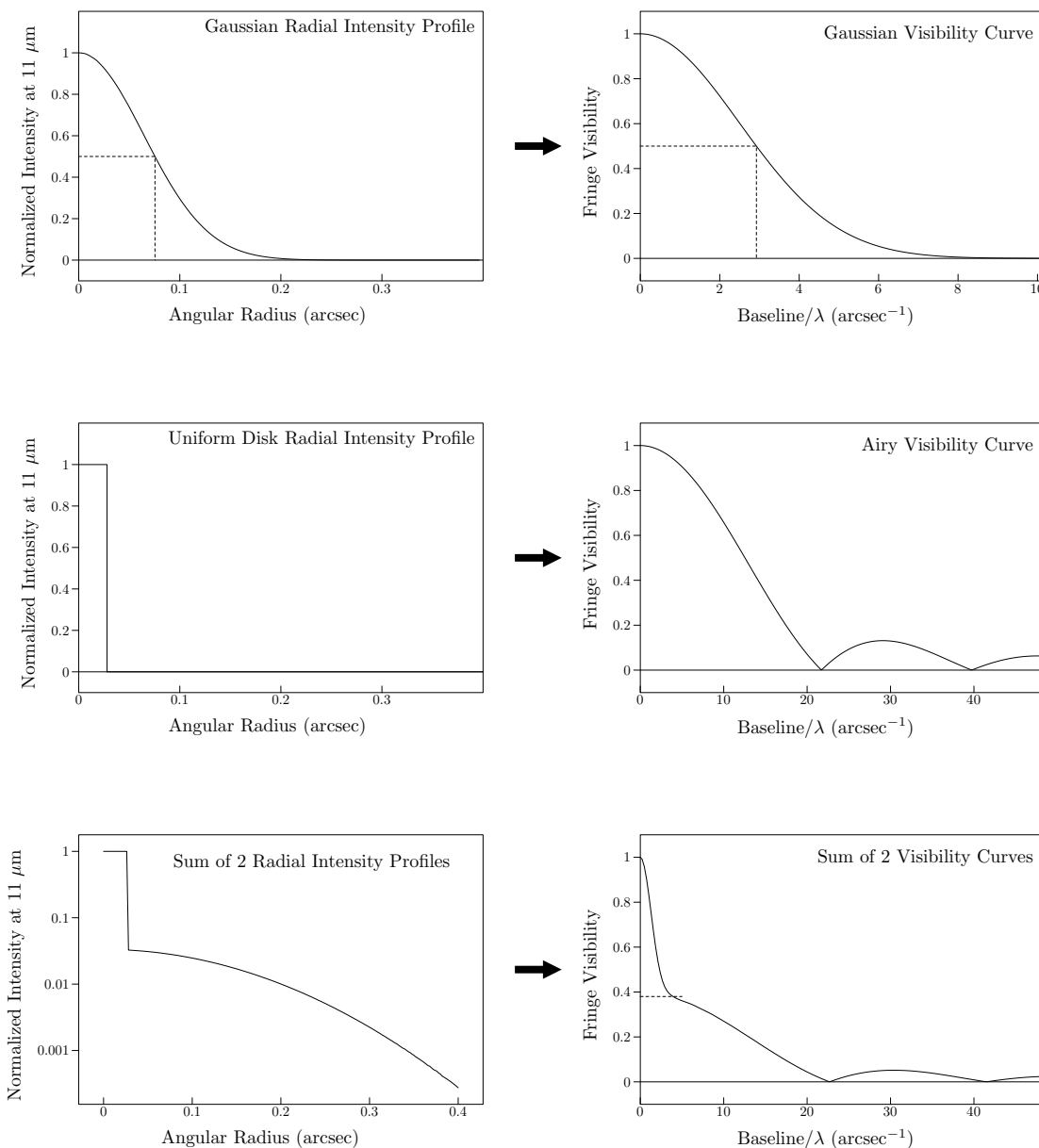


Figure 2.4: Examples of visibility curves. Shown above are radial intensity profiles and corresponding visibility curves for three simple objects with axial symmetry. The top example illustrates that a Gaussian profile results in a Gaussian visibility curve. The product of the full-widths at half-maximum of the profile and visibility curve is $-\frac{4}{\pi} \ln(\frac{1}{2})$. The middle example shows the visibility curve for a uniform disk. The final example illustrates the linearity of the Fourier transform. On the left is a radial profile made up of a uniform disk added to a broad, dim Gaussian (note the logarithmic scale). The visibility curve in this case is the sum of two curves, each corresponding to one of the components of the radial profile.

get a rough estimate of the size of an object from sparse visibility data. This technique is used in Appendix A.

The middle example in Fig. 2.4 shows a uniform disk and the corresponding visibility curve, which is an Airy function. A uniform disk is often used to model a star with no dust shell. The radius of the disk shown here was chosen to match the observed radius of α Orionis at $11\ \mu\text{m}$ ($0.0283''$, as given by Bester *et al.* [8]).

The final pair in the figure illustrates the linearity of the Fourier transform. If we have an object composed, for example, of a bright central star surrounded by dust, its intensity profile might look like a uniform disk added to a much dimmer extended Gaussian. The Fourier transform of the sum of these two functions is the sum of the individual transforms. Therefore, the resulting visibility curve consists of a narrow Gaussian, corresponding to the broad Gaussian in the profile, added to an Airy function, generated by the central disk. This visibility curve bears a qualitative resemblance to the curve for α Orionis (Fig. 3.30), though in that case, the dust is in a larger shell than in this example. The relative amounts of power contained in the disk and shell are the same in Fourier space as they are in real space. Even though the shell has a much lower brightness, it covers a much wider area³ than the disk, and thus contributes a substantial fraction of the visibility curve. Since the shell is much larger than the disk, it is resolved at shorter baselines (smaller spatial frequencies), and there is no contribution to the visibility curve from the shell past about $5\ \text{arcsec}^{-1}$. Although the power from the shell has been resolved, the power from the disk still contributes to the curve at the longer baselines.

Ideally, one might want to take a visibility curve from the ISI and directly transform it to obtain the brightness profile of the source. In practice, however, the data are usually too sparse for this to be effective. As will be discussed in Chapter 4, a better approach is to use a model of the star and its surroundings to generate a radial profile. This profile can then be transformed and compared with the data.

³Recall that the intensity profiles shown here are radial, so the amount of power received by the interferometer from the region of the source at angular radius r is proportional to $rB(r)$, where $B(r)$ is the intensity (brightness) profile.

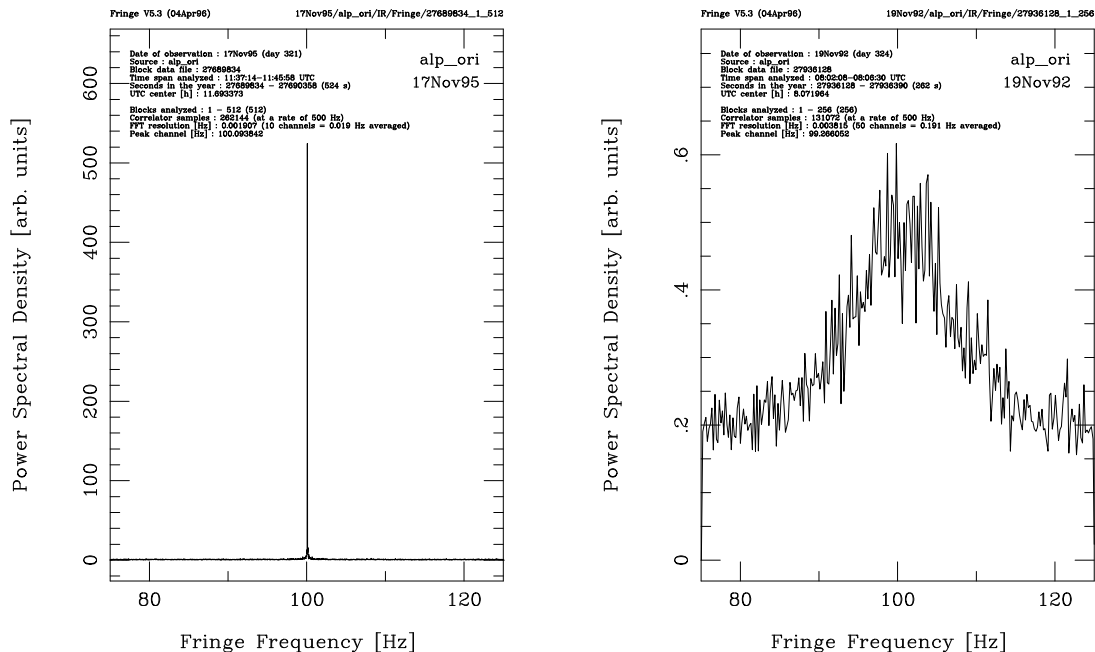


Figure 2.5: Fringe signal power spectrum under differing seeing conditions. The data shown here were taken on α Orionis in November 1995 and November 1992. The extremely narrow spectrum on the left is indicative of excellent atmospheric conditions. During the acquisition of the fringe signal whose spectrum is shown on the right, poor atmospheric conditions caused phase modulation of the signal components, broadening the spectrum.

2.2.5 Atmospheric Fluctuations

Fluctuations in the phase of starlight, due to variations in the atmospheric index of refraction, present a substantial obstacle to the gathering of accurate fringe visibility data. As can be seen in Fig. 2.2, any fluctuation in the phase of the incoming stellar wavefront which changes the relative phase at the two apertures of the interferometer will cause a shift in the phase of the fringe pattern due to that wavefront. Phase shifts in the plane wave components contributing to the fringe signal will blur the pattern, decreasing the precision of the visibility measurement. This situation is illustrated in Fig. 2.5. A formal treatment of the effects of the atmosphere (“seeing”) on interferometry can be found in a paper by Roddier [81].

Atmospheric fluctuations, being a manifestation of local weather and turbulent fluid flow, are inherently difficult to describe and predict. There are, however, some use-

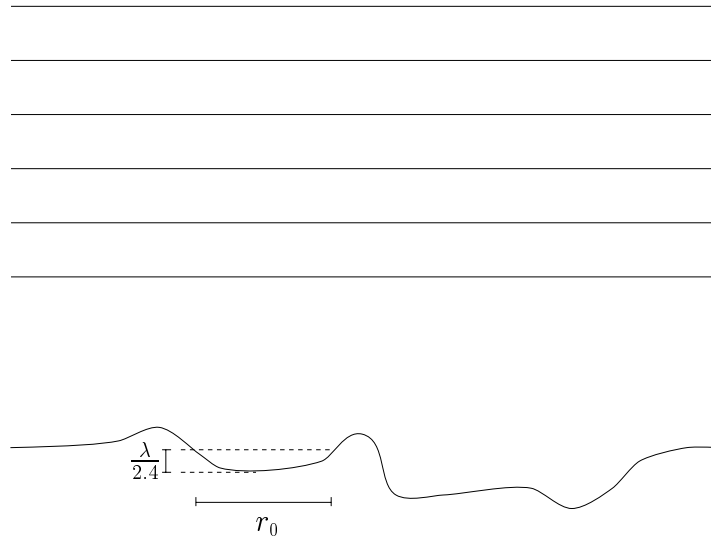


Figure 2.6: Illustration of the Fried coherence parameter. Initially parallel stellar wavefronts are distorted by fluctuations in the atmospheric index of refraction. r_0 is the distance over which the RMS wavefront distortion is $\lambda/2.4$. r_0 varies as $\lambda^{6/5}$ for an ideal atmosphere described by Kolmogorov turbulence theory, and is typically on the order of 10 cm at visible wavelengths.

ful scaling laws and order of magnitude estimations which allow us to characterize the problem. In his 1965 paper [30], Fried analyzed the distortion of an optical wavefront by atmospheric turbulence. His analysis derived statistical properties of the distortion of a wavefront passing through an atmosphere described by Kolmogorov turbulence theory. Fried defined a parameter, r_0 , the distance over which the root-mean-square (RMS) fluctuation of the phase of a wavefront with wavelength λ is $\lambda/2.4$, as is illustrated in Fig. 2.6. This definition of r_0 was chosen such that r_0 is “that diameter of a heterodyne collector for which distortion effects begin to seriously limit performance,” and is further explained in a subsequent paper [31]. In this latter paper, Fried also derived that, for propagation through Kolmogorov turbulence, $r_0 \propto \lambda^{6/5}$. It is also useful to know how fast the propagation conditions change in the atmosphere. If one uses the approximation that refractive index fluctuations occur in a fixed pattern which moves past the telescope at a typical atmospheric wind velocity ($v \approx 10$ m/s), the characteristic time corresponding to r_0 is r_0/v , which for visible wavelengths is on the order of 10 ms. This has proved to be a good approximation, as pictures of stars taken with exposure times

less than r_0/v tend to show significantly less blurring than do longer exposures.

Fried approximated the wavefront using a series of orthonormal polynomials, representing the phase distortion as an overall average phase change, two terms in the tilt of the wavefront (the “tip” and “tilt” in “tip-tilt correction”), spherical and hyperbolic deformations, and other higher-order terms. He was then able to derive RMS values of the coefficients representing the distortion in each of these components due to propagation through the turbulent atmosphere. All of the RMS coefficient values were found to vary as $(D/r_0)^{5/3}$, where D is the diameter of a circular region of interest (e.g. a telescope aperture) of the wavefront. Of significant interest is that the theoretical fraction of wavefront deformation in the tilt (first order) components was found to be 91% of the total, neglecting terms of third order and higher. Using Fried’s results, Tango and Twiss [86] predicted a fractional loss of visibility due to the tilt components of a bit less than 20% for an interferometer with $D/r_0 = 0.4$, which is the case for the ISI at $11\ \mu\text{m}$, assuming a typical r_0 at this wavelength of 4 m.

It should be emphasized that any numerical prediction using these results is imprecise at best. Even at Mt. Wilson observatory, renowned for its excellent seeing conditions, characteristics of the atmospheric turbulence can vary by up to an order of magnitude. An illustration of this variance is given in Fig. 2.7. In addition to the caprices of the atmosphere, there are weaknesses in other assumptions underlying Fried’s results. Turbulence theory obviously can not take into account such influences as local terrain variations, sources of heat, or trees. On a more subtle level, work done by our group has shown that in certain regimes, Kolmogorov turbulence is not sufficient to explain the behavior of the atmosphere. In particular, under favorable seeing conditions, phase fluctuations grow more slowly than expected with time (Bester *et al.* [7]), and conditions near the ground must often be modeled separately to adequately explain the observed fluctuations (Truehaft *et al.* [90]).

In order to compensate for the first order phase fluctuations caused by the atmosphere, a tip-tilt correction system has been constructed for the ISI. Although this system can not compensate for overall phase differences induced by the atmosphere along the line of sight to the star (the zero-order term in Fried’s approximation), the first order distortions of the wavefront can be largely removed. The resulting improvements to ISI data quality are discussed in §3.4.4.

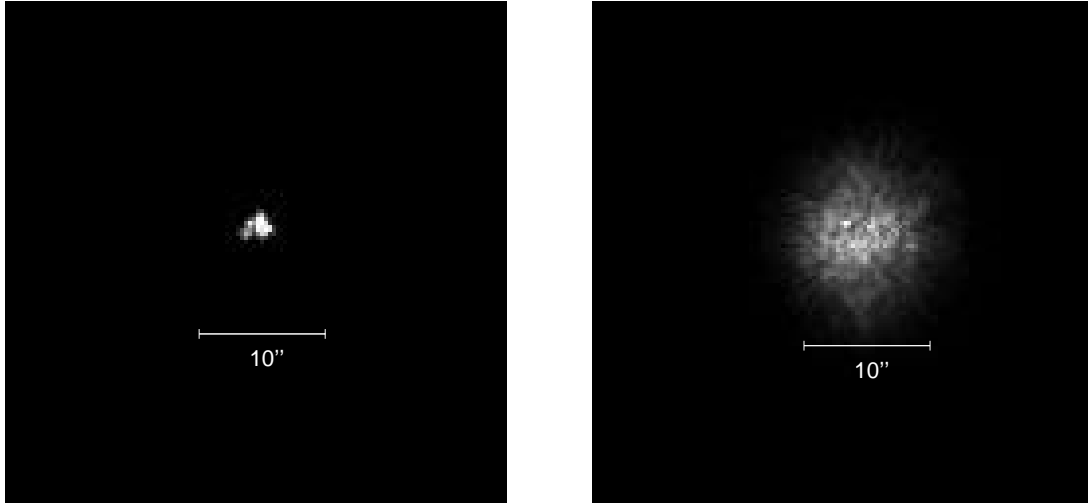


Figure 2.7: Star images under different seeing conditions. These star images were taken by the ISI guider cameras on nights which represent the extremes of the seeing conditions at Mt. Wilson. See also Fig. 2.5.

2.3 Radio Interferometry, Heterodyne Detection, and the ISI

A number of the technical difficulties associated with optical interferometry do not apply to interferometers operating at radio wavelengths. The lower frequencies and longer wavelengths allow the use of electronic circuitry for manipulation and combination of stellar signals, and greatly reduce the requirements of extreme rigidity and stability which make the construction of an optical interferometer so difficult. The field of radio interferometry has advanced significantly beyond the stage of two-element instruments. Arrays of radio antennas take fringe data simultaneously on a number of baselines, allowing the reconstruction of two dimensional images. Such techniques have only become possible at optical wavelengths within the last few years. The most accurate stellar positions available are measured using radio interferometers with intercontinental baselines. In these instruments, the individual signals are recorded on tape, and the actual combination to produce fringes takes place later. This is, of course, impossible at optical frequencies. A comprehensive treatment of radio interferometry, including a historical review, is given in Thompson, Moran, and Swenson's *Interferometry and Synthesis in*

Radio Astronomy [89].

The U.C. Berkeley Infrared Spatial Interferometer (ISI) is a two-element (though a third is under construction) interferometer which operates in the mid-infrared (9–12 μm). Despite the relative proximity of the mid-infrared to the visible region of the spectrum, the ISI uses heterodyne detection, a technique common to radio interferometers. Figure 2.8 shows a block diagram of a basic heterodyne stellar interferometer, and Fig. 2.9 illustrates the difference between heterodyne and “direct” detection. In heterodyne detection (§3.2.1), light from the source under observation is combined with radiation from a “local oscillator” (LO). This combination produces a signal at a frequency (the “intermediate frequency” or IF) which is the difference between that of the LO and that of the source. This difference signal is then at a much lower frequency (200 MHz–3 GHz for the ISI) than that of the infrared starlight (30 THz), which enables manipulation of the signal with electronic circuitry. The use of heterodyne detection in the ISI is made possible by stabilized CO₂ lasers which serve as local oscillators.

Heterodyne detection in the mid-infrared provides a number of advantages for interferometry, but also has its drawbacks. A major difference between heterodyne and direct detection is that with heterodyne, the detection bandwidth is relatively narrow, being limited by the detectors used to gather the difference frequency signal. In the case of the ISI, the detectors have a 3 GHz bandwidth, which provides us with a (dual sideband) detection bandwidth $\Delta\nu = 6 \text{ GHz}$, compared to a fractional bandwidth of 10% (a few terahertz) which would be reasonable for a corresponding direct detection instrument. While in the case of comparable bandwidths, heterodyne detection can have a larger signal-to-noise ratio (SNR), this factor of roughly 500 difference in bandwidths results in a much larger signal power, and corresponding gain in SNR, for direct detection.

In order to clarify this theoretical advantage, it is useful to examine the situation quantitatively, comparing the ISI with a hypothetical 10 μm direct-detection interferometer. In a typical application of heterodyne detection, the power of the local oscillator far exceeds that of the signal which is to be measured. For example, the signal power from the ISI LO exceeds that from the brightest 11 μm source in the northern sky by about a factor of about 10^9 at the detector. Since the detector output current is proportional to the product of the input signal amplitudes (§3.2.1), the large LO power results in a correspondingly large signal current. This current contains the phase

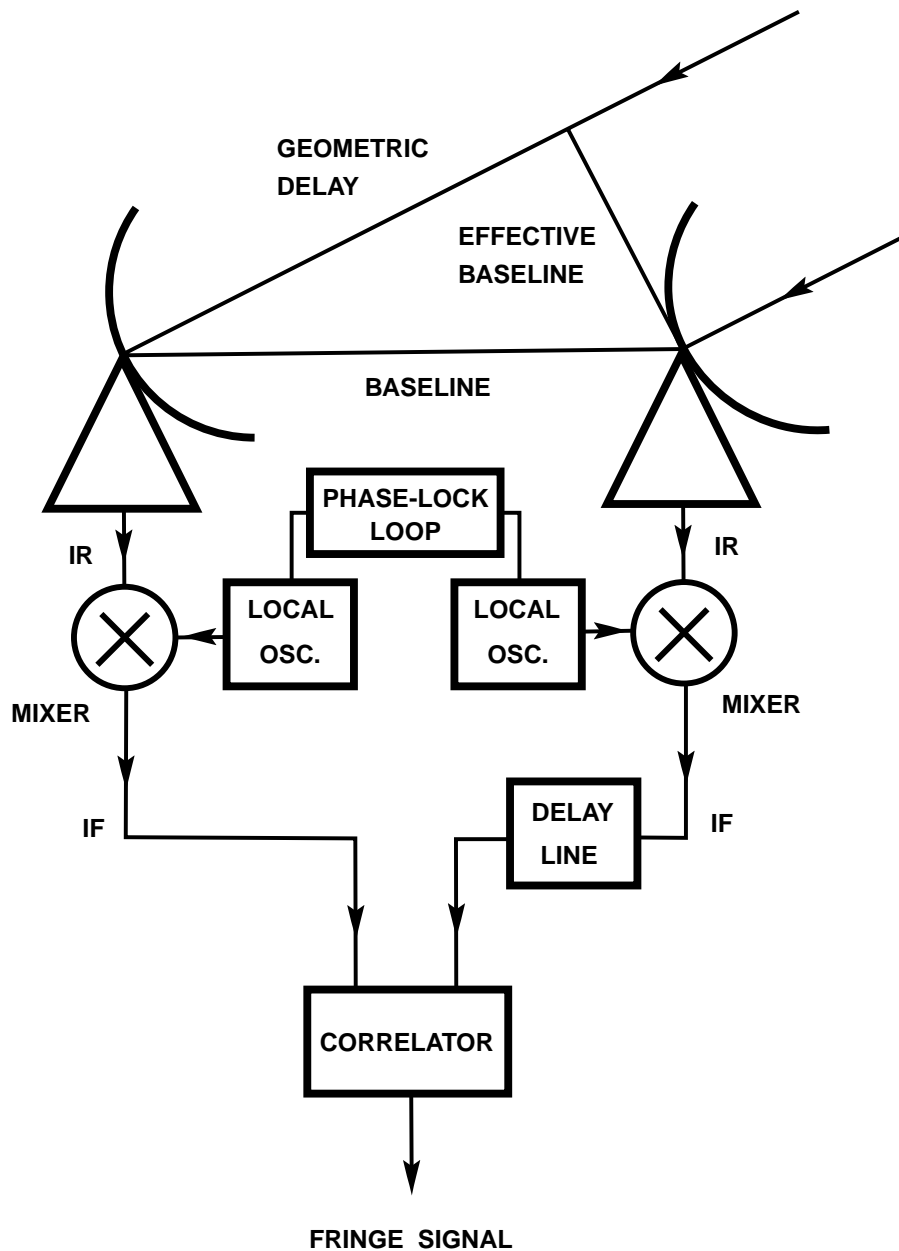


Figure 2.8: Heterodyne stellar interferometer. After reception by the telescopes, infrared starlight (IR) is combined with light from a local oscillator to produce an intermediate-frequency (IF) signal. The phase relationship between the two local oscillators is controlled by a phase-lock loop. The IF signal from one of the telescopes is sent through a delay line in order to compensate for the geometric delay shown in the path taken by the starlight. Finally, the signals are combined in a correlator to produce interference fringes.

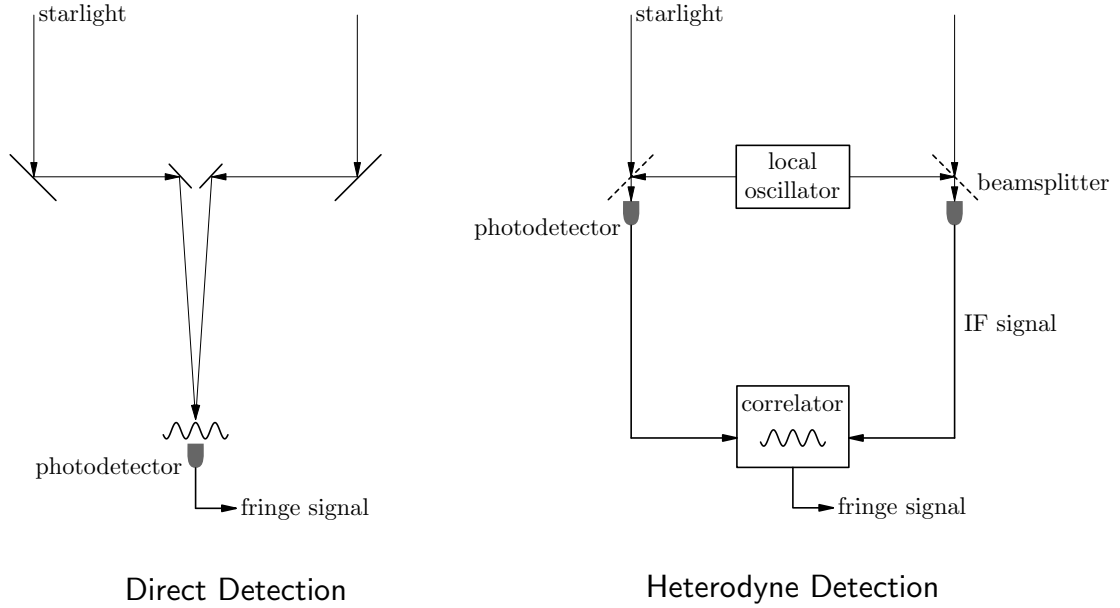


Figure 2.9: Schematic comparison between direct and heterodyne detection in stellar interferometers. In a direct detection interferometer, collimated starlight from both telescopes is combined to produce an interference pattern. A photodetector is used to measure the intensity in a small (\ll one cycle) area of the pattern. A heterodyne system combines the starlight in each telescope with the signal from a local oscillator. This produces an intermediate frequency (IF) signal which preserves the phase of the starlight. If the phase relationship between the two local oscillator signals is fixed, the IF signals from the two telescopes can be combined in an electronic correlator to produce a fringe signal.

information from the small signal of interest, and can be made large enough that noise from the detector, amplifiers, and thermal background is insignificant by comparison. This leaves fluctuations in the input signal (essentially all of which is the LO) photon count as the dominant source of noise. The SNR in this case, using a detector with quantum efficiency η , is given by Betz [11] as:

$$\text{SNR}_{\text{het}} = \frac{\eta P_s}{h\nu B} \sqrt{Bt}$$

where $h\nu$ is the photon energy, P_s is the signal power, B is the IF bandwidth, and t is the duration of the measurement. For the purposes of this comparison, ideal ($\eta = 1$) photodetectors will be assumed for both types of detection system. Setting $\text{SNR}_{\text{het}} = 1$,

we find that the noise-equivalent-power⁴ (NEP) is

$$\text{NEP}_{\text{het}} = \frac{h\nu B}{\sqrt{Bt}} = \frac{h\nu\sqrt{B}}{\sqrt{t}} = \frac{h\nu\sqrt{\Delta\nu}}{\sqrt{2t}}, \quad (2.19)$$

where we have used the dual-sideband detection bandwidth $\Delta\nu = 2B$. For the ISI, operating at $11\ \mu\text{m}$, with $\Delta\nu = 6\ \text{GHz}$, this is

$$\text{NEP}_{\text{ISI}} \approx 1 \times 10^{-15}\ \text{W} \quad (2.20)$$

for a 1 second measurement.

The noise in a mid-infrared direct detection interferometer would be dominated by fluctuations in the thermal background from the instrument and its surroundings. We can make an rough estimate of this noise as follows. The thermal radiation background power (Kingston [48]) received by the detector is

$$P_b = \epsilon A \Omega \frac{2h\nu^3 \Delta\nu}{c^2(e^{h\nu/kT} - 1)}, \quad (2.21)$$

where ϵ is the combined emissivity of the optical system and atmosphere, A is the detector area, Ω is the solid angle over which radiation is collected (the product $A\Omega$ remains constant throughout the optical system), and $\Delta\nu$ is the detection bandwidth. We will assume that the detector has a size and placement in the optical system such that it accepts radiation in only one spatial mode, corresponding to a plane wave perpendicular to the optical axis at the entrance pupil. This will be approximately true if the detector corresponds to the size of the Airy disk. Although some radiation from other modes may hit the detector, this approximation will give us a good lower limit. For this mode, the solid angle of collection at the primary mirror $\Omega \approx (\lambda/D)^2$, where D is the primary mirror diameter. We then have

$$A\Omega \approx D^2 \left(\frac{\lambda}{D}\right)^2 = \lambda^2 = c^2/\nu^2.$$

Substituting into (2.21), we have

$$P_b = \frac{2\epsilon h\nu \Delta\nu}{e^{h\nu/kT} - 1} = \bar{N} h\nu,$$

where $\bar{N} = \frac{2\epsilon \Delta\nu}{e^{h\nu/kT} - 1}$ is the average number of photons received per second. At $11\ \mu\text{m}$ with a 290 K background, the photon arrival fluctuations are described by Poisson statistics. The RMS noise in P_b will therefore be $\sqrt{\bar{N}t}$ photons per measurement time t .

⁴The NEP is the signal power required to produce an SNR of 1 in the specified measurement time.

Finally, we have

$$\text{NEP}_{\text{direct}} = h\nu \frac{\sqrt{Nt}}{t} = h\nu \sqrt{\frac{N}{t}} = \frac{h\nu\sqrt{\Delta\nu}}{\sqrt{t}} \sqrt{\frac{2\epsilon}{e^{h\nu/kT} - 1}}. \quad (2.22)$$

Comparing the the expressions for $\text{NEP}_{\text{direct}}$ and NEP_{het} from (2.19), we have

$$\text{NEP}_{\text{direct}} = 2\sqrt{\frac{\epsilon}{e^{h\nu/kT} - 1}} \text{NEP}_{\text{het}}$$

if $\Delta\nu$ is the same for both systems. Note, however, that this is not normally the case, so there will usually be an additional factor of the square root of the ratio of the bandwidths which must be used in a comparison. We will assume that the total emissivity at 11 μm of the atmosphere and the mirrors in the telescope is approximately 0.5, which is reasonable for a realistic optical system with on the order of 10 mirrors which are not perfectly clean. At a background temperature of 290 K we then have

$$2\sqrt{\frac{\epsilon}{e^{h\nu/kT} - 1}} = 0.15.$$

Using a bandwidth of 3 THz for our hypothetical 11 μm direct-detection interferometer, we get

$$\sqrt{\frac{\Delta\nu_{\text{direct}}}{\Delta\nu_{\text{het}}}} = \sqrt{500} = 22.4.$$

Comparing (2.22) with (2.19) and (2.20), we can estimate that for this instrument,

$$\text{NEP}_{\text{direct}} \approx 3 \times 10^{-15} \text{ W}$$

for a 1 second measurement. This is about 3 times NEP_{ISI} from (2.20).

Although the NEPs are comparable for the two different types of detection, the amount of signal power received by each system is proportional to $\Delta\nu$. With a $\Delta\nu$ 500 times that of the heterodyne system, a direct-detection interferometer would theoretically enjoy an SNR approximately $500/3 \approx 170$ times (5.6 stellar magnitudes) larger. This apparent relative advantage for direct detection is never realized in practice. The above analysis fails to take into account a significant advantage of small bandwidth. The ISI's bandwidth of 6 GHz yields a coherence length (§2.2.1) of 5 cm. In addition to greatly simplifying a number of aspects of instrument construction, this large coherence length allows the ISI delay line to operate in a “passive” mode, whereby the delay line is adjusted, based on the computed geometry of the star and telescopes, such that the

path length difference remains less than about 1 cm. The adjustment need only take place a few times per minute on average. As a result, the ISI can perform continuous averaging of the fringe visibility. Atmospheric fluctuations will cause the phase of the fringe to shift, but because of the large coherence length, the geometric delay will still be compensated, and the fringe amplitude (and hence visibility) will remain constant. A direct detection interferometer, however, typically has only a few wavelengths of coherence. This forces such an interferometer to use “active” delay tracking, in which the delay line is rapidly adjusted so that it can compensate for the atmosphere and keep the path lengths equal to within a few wavelengths. The time which an active delay-tracking system has to measure the fringe, compute a correction, and compensate for the state of the atmosphere is necessarily less than the atmospheric coherence time. Such a fast measurement can only be made on sufficiently bright sources, and in practice, this severely reduces the number of sources which can be measured with a direct-detection interferometer. While the ISI can observe a weak star continuously for a time on the order of an hour, a direct-detection mid-infrared interferometer would be limited to sources for which it could measure the fringe signal in less than about a third of a second.

The narrow bandwidth of a heterodyne system also affords the opportunity to make spectral measurements with high spatial resolution. Gathering this valuable information about the distribution of atoms and molecules in stellar atmospheres is not practical using direct detection systems. Typical mid-infrared Doppler-broadened linewidths seen in the material around stars are on the order of a few hundred megahertz. A heterodyne system can collect such a narrow-band signal using filters and enjoy relatively good sensitivity, since heterodyne noise is proportional to the square root of the bandwidth. Such work with a direct-detection system would require a relatively high resolving power (roughly 10^5), and the low photon count would cause the signal to be dominated by detector and amplifier noise. A heterodyne system with sufficiently high local oscillator power would avoid this noise problem. The ISI is presently being used to make spectral measurements with a resolution of 60 MHz. This resolution corresponds to the Doppler shift due to motion at about 0.7 km/s, and is thus sufficient to make useful measurements of outflow velocities in stellar dust shells. Such velocities are usually on the order of 20 km/s.

An effect, not related to bandwidth, which confers a relative advantage on

heterodyne detection is that of wavefront matching. The ISI will only detect incoming radiation which matches the shape of the local oscillator wavefront. This radiation contains the desired information about the source. In contrast, a direct detection interferometer will detect radiation which has been distorted by the atmosphere, and thus cannot combine to produce fringes. This will add to the background level of the fringe pattern, corrupting the visibility measurement.

Finally, the use of heterodyne detection allows amplification and splitting of the down-converted stellar signal. These manipulations can be accomplished with standard microwave electronics, and result in no significant loss in signal-to-noise ratio. For interferometric arrays with n elements, the signal from each telescope must be shared among $n(n-1)/2$ baselines. In a direct-detection array with more than a few elements, the requisite splitting of the optical signal from each telescope would cause a substantial signal-to-noise reduction. This advantage of heterodyne detection will take on increasing importance as the field of optical and infrared interferometry matures.

Chapter 3

The U.C. Berkeley Infrared Spatial Interferometer

The U.C. Berkeley Infrared Spatial Interferometer (ISI) is a two-element interferometer which makes use of heterodyne detection in order to measure stellar fringe visibilities in the 9–12 μm wavelength range. The ISI is located at Mt. Wilson Observatory in the San Gabriel mountain range north of Los Angeles, California. As shown in Figs. 3.1 and 3.2, each of the ISI telescopes is mounted in a standard semitrailer, and uses two large mirrors in a configuration known as a “Pfund” design, named after the spectroscopist who first used an instrument [78] of this type. When the interferometer is in use, the mirror mounts are each supported by large steel pedestals. These pedestals rest on concrete pads which have been laid out on the site in a pattern that allows baselines of different lengths and orientations to be realized. The optics table in each trailer, on which the detection system and its associated optics are mounted, is supported by the flat mirror mount, and is thus somewhat isolated from vibrations of the trailer. When the trailers are to be moved, as when a baseline change occurs, the trailer frames are raised so that they pick up the mirror mounts. The trailers can then be towed to new positions. A general description of the ISI, along with some early results, can be found in a paper by Bester, et. al. [9]. Since the ISI began taking fringes in June 1988, many upgrades [6] have been performed, including the construction of the guiding and tip-tilt correction system to be described in this chapter.

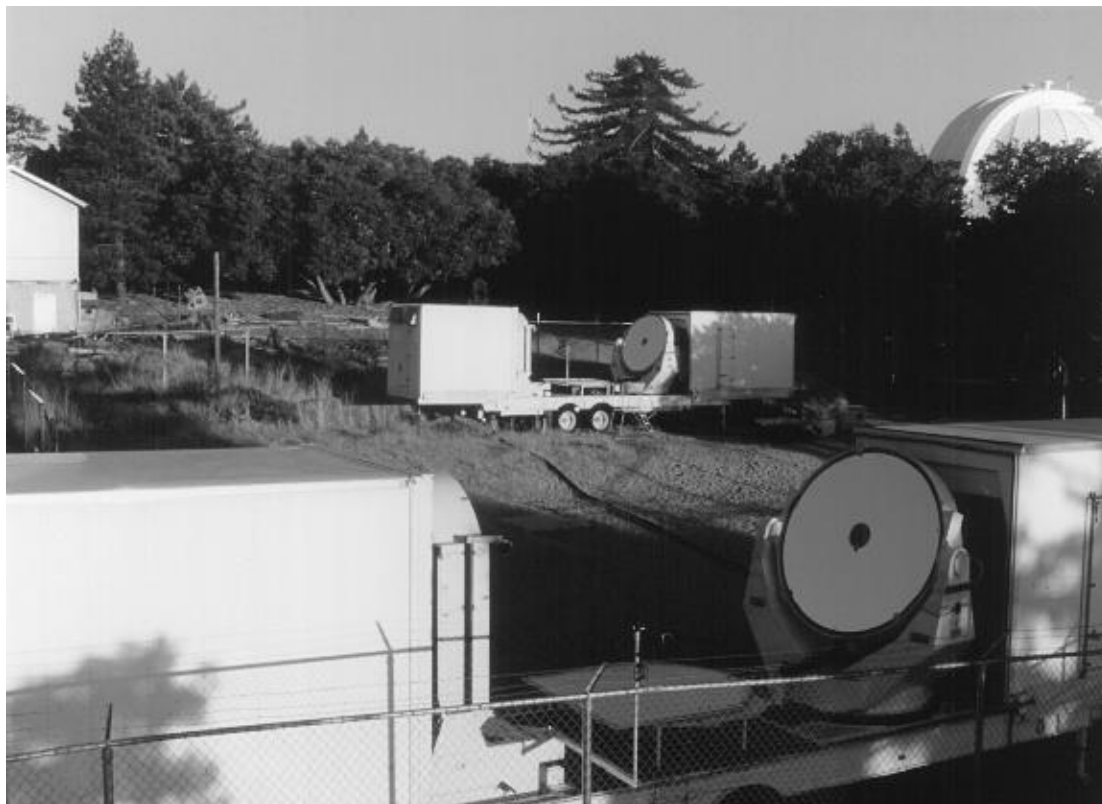


Figure 3.1: The U.C. Berkeley Infrared Spatial Interferometer. The interferometer is comprised of two Pfund telescopes, each mounted in a standard semitrailer. Here the interferometer is shown on a 32 m baseline. The 2 m steerable flat mirrors can be seen in this view. In the upper right of the photograph is the 100 inch telescope dome, where Michelson and Pease carried out the first successful measurement of the angular diameter of a star, and in the upper left is the building where a subsequent attempt at interferometry with longer baselines was made (§2.1).

3.1 Optical System

Each telescope has two large mirrors, a flat mirror, 2 m in diameter, on a steerable mount, and a paraboloid, 1.65 m in diameter, mounted vertically (Fig. 3.2). During operation of the telescope, the flat mirror tracks a star, redirecting the starlight to the paraboloid. The paraboloid brings the light to a focus through a hole in the flat mirror. The beam then continues on into a Schwarzschild optical system, as shown in Fig. 3.3. This combination of two front-surface spherical mirrors collimates the beam with minimal aberration and without the use of transmissive optics. Once past

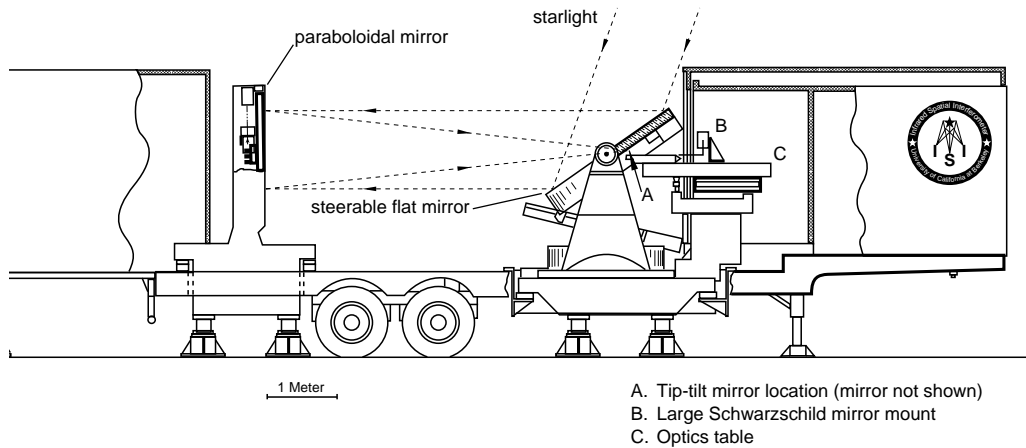


Figure 3.2: ISI telescope trailer. Starlight incident on the steerable flat mirror (right) is focused by the paraboloid (mounted vertically at left) through a hole in the flat. Behind the flat mirror (to the right) is the optics room, which contains the guider camera, beam combining optics, and heterodyne detection system.

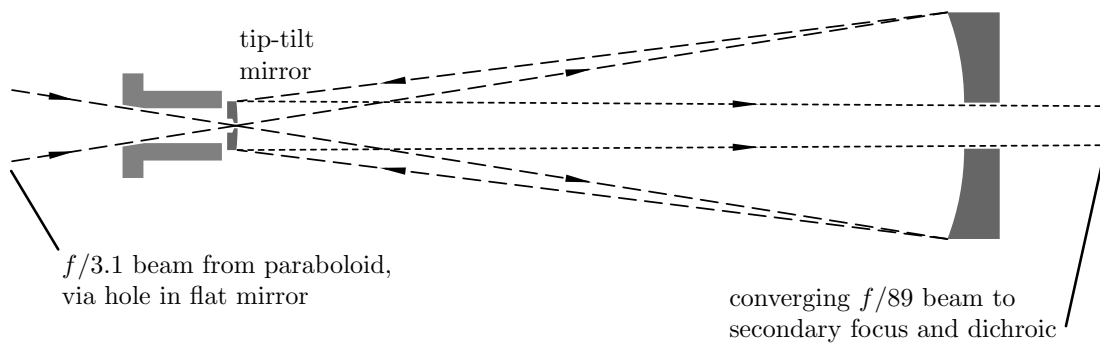


Figure 3.3: Schwarzschild optical system and telescope beam. The focus of the ISI telescope primary mirror lies at the center of the tip-tilt mirror.

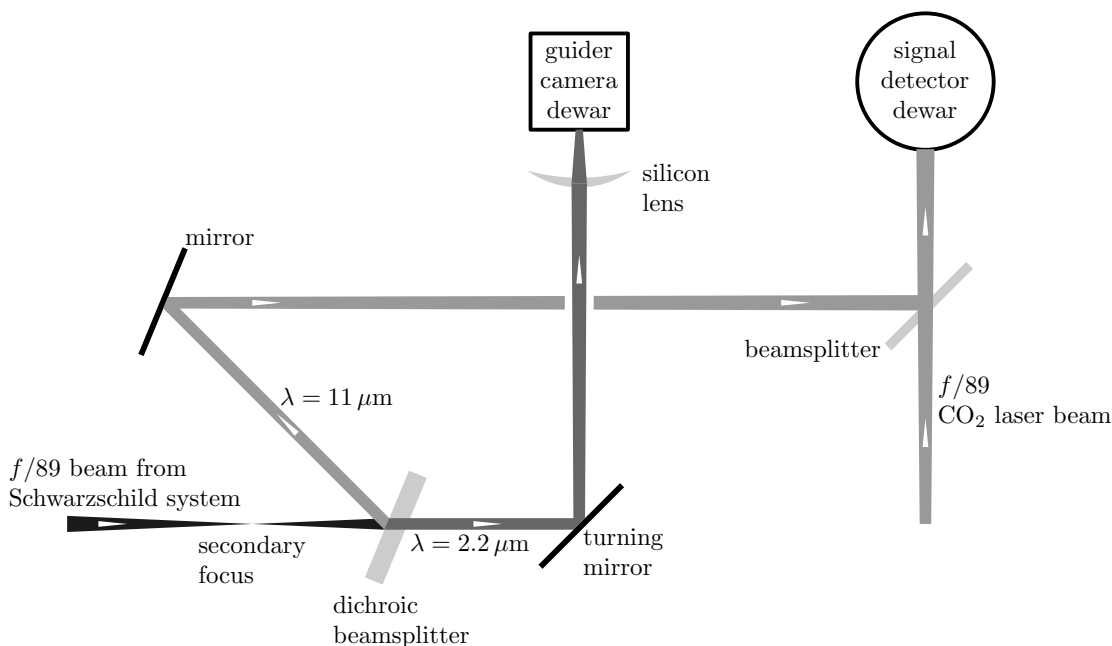


Figure 3.4: Dichroic beamsplitter, camera, and signal detector. The $f/89$ starlight beam from the Schwarzschild optical system (Fig. 3.3) converges to a focus just before the dichroic beamsplitter. The near-infrared light is sent to the guider camera, and the mid-infrared light is combined with the light from the local oscillator on the way to the signal detector dewar. The beam convergence at the secondary focus is exaggerated for clarity. Positions and sizes of the various components shown in this schematic illustration can be seen, drawn to scale, in Figs. 3.5 and 3.6.

the Schwarzschild optical system, the $f/89$ beam is brought to a secondary focus. A few centimeters beyond the focal point, the beam is split into two parts by a dichroic beamsplitter (Fig. 3.4). The mid-infrared radiation is sent to the fringe detection system, while the near-infrared light is sent into the guider camera. Figures 3.5 and 3.6 are detailed drawings of the optics tables which hold the guider cameras and detection systems. The tip-tilt mirrors are mounted on extensions attached to the tapered ends of the tables.

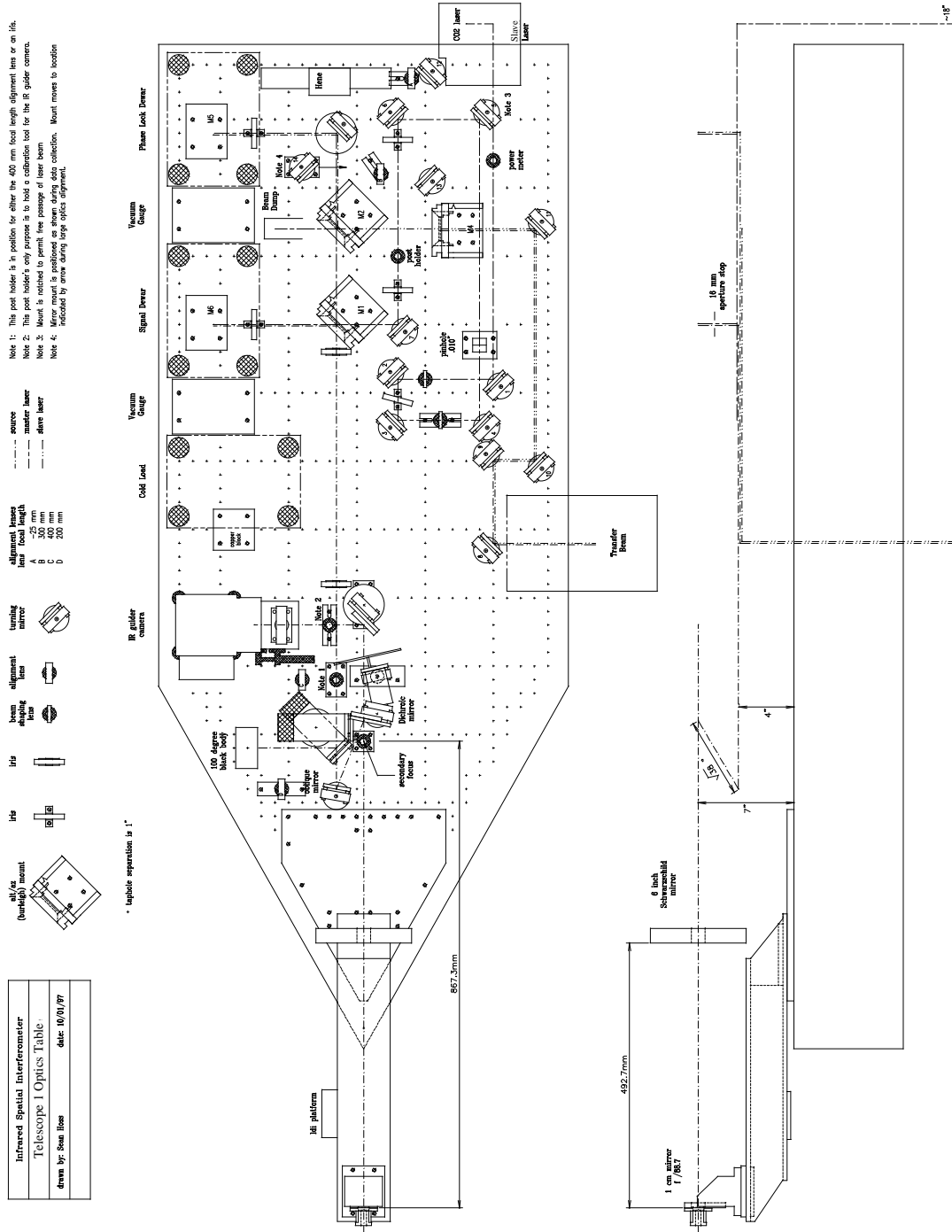


Figure 3.5: Telescope 1 optics table. If the diagram is viewed with the tapered section of the table at the left, the cold load, signal detection, and phase lock dewars can be seen on the upper edge of the table. The guider camera is next to the cold load dewar. Light enters through the Schwarzschild optics at the tapered end of the table.

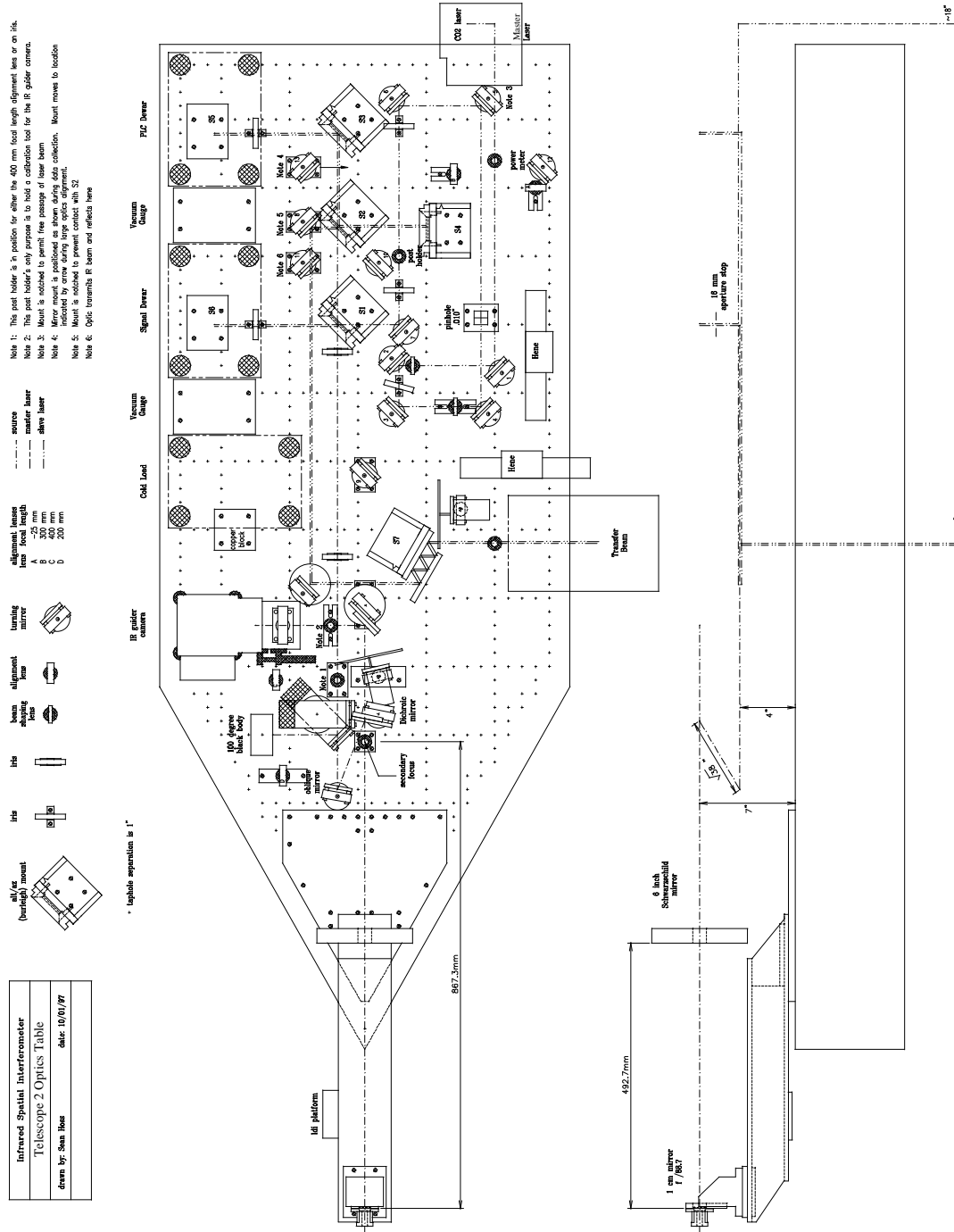


Figure 3.6: Telescope 2 optics table. The path length stretcher is labeled S7 and has a zigzag light path passing through its two parallel flat mirrors. The CO₂ laser local oscillator (not shown) is affixed to the bottom of the table, and the beam is brought up through a box on the upper right of the table as shown here.

3.2 Fringe Detection

3.2.1 Heterodyne Signal Detection

The ISI uses a heterodyne (frequency conversion) fringe detection system, as is common in radio interferometry. The idea of such a system is that the stellar signal at each telescope is combined with that from a “local oscillator” (LO) whose frequency (about 30 THz) lies at the center of the region of interest in the star’s spectrum. This combination produces a signal which is at much lower frequency (200 MHz-3 GHz), but preserves the phase relationship between the starlight and the LO. The resulting intermediate frequency (IF) signal can be detected and amplified, with very little loss in signal-to-noise ratio, using standard microwave electronics. A very extensive discussion of heterodyne detection as it pertains to stellar interferometry can be found in *Interferometry and Synthesis in Radio Astronomy* [89].

In the case of the ISI, the LO is a CO₂ laser. This laser can be run on a variety of spectral lines in the 9–12 μm range, and can use different isotopes of C and O. During the course of the research described in this dissertation, the laser was run on the P(20) line of ¹³C¹⁶O₂ at 11.15 μm. The laser beam is focused through a pinhole which is placed the same optical path distance from the detector as the secondary focus of the starlight (the secondary focus occurs after the Schwarzschild optical system at the point (Fig. 3.4) where the $f/89$ beam shown in Fig. 3.3 converges). This placement provides an LO wavefront which matches that of the stellar signal.

The combined signal has two components, one whose irradiance varies at the sum frequency (stellar signal frequency plus laser frequency), and another whose irradiance varies at the difference frequency. Specifically, if we express the electric fields of the LO and a component of the starlight as follows,

$$\begin{aligned}\mathbf{E}_{\text{LO}} &= E_{\text{LO}} \cos(\omega_{\text{LO}}t + \phi_{\text{LO}}) \\ \mathbf{E}_{\text{s}} &= E_{\text{s}} \cos(\omega_{\text{s}}t + \phi_{\text{s}})\end{aligned}$$

then the heterodyne signal

$$\begin{aligned}\mathbf{E}_{\text{het}} &= \mathbf{E}_{\text{s}} + \mathbf{E}_{\text{LO}} \\ &= E_{\text{s}} \cos(\omega_{\text{s}}t + \phi_{\text{s}}) + E_{\text{LO}} \cos(\omega_{\text{LO}}t + \phi_{\text{LO}}).\end{aligned}\tag{3.1}$$

In this representation, \mathbf{E}_s is the starlight of a single frequency ω_s *originating from one unresolved point in the source*.¹ It will be shown later in this chapter that an electrical fringe signal, analogous to the individual point fringe patterns in Fig. 2.2, will be produced in a heterodyne interferometer by each point in the source. It will also be shown that all frequency components originating from one point on the star will produce a fringe signal with the same phase.² The irradiance resulting from \mathbf{E}_{het} in (3.1) is proportional to the time average of the square of the combined electric fields:

$$\begin{aligned}
\mathbf{I}_{\text{het}} &\propto \langle \mathbf{E}_{\text{het}}^2 \rangle \\
&= \langle [E_s \cos(\omega_s t + \phi_s) + E_{\text{LO}} \cos(\omega_{\text{LO}} t + \phi_{\text{LO}})]^2 \rangle \\
&= \langle E_s^2 \cos^2(\omega_s t + \phi_s) + E_{\text{LO}}^2 \cos^2(\omega_{\text{LO}} t + \phi_{\text{LO}}) + \\
&\quad 2E_s E_{\text{LO}} \cos(\omega_s t + \phi_s) \cos(\omega_{\text{LO}} t + \phi_{\text{LO}}) \rangle \\
&= \frac{E_s^2}{2} + \frac{E_{\text{LO}}^2}{2} + 2E_s E_{\text{LO}} \langle \cos(\omega_s t + \phi_s) \cos(\omega_{\text{LO}} t + \phi_{\text{LO}}) \rangle \tag{3.2}
\end{aligned}$$

where we have used the fact that

$$\langle \cos^2(\omega t + \phi) \rangle = \frac{1}{2}$$

The first two terms on the right hand side of the final form of (3.2) are constant, while the third term contains the phase and frequency information. This third term can be further simplified. Adding the following identities:

$$\begin{aligned}
\cos(a) \cos(b) - \sin(a) \sin(b) &= \cos(a + b) \\
\cos(a) \cos(b) + \sin(a) \sin(b) &= \cos(a - b)
\end{aligned}$$

we get

$$2 \cos(a) \cos(b) = \cos(a + b) + \cos(a - b). \tag{3.3}$$

¹In order to keep the notation reasonably simple in this section, “*p*” subscripts have been omitted from quantities such as E_s and ϕ_s . The reader who wishes to compare the following analysis of ISI signals with the discussion in §2.2.3 should remember that all source signals used here are components from a single point in the brightness distribution $B(\xi, \eta)$.

²This is strictly true only to the extent that the fractional bandwidth $\Delta\lambda/\lambda$ is small enough that the change in fringe phase produced by $\Delta\lambda$ is equal to that which would be produced by a negligible change in the position of the source point. For the ISI, $\Delta\lambda/\lambda \approx 2 \times 10^4$. Since for small angles, the sky position angle $\theta \propto \lambda$ for a given fringe phase change (see Fig. 2.2 and accompanying discussion), the fractional change in θ is the same as the fractional change in λ . This change in θ is negligible compared with the interferometer resolution, even for the largest possible θ , which is the edge of the telescope beam at about $2.5''$. A much larger effect is due to the finite size of the telescopes (§2.2.3).

If we equate

$$\begin{aligned} a &\equiv \omega_s t + \phi_s \\ b &\equiv \omega_{LO} t + \phi_{LO} \end{aligned}$$

and use (3.3), we find that the oscillatory term from (3.2),

$$2E_s E_{LO} \left\langle \cos(\omega_s t + \phi_s) \cos(\omega_{LO} t + \phi_{LO}) \right\rangle$$

becomes

$$E_s E_{LO} \left\langle \cos[(\omega_s - \omega_{LO})t + \phi_s - \phi_{LO}] \right\rangle + E_s E_{LO} \left\langle \cos[(\omega_s + \omega_{LO})t + \phi_s + \phi_{LO}] \right\rangle$$

and finally, the irradiance can be expressed as follows:

$$\begin{aligned} \mathbf{I}_{\text{het}} &\propto \frac{E_s^2}{2} + \frac{E_{LO}^2}{2} \\ &\quad + E_s E_{LO} \left\langle \cos[(\omega_s - \omega_{LO})t + \phi_s - \phi_{LO}] \right\rangle \\ &\quad + E_s E_{LO} \left\langle \cos[(\omega_s + \omega_{LO})t + \phi_s + \phi_{LO}] \right\rangle \end{aligned} \quad (3.4)$$

The time average used in this classical description of the irradiance is taken over a period which is long compared with one optical cycle (Born & Wolf [14]), but short compared with the response time of the detector. The response time of the detector is half the inverse of its bandwidth (Kingston [48]).

The combined signal is directed onto a HgCdTe detector (Bester *et al.* [6]), which has a bandwidth of about 3 GHz and produces a signal current I_{sig} proportional to the irradiance \mathbf{I}_{het} . During operation, all infrared detectors in the ISI system are cooled to 77 K using liquid nitrogen. Since the last term in (3.4) oscillates at an angular frequency $\omega_s + \omega_{LO}$, which well exceeds the detector bandwidth for any detectable frequency component of the stellar radiation, this term does not contribute to the signal current. In a field-theoretical treatment of photomixing (Teich [88]), the sum frequency term does not appear. The third term in (3.4), however, will result in an oscillating component to I_{sig} , so long as $|\omega_s - \omega_{LO}|/2\pi$ is less than the 3 GHz bandwidth of the detector. This term in the signal current contains the phase information from the starlight. The amplifier chain following the signal detector in an ISI telescope rejects the DC components of I_{sig} , so in the end, the signal current

$$I_{sig} \propto E_s E_{LO} \cos[(\omega_s - \omega_{LO})t + \phi_s - \phi_{LO}] \quad (3.5)$$

The ISI uses dual-sideband detection, by which it is meant that radiation within 3 GHz above and below ω_{LO} will contribute to I_{sig} .³ These sidebands should not be confused with the sum and difference frequencies resulting from the photomixing.

3.2.2 Phase Locking

Each telescope produces a signal of the form shown in (3.5). Since we are ultimately interested in the relative phase of the starlight received at the two telescopes, we need to arrange a fixed phase relationship between the two local oscillators. We can then combine the signal currents to produce interference fringes and measure the fringe visibility.

Phase locking of the LOs is accomplished with an elaborate feedback system which monitors the relative phase of the LOs and adjusts the frequency of one of the lasers using a piezoelectric actuator which can change the length of the laser cavity. A block diagram of the detection system is shown in Fig. 3.7. The laser in one of the telescopes (pictured on the right in Fig. 3.7) is free-running, except for a feedback loop which adjusts the cavity length to produce the maximum possible power. A part of the beam from this laser (the “master laser”) is sent over to the other telescope, where it is combined with part of the beam from the other laser (the “slave”). The combined signal is detected in a fashion similar to the detection of the starlight described in §3.2.1. The detection of this beating produces a signal (the phase-lock signal) which contains the relative phase information.

Since the objective is to maintain a fixed phase relationship between the LOs at their respective detectors, we must also correct for the phase shift of the master laser beam as it travels over to the other telescope. This is accomplished by sending part of the transfer beam back to the telescope which houses the master laser. The returned beam is then mixed with the master beam to produce a signal which indicates the phase shift experienced by the transfer beam during its round trip between the telescopes. Using this signal, a second feedback system (the path length compensator) adjusts the path length stretcher, a pair of parallel mirrors through which the transfer beam travels. The stretcher can be seen in the upper right of Fig. 3.7 and in Fig. 3.6. The stretcher adjustment is carried out continually in order to maintain a fixed optical

³The sign of $\omega_s - \omega_{LO}$ is not important in (3.5), since this will merely affect the phase of the resulting I_{sig} . In the case where $\phi_s = \phi_{LO}$, there would be no difference, since cosine is an even function.

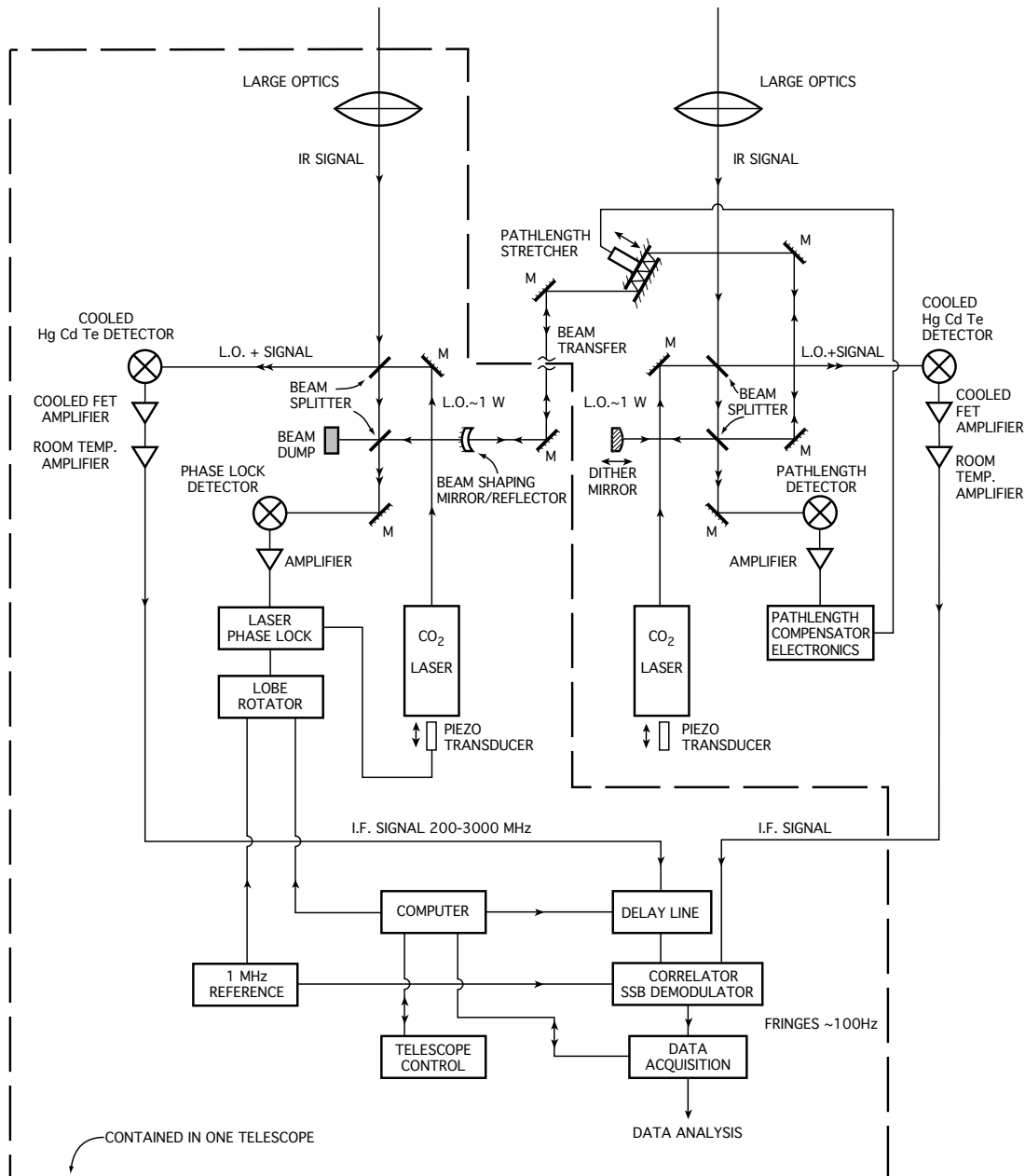


Figure 3.7: ISI detection system block diagram. The IR signal shown entering the system following the large optics is the $11\ \mu\text{m}$ portion of the beam separated by the dichroic in Fig. 3.4.

path length, and hence a fixed phase shift, for the transfer beam as it travels between the telescopes. Once the transfer beam phase shift is fixed, the phase-lock system is able to maintain a constant relationship between the LO phases at the heterodyne signal detectors.

The piezoelectric actuator in the slave laser is adjusted by the phase-lock system so that a known frequency separation and fixed phase shift is maintained between the two LOs. The frequency separation is 1 MHz, plus a small correction to be discussed in §3.2.3. The 1 MHz offset, which allows for simpler and more accurate detection of the phase difference between the LOs, is later removed from the fringe signal by a single-sideband demodulator. We can thus treat ω_{LO} as being the same in both telescopes.

3.2.3 Signal Combination

During observations, each telescope provides an electric signal of the form given in (3.5):

$$\begin{aligned}\mathbf{I}_1 &= A_1 \cos[(\omega_s - \omega_{\text{LO}})t + \phi_1 - \phi_{\text{LO}}] \\ \mathbf{I}_2 &= A_2 \cos[(\omega_s - \omega_{\text{LO}})t + \phi_2 - \phi_{\text{LO}}]\end{aligned}\tag{3.6}$$

where A_1 and A_2 incorporate the (different) star and LO signal amplitudes ($E_s E_{\text{LO}}$) from each telescope, as well as a proportionality constant to account for the detector and amplifier responses in that telescope. Before these two signals are combined in the correlator to produce the interference fringes, the signal from the telescope which houses the correlator is passed through a delay line, as discussed in §2.2. The ISI delay line consists of a bank of cable segments of differing lengths. The real-time computer system calculates the geometric delay based on the position of the star, and switches in the appropriate length of cable to equalize the path lengths for the two signals.

At this stage, each signal is split into two parts, as shown in Fig. 3.8. One part is sent through a non-linear circuit element, which produces an output proportional to A_1^2 or A_2^2 . The other part is sent to the correlator, which produces an output proportional to $\mathbf{I}_1 \mathbf{I}_2$.

Infrared Power Detection

The first part of each signal is used as the input to a lock-in amplifier, which is referenced to the signal from a chopper positioned in the telescope beam. The output of the lock-in

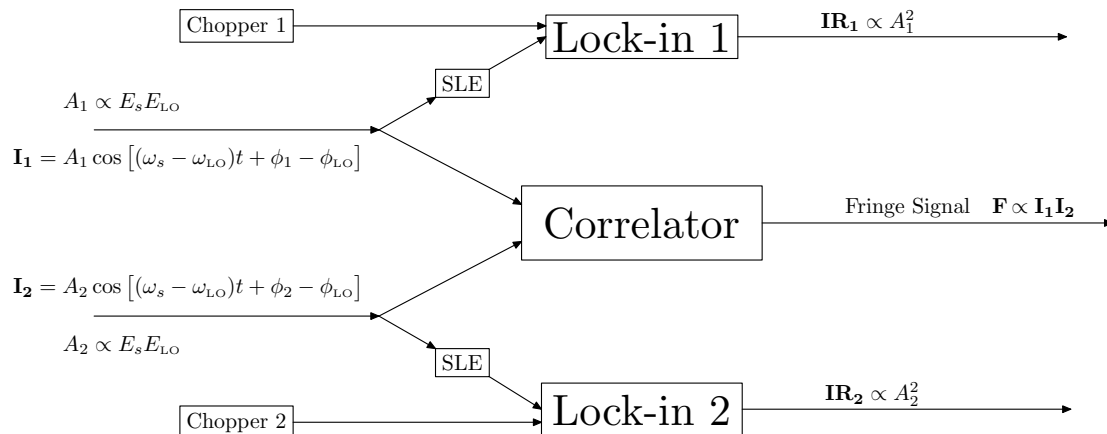


Figure 3.8: Correlator signal path. The boxes labeled “SLE” represent square-law elements, which produce an output voltage proportional to the square of the input voltage.

amplifier is proportional to the infrared power (the time-averaged square of the electric field amplitude) seen by the detector. During observations, the interferometer switches between two modes. In chopping mode, the choppers run, and every 15 seconds, the telescope alternates between the star and two off-source positions $5''$ away from the star. When the choppers, which are highly reflective, are in the beam, the signal detectors see a cold load, which is a combination of 77 K and room temperature black plates (the view is combined with a partially reflecting window on the cold load dewar) designed to approximate the radiation profile of a cold sky. Using the lock-in amplifier outputs (IR_1 and IR_2) from the on-source and off-source positions, we can calculate the infrared power received from the star by the detector.

Fringe Signal Detection

When the telescope is in non-chopping mode, the choppers are turned off, and the position switching is halted. This allows the telescopes to stare at the source and collect fringe data. For the brightest sources, fringe data collected in chopping mode can be used, but for most sources, the chopped fringe signal is too noisy to provide accurate visibility measurements.

The second part of each split signal is sent into the correlator (Fig. 3.8). The correlator contains circuitry which produces a signal proportional to the product of

the signals from the individual telescopes. From the input signals given in (3.6), the correlator will produce a fringe signal of the following form:

$$\begin{aligned} \mathbf{F} &\propto \mathbf{I}_1 \mathbf{I}_2 \\ &= A_1 A_2 \cos[(\omega_s - \omega_{\text{LO}})t + \phi_1 - \phi_{\text{LO}}] \cos[(\omega_s - \omega_{\text{LO}})t + \phi_2 - \phi_{\text{LO}}]. \end{aligned} \quad (3.7)$$

Using the identity given in (3.3), we have

$$\begin{aligned} &\cos[(\omega_s - \omega_{\text{LO}})t + \phi_1 - \phi_{\text{LO}}] \cos[(\omega_s - \omega_{\text{LO}})t + \phi_2 - \phi_{\text{LO}}] \\ &= \frac{1}{2} \cos[2(\omega_s - \omega_{\text{LO}})t + \phi_1 + \phi_2 - 2\phi_{\text{LO}}] + \frac{1}{2} \cos(\phi_1 - \phi_2). \end{aligned} \quad (3.8)$$

If we recall that ω_s is a representative frequency component from the starlight, we can see that the first term on the right hand side of (3.8) will contain frequencies throughout the bandwidth of the detection and amplification system when the fringe signal is summed over all values of ω_s . This broad-band component of the signal is rejected by filters in the correlator electronics at the stage when the fringe signal is demodulated from the 1 MHz phase-lock offset (§3.2.2). At the output of the correlator, we are left with the following fringe signal:

$$\mathbf{F} \propto A_1 A_2 \cos(\phi_1 - \phi_2) \quad (3.9)$$

The fringe signal contains the desired information about the phase relationship between the starlight at telescope 1 and that at telescope 2, *and is independent of ω_s* .

If the star were stationary with respect to the two telescopes, the fringe signal would be a DC level determined by the phase difference $\phi_1 - \phi_2$. This DC level would be directly analogous to the fringe intensity level produced by one of the component point sources at the center of symmetry of the two-slit experiment shown in Fig. 2.2. Since the Earth is rotating, however, an interferometer will see a constant shifting of the fringe phase. This is known as the natural fringe frequency (§2.2.2). It is very desirable from an instrumentation point of view to have the fringe signal emerge from the correlator at a constant frequency, instead of whatever the natural fringe frequency happens to be for the source position of the moment. This is arranged in the ISI by a device known as the “lobe rotator,” which produces a small frequency offset, in addition to the 1 MHz phase-lock offset, on the slave laser (discussed in §3.2.2). The lobe rotator is controlled by the real-time computer system, which determines the proper frequency

offset for the current source position and delay line setting. The ISI fringe signal is held at 100 Hz. Each point component of the source therefore contributes a fringe signal at 100 Hz, the phase of which is determined by the value of $\cos(\phi_1 - \phi_2)$ corresponding to the location of the point in the source (see Fig. 2.2). The output signal, which is the sum of all the components, will have an amplitude (from which the visibility is derived) determined by the brightness distribution and shape of the source.

3.2.4 Data Acquisition and Storage

The ISI, alternating between chopping and non-chopping modes, provides three signals from which the fringe visibility measurements are eventually obtained: \mathbf{IR}_1 , \mathbf{IR}_2 , and \mathbf{F} . These signals are digitized and stored by one of the real-time computers (`vme0`) for analysis, which typically takes place at a later date. The signals are recorded and passed on to `vme0` by an analog-to-digital converter, which samples the \mathbf{F} signal at 500 Hz, and the \mathbf{IR}_1 and \mathbf{IR}_2 signals at 100 Hz. `vme0` adds an offset to the \mathbf{IR}_1 and \mathbf{IR}_2 signals in order to indicate which mode the ISI was in (chopping or non-chopping, and if chopping, on-source or off-source) when the data were taken. The three signals are then stored on a hard disk which is attached to the system control workstation (`isi10`). Computation of the fringe visibility values will be discussed in chapter 4.

3.3 Telescope Control

The various functions of the ISI are coordinated by a set of interconnected computers, as shown in Fig. 3.9. During observations, the operator controls the interferometer using a set of programs which run on a UNIX workstation. Typically, this is `isi10`, but any one of the workstations (all with names beginning in “`isi`”—see Fig. 3.9) can be used. The workstation communicates over the local-area network (Ethernet) with the real-time computers (names beginning with “`vme`”) and the guider PCs (`isicam1` and `isicam2`).

The real time system consists of three single-board (Motorola MVME-147) computers which run the VxWorks operating system. This operating system is designed to have very low dispatch latency, but is still able to run a number of tasks concurrently. These computers are responsible for tasks which require synchronization with external events, such as star tracking, data collection, and control of the delay line. `vme0` is

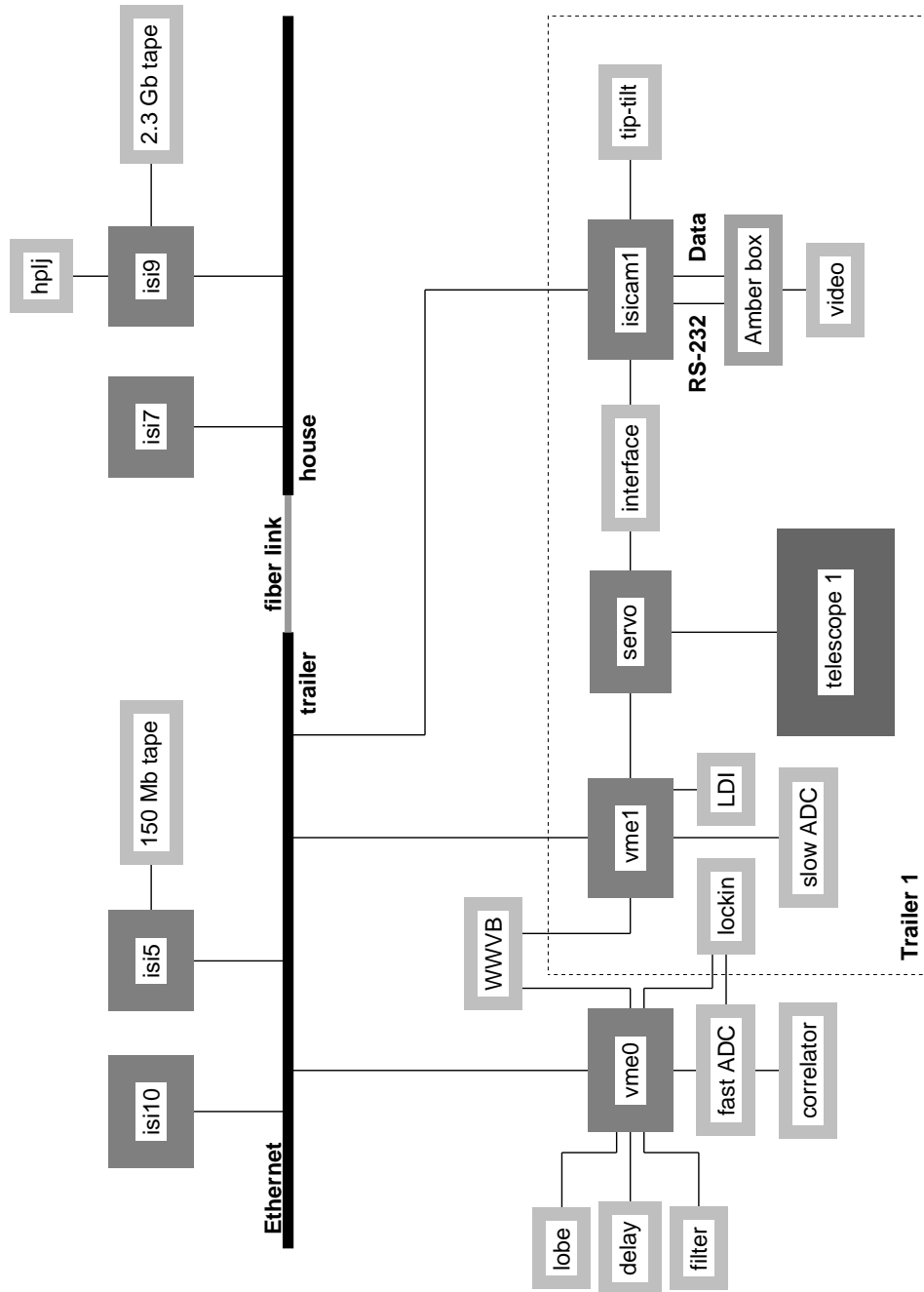


Figure 3.9: ISI computer configuration. All machines shown within the dotted outline have identical counterparts in trailer 2. See the text for a description of the various computers and their functions.

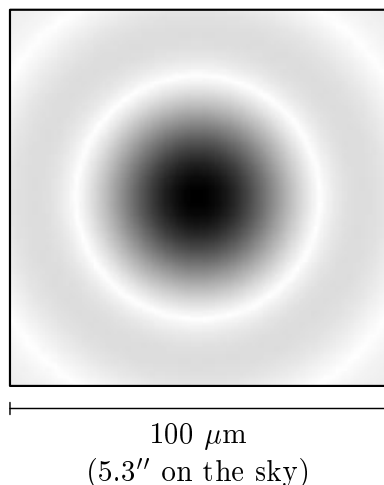


Figure 3.10: ISI signal detector with $\lambda = 11.15 \mu\text{m}$ beam. The detector is a square, approximately $100 \mu\text{m}$ on a side, corresponding to $5.3''$ in the telescope field of view. The beam shown here, with the Airy disc and most of the first diffraction ring on the detector, would result from a point source at the center of the field.

responsible for central functions, such as delay line control and data acquisition, while `vme1` and `vme2` each control telescope-specific functions. All three real-time computers run a customized star-tracking software system (Bester [10]). This system, which had to be written specifically for the ISI Pfund telescopes, is capable, when the telescope positions are properly calibrated, of pointing the telescopes to within about $15''$ of the desired position. Various routines within this software package compute quantities necessary for interferometry, such as the lobe rotation frequency, effective baseline, and other required parameters. `vme1` and `vme2` communicate over serial data lines with the servo microprocessors, which are specialized computers that drive the telescope motors and read the position encoders. The real time computers are synchronized to the time signal on radio station WWVB from the National Institute of Standards and Technology in Fort Collins, Colorado.

3.4 Telescope Guiding and Tip-Tilt Correction

In each ISI telescope, the heterodyne signal resulting from the combination of starlight with the CO_2 laser beam is focused onto a detector, as shown in Fig. 3.10. The beams in both telescopes must be on the signal detectors simultaneously in order for the interfer-

ometer to detect fringes. Deviations in the beam position corresponding to as little as $1''$ on the sky can result in a significant loss of fringe signal. In addition, some structure, such as that in the dust shells around evolved stars, is present more than $1''$ from the center of the field of view, and is therefore imaged onto the edge of the detector. Information about this structure will be lost if the beam does not remain centered. There are two major obstacles which must be overcome in order to keep the telescope beams centered. Small errors in the telescope star tracking occur over the course of a few seconds, while on a time scale ranging from tens to hundreds of milliseconds, atmospheric distortion of the wavefront from the source displaces the beam.

When the ISI was first built, guiding of the telescopes was carried out with a manual control, used by the operator to send corrections to the telescope servo system. The first autoguiding system used an inexpensive surveillance camera, which was later replaced with an astronomical grade silicon CCD-based camera. For sources with adequate visible flux, this system was able to correct errors in the telescope guiding, but the maximum frame rate of 10 Hz was not sufficient for fully correcting atmospheric fluctuations. In addition, the need for high flux in the visible presented a problem. The ISI is used to observe sources with substantial mid-infrared flux, and objects with high flux in this wavelength range tend to be surrounded by dust, which reduces the amount of visible radiation available to the guider camera. Table 3.1 gives photon fluxes from some typical ISI targets.

The CCD-based guiding system, in order to function effectively, had to acquire at least one frame per second with an adequate signal to noise ratio for the control computer to determine a star position. This condition resulted in a lower flux limit, after various losses in the optical system, sources of noise, and spreading of the star image on the CCD were taken into account, of about 5×10^7 photons per second incident on the primary mirror. This prevented the ISI from observing a number of interesting sources.

A significant gain in photon flux is available in the near-infrared, hence the new ISI guiding system is based on an InSb array detector which is sensitive to infrared light of between 1 and $5 \mu\text{m}$ wavelength. This camera allows the guiding system to follow the dim stars which were previously inaccessible, and for the brighter stars (in the $2.2 \mu\text{m}$ K band), it allows short enough exposures to do tip-tilt correction. As shown in Fig. 3.11, the atmospheric index of refraction [93] does not change significantly between

Table 3.1: Photon fluxes [32] from a sample of ISI observing targets. Values shown for variable stars are averages. V band is centered at $0.55 \mu\text{m}$, and K band is centered at $2.2 \mu\text{m}$.

Source	V band flux	K band flux
	Photons per second into ISI telescope $\div 10^6$	
α Boo	21,000	72,000
α Tau	9,600	60,000
α Sco	8,300	160,000
α Ori	8,300	150,000
α Her	1,100	110,000
\circ Cet	80	72,000
R Leo	13	50,000
IRC +10420	8	290
IRC +10011	5	720
IRC +10216	0.3	1,100
IK Tau	0.1	12,000

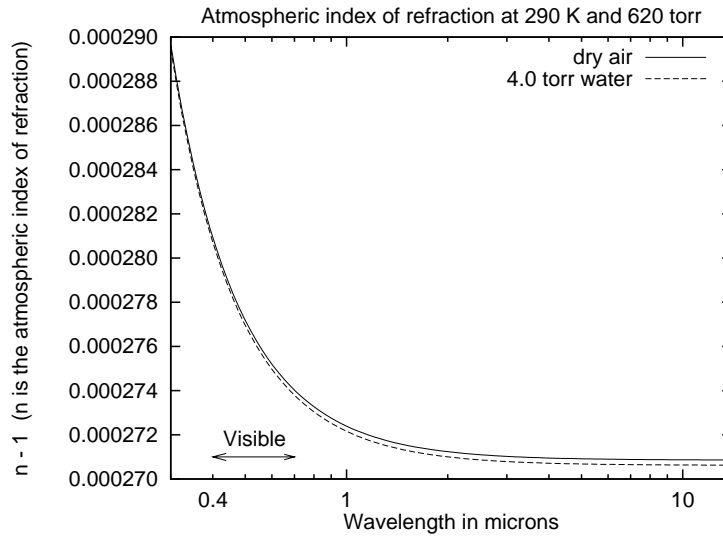


Figure 3.11: Atmospheric index of refraction in the visible and infrared.

Table 3.2: Amber AE4128 camera characteristics. Read noise and dark current values refer to individual pixels.

Array size:	128 × 128 pixels
Array area:	6.4 × 6.4 mm = 41.0 mm ²
Detector size:	43 × 43 μm
Detector pitch:	50 μm
Detector capacitance:	0.70 pF
Detector storage capacity:	3 × 10 ⁷ charges
Detector quantum efficiency:	≈ 75%
Read noise:	about 600 e ⁻ per pixel
Dark current:	4 × 10 ⁷ e ⁻ per second at 77 K 1 × 10 ⁵ e ⁻ per second at 55 K
Array power dissipation:	≈ 29 mW

2 and 11 μm, so correction of wavefront tilt in the near-infrared should also stabilize the mid-infrared signal.

3.4.1 Guiding System Hardware

Guider Cameras

The ISI uses two Amber Engineering (now Raytheon) AE4128 InSb cameras. Some characteristics of the cameras are shown in Table 3.2. These cameras represent a compromise between cost and convenience on one hand, and performance on the other. The AE4128 was designed for industrial inspection and military purposes. In these applications, background noise levels are not nearly as critical as they are for astronomical work, and hence the read noise and dark current exhibited by these cameras exceeds that which one finds in astronomical-grade cameras. A good InSb-based astronomical camera might have a read noise of a few tens of electrons, and a dark current which is negligible.

The Amber cameras, despite having some non-ideal characteristics, were the best selection for the ISI. The first consideration was cost. The AE4128 is an off-the-shelf product, and did not have to be custom manufactured. Secondly, the focal plane arrays in the cameras can run at rates up to 1000 frames per second, and the included electronics support rates up to 217 frames per second, which is more than adequate to compensate for atmospheric fluctuations in the near-infrared. Finally, the

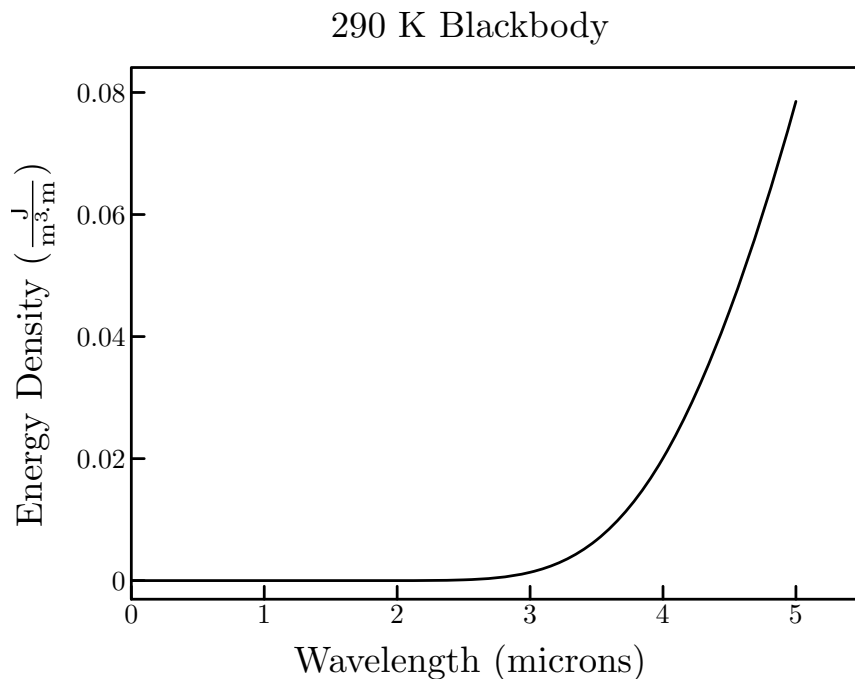


Figure 3.12: 290 K blackbody distribution. This curve illustrates the rapidly increasing thermal background over the wavelength range of the InSb guider cameras.

AE4128 comes as a complete package with a computerized readout system. This allowed development effort to be concentrated on the guiding system control software, and saved at least half a year which would have been spent on the design and construction of suitable interface electronics.

The InSb focal plane array is sensitive to radiation with wavelength λ between 1 and 5 μm . As was shown in Table 3.1, most of the sources of interest get markedly brighter with increasing wavelength. By the time λ reaches 11 μm , these are the brightest objects in the northern sky. If we consider this fact alone, it would seem best to use the entire range of sensitivity of the detector in order to maximize the collected radiation from the sources. There is another concern, however, as pictured in Fig. 3.12. The thermal background from the instrument and its surroundings (at 290 K, a typical environmental temperature) rises very steeply between $\lambda = 1 \mu\text{m}$ and $\lambda = 5 \mu\text{m}$. A third important factor is that the atmosphere has various absorption bands scattered throughout this wavelength range (Allen [1] and references therein). In order to maximize the stellar signal with respect to the background, a cold filter is used in the guider

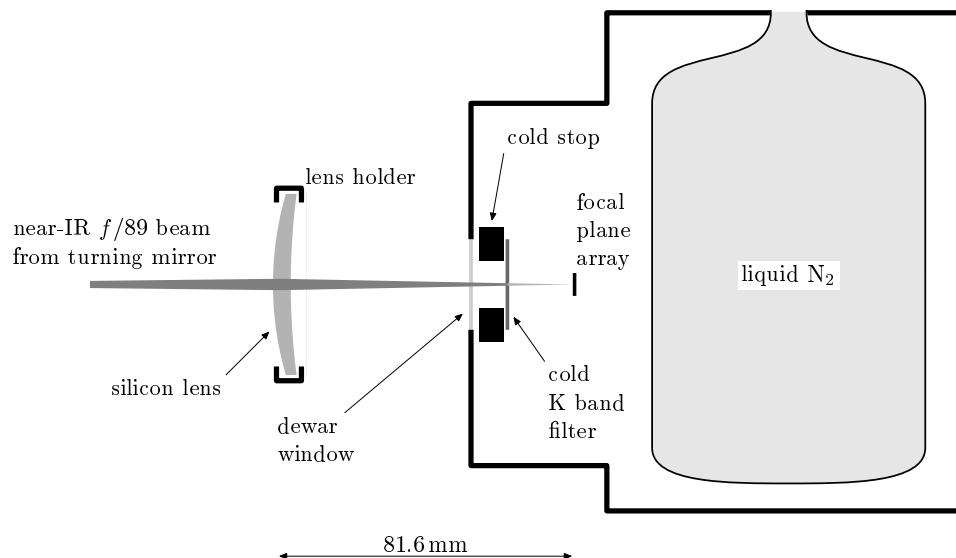


Figure 3.13: Guider camera optical system. The focal plane array and all optical components and distances are shown to scale. The $f/89$ beam from the turning mirror (Fig. 3.4) is focused by a silicon lens, through the dewar window and K band ($2.0\text{--}2.4\ \mu\text{m}$) filter, onto the focal plane array. The cold stop limits the camera focal ratio to $f/1.95$. The relatively large lens is required for the field of view, which is $39.8\times 39.8''$ on the sky.

cameras. This filter has a passband centered at $\lambda = 2.2\ \mu\text{m}$, with half-power points at 2.0 and $2.4\ \mu\text{m}$, corresponding to an atmospheric transmission window known as the “K band.”

The guider camera optical system is shown in Fig. 3.13, and the nominal specifications are given in Table 3.3. Near-infrared light from the secondary focus of the telescope, which has been transmitted through the dichroic beamsplitter and reflected by the turning mirror (Fig. 3.4), is reimaged on the camera focal plane by a custom-designed lens. The lens, which is made of silicon, is a meniscus design, with radii of curvature chosen to minimize spherical aberration and coma in this particular optical configuration. The specifications are listed in Table 3.3, and a spot diagram is shown in Fig. 3.14. As is evident from the spot diagram, the lens provides diffraction-limited image quality at the center of the field. At the very edge of the field ($20''$ off axis), the spot size (long axis) from aberrations is $180\ \mu\text{m}$. This distance on the focal plane is 1.7 times the diameter of the ISI telescope Airy disk at $2.2\ \mu\text{m}$. The edge of the field

Table 3.3: Guider camera optical system specifications.

Object distance:	359.3 mm.
Image distance:	81.6 mm.
Magnification:	$0.227 = \frac{1}{4.40}$.
Plate scale at focal plane:	$160.9 \mu\text{m}/\text{arcsec} = 0.31''/\text{pixel}$.
Field of view:	$39.8 \times 39.8 \text{ arcsec}$.
Focal ratio:	$f/1.95$.
Distance from front of camera window to lens:	52.6 mm.
Distance from lens to turning mirror:	143.4 mm.

Lens Parameters

Effective focal length:	66.5 mm.
Radii of curvature:	$R_1 = +91.0 \text{ mm}$ $R_2 = +198.0 \text{ mm}$.
Center thickness:	5.0 mm.
Diameter:	50.8 mm.
Lens holder clear aperture:	46.0 mm.
Material:	Silicon; $n = 3.45$ at $\lambda = 2.2 \mu\text{m}$.

is not used once the star has been located and locked in by the guiding system. Since the index of refraction of silicon is 3.45, the lens has been anti-reflection coated. The coating provides a transmission of more than 95% per surface over the K band (when the lens is clean).

The focal ratio of the camera, which determines the amount of thermal background radiation received, is limited to $f/1.95$ by a cold stop in the dewar (Fig. 3.13). A much smaller stop could have been used, except that the relatively large field of view is necessary for locating a star.

The camera detector consists of an array of photodiodes on an InSb substrate, each bonded to the silicon readout electronics with a small bump of Indium. A pixel in the array has a corresponding capacitor in the readout which stores the charge produced by the photodiode. During observations, the voltages on the individual capacitors are read out in turn, passed through a preamplifier (also known as the transimpedance amplifier, or TIA), and multiplexed onto one of two output lines. The gain and offset of the preamplifier are adjusted so that the output varies between -5 and 0 V .

The amplification and multiplexing take place in a small box which is attached to the camera dewar. The two outputs from this box are sent to the camera controller,

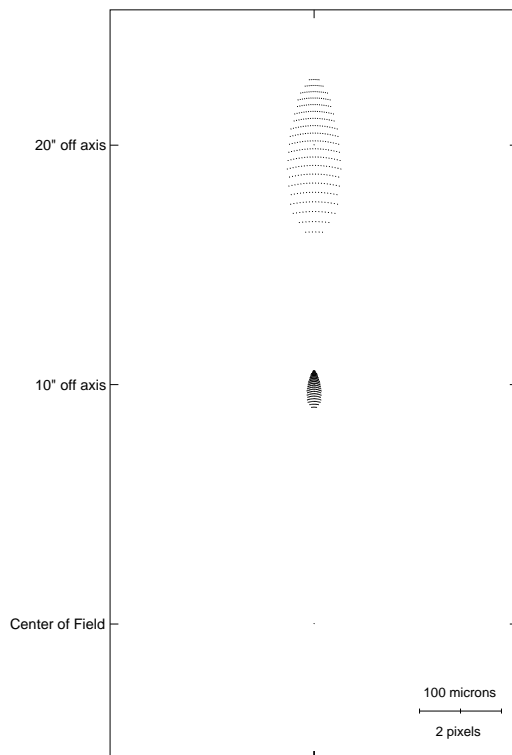


Figure 3.14: Spot diagram for the silicon guider lens. Shown here are the results of a computer raytrace of the guider lens. The size of individual camera pixels is indicated in the scale at the lower right. By comparison, the diameter of the $2.2\ \mu\text{m}$ Airy disk from an ISI telescope is $0.67''$, which corresponds to $108\ \mu\text{m}$ at the camera focal plane.

where the signals are digitized at a resolution of 12 bits (values between 0 and 4095, corresponding to inputs between -5 and 0V). A digital gain and offset are applied to the raw pixel values by the controller, and the new values are sent to the video monitor and via fast parallel data lines to an interface card in the guider PC. The image is periodically transferred from the interface card into the guider PC memory for processing. A block diagram of the camera and guiding system is shown in figure 3.15. Operating parameters for the controller, preamplifier, and camera are set by the guider PC, which sends commands to the controller computer over an RS-232 serial line.

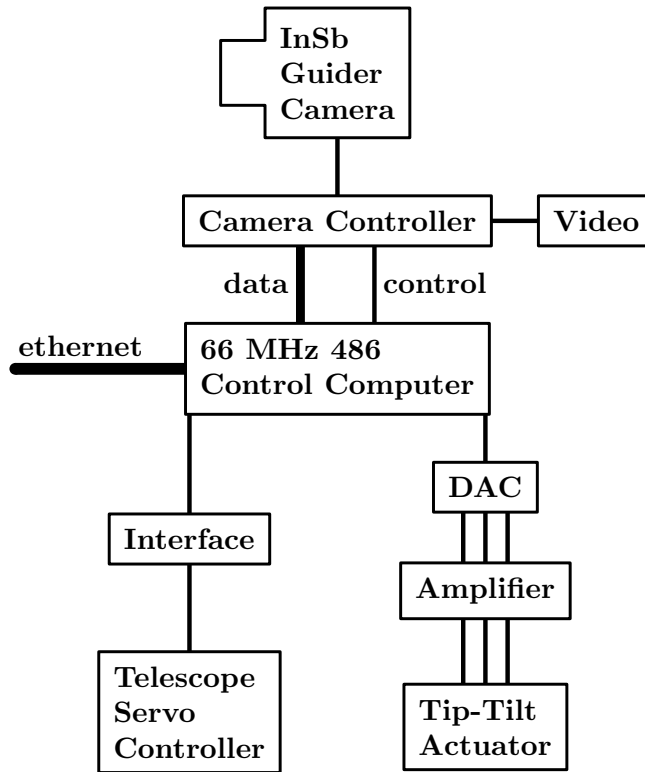


Figure 3.15: Guiding system configuration.

Tip-Tilt Actuator

Correction of the atmospherically-induced wavefront tilt of incoming starlight is accomplished by rapidly adjusting a small mirror which is mounted on a piezoelectric stage. The tip-tilt mirror is the smaller of the two Schwarzschild mirrors shown in Fig. 3.3. Figure 3.16 shows an enlarged view of the tip-tilt actuator. The actuator was manufactured by Physik Instrumente (model S-315.10, in which was drilled a small conical bore to accommodate the beam). The tip-tilt mirror is fastened to a thin, pivoting platform (not shown in the figure) at the front end of the actuator. This platform is attached to three piezoelectric stacks, each with a $12\ \mu\text{m}$ throw, positioned in an equilateral triangle. The spacing of the stacks and its placement in the optical system give the tip-tilt mirror a range of positions on the sky as shown in Fig. 3.17. In all but the very worst seeing conditions at Mt. Wilson observatory, the range of the tip-tilt mirror has been sufficient to correct for the atmospheric fluctuations. The remaining nights, during which the star

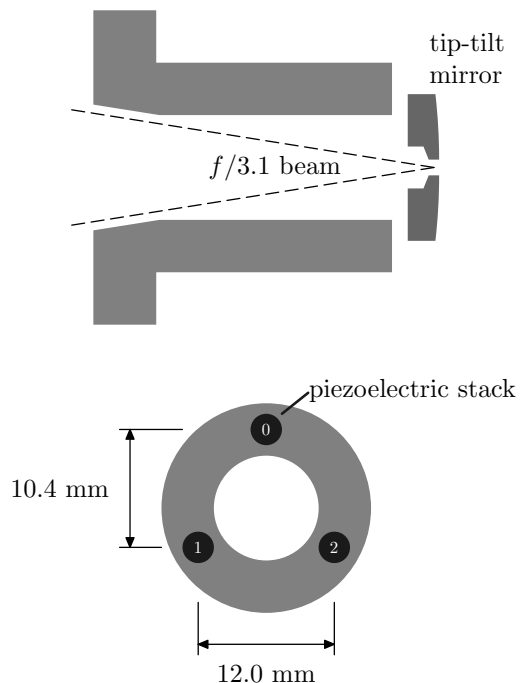


Figure 3.16: Tip-tilt actuator side and front views. Both views are drawn to the same scale. Each stack has a throw of $12\ \mu\text{m}$ along the optical axis.

image diameters vary from 5–10", do not allow the acquisition of useful fringe visibility data.

In order for it to effect a pure change in the tilt of the starlight without introducing any transverse offset for light from off-axis points, the tip-tilt mirror should be located at a pupil (Pedrotti & Pedrotti [76]) of the optical system. For a telescope, this is where an image of the primary mirror (the “entrance pupil”) is formed. Since the tip-tilt mirror was added to the existing ISI optical system, a compromise had to be made in the mirror placement. There is a virtual pupil located approximately 30 mm behind the front surface of the tip-tilt mirror (toward the paraboloid). If the wavefront from a point $1''$ from the center of the field of view on the sky is adjusted so that it is parallel to the optical axis, the 30 mm pupil offset will result in an image displacement on the guider camera focal plane of about $5.4\ \mu\text{m}$. Since the pixels in the guider camera are $43\ \mu\text{m}$ across, this displacement is negligible for any point in the ISI beam (Fig. 3.10).

During operation of the tip-tilt system, the position of the mirror is controlled by the guider PC. The PC contains a digital-to-analog converter (DAC) which produces

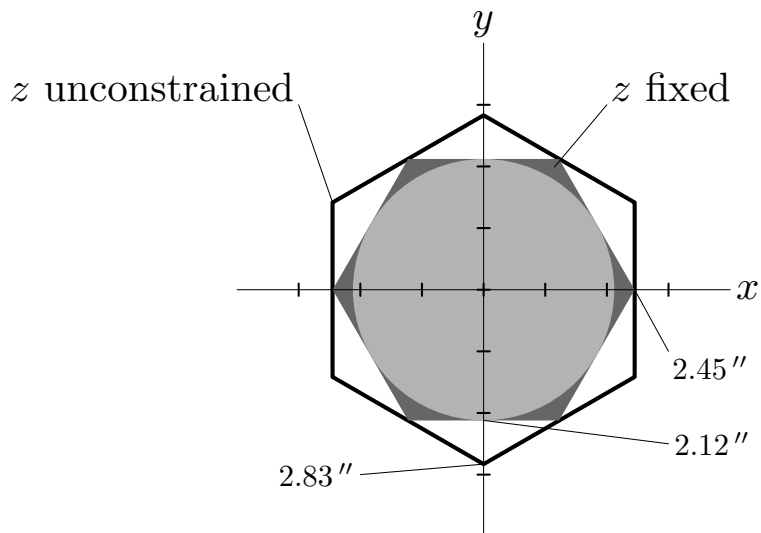


Figure 3.17: Tip-tilt range on the sky. The axis markings are spaced at $1''$. The outer hexagon encloses the region which is accessible if the mirror is unconstrained in the direction (z) along the optical axis. If the center of the mirror is fixed in position, the star can be moved anywhere within the inner hexagon. The central circle is the region in which all directions are available with z fixed, and is the range over which the tip-tilt system can move to correct the apparent position of the star.

an output between 0 and 10 V on each of three channels. The voltage from each channel is amplified by a factor of 10 and placed across one of the piezoelectric stacks in the tip-tilt actuator. The bandwidth of the amplifiers (500 Hz) and the mechanical resonance frequency of the tip-tilt stage (about 2 kHz with the mirror) both far exceed what is necessary to run the tip-tilt feedback loop at its maximum rate of 73 Hz.⁴ Tests of the system have confirmed that the computer interface, amplifiers, and mirror can operate beyond 100 Hz with no loss of performance.

3.4.2 Guider Camera Sensitivity

During the operation of the guiding system, the guider PC receives images from the cameras in the form of 128×128 arrays of values which range between 0 and 4095. The value corresponding to each pixel represents a combination of the star's near-infrared flux, the near-infrared background, and noise introduced in the detection and

⁴At a closed-loop rate of 73 Hz, a full image capture, error computation, and mirror correction cycle occurs every 13.7 ms.

amplification processes. Using these values, the PC must make a reliable determination of whether or not there is a star in the field. If there is, the star's position must be accurately determined. This is only possible if the fraction of the pixel value representing starlight is substantially greater than that representing noise.

Photon Noise

It is useful to make a quantitative comparison between the power received by the camera from the stars and that received from various sources of noise. Stars are classified using a system of magnitudes (Allen [1]). A star's magnitude indicates how much flux it produces in a given wavelength range. The magnitude system is logarithmic, and is defined such that a 100-fold increase in flux corresponds to a *decrease* of 5 magnitudes. 0 magnitude in each wavelength band is defined to correspond to the power per unit area and wavelength range delivered by the bright star Vega (α Lyrae). A specific example which will concern us is the K band magnitude. A star with $m_K = 0$ produces a flux of $3.98 \times 10^{-10} \text{ W}\cdot\text{m}^{-2}\cdot\mu\text{m}^{-1}$ just outside Earth's atmosphere. The transmission of the clear atmosphere at K band is approximately 99% (Allen [1]), so we will not consider this factor in the present analysis.

Using the ISI's collecting area of 2.14 m^2 and the $0.4 \mu\text{m}$ -wide passband of the guider camera cold filter, we find that a star with $m_K = 0$ delivers a power of $3.4 \times 10^{-10} \text{ W}$ into the ISI guider camera, not including losses in the optical system. At $2.2 \mu\text{m}$, this is equivalent to 3.8×10^9 photons per second. On a typical night, this flux would be spread by the seeing over about 50 pixels (corresponding to a circle with radius $1.24''$). Using this approximation, we would expect about

$$7.5 \times 10^7 \kappa \text{ photons}\cdot\text{pixel}^{-1}\cdot\text{s}^{-1} \text{ from a star with } m_K = 0, \quad (3.10)$$

where κ is the transmission coefficient of the optical train leading into the guider camera. Table 3.4 shows m_K and the expected photon flux per pixel for a few sources. IRC +10420 is the dimmest source on which the ISI can reliably guide in its present configuration, and α Orionis is one of the brightest sources available.

The two sources of noise which inject unwanted photons into the camera are the sky background and the thermal background from the instrument and its surroundings. A study of the K band sky background was done at Mauna Kea by Wainscoat &

Table 3.4: Expected photons per pixel per second from some ISI observing targets. κ is the transmission of the telescope optical train leading into the guider camera. These values assume that the total flux from the star is spread evenly over 50 guider camera pixels.

Source	m_κ	$\frac{\text{photons}}{\text{pixel}\cdot\text{s}}$
α Ori	-3.8	$2.5 \times 10^9 \kappa$
α Lyr	0	$7.5 \times 10^7 \kappa$
IRC +10011	+2.0	$1.2 \times 10^7 \kappa$
IRC +10420	+3.4	$3.3 \times 10^6 \kappa$

Cowie [92], and they found the flux to be consistently less than 14 mag/arcsec². This is equivalent to 26κ photons·pixel⁻¹·s⁻¹, which is completely negligible, even when one accounts for the fact that the background at Mt. Wilson is probably worse than at Mauna Kea. The thermal background turns out to be much larger. The radiation power incident on one pixel is (Kingston [48]):

$$P_b = \epsilon A \Omega \frac{2h}{c^2} \int_{\nu_1}^{\nu_2} \frac{\nu^3 d\nu}{(e^{h\nu/kT} - 1)}, \quad (3.11)$$

where ϵ is the total emissivity of the optical system, A is the area of a pixel, $\Omega = 0.197$ steradians, the solid angle of acceptance corresponding to the $f/1.95$ cold stop in the camera (§3.4.1), and ν_1 and ν_2 are the frequencies at the edges of the K band. T , the background temperature, will be taken to be 290 K. The integral in (3.11) is necessary because of the rapid rise of the 290 K blackbody distribution over the K band. Performing the integral, we have:

$$P_b = \epsilon A \Omega \frac{2h}{c^2} \cdot \frac{e^{a\nu}}{a} \left(\nu^3 - \frac{3}{a}\nu^2 + \frac{6}{a^2}\nu - \frac{6}{a^3} \right) \Big|_{\nu_1}^{\nu_2},$$

where $a \equiv -h/kT$. Using $\nu_1 = 1.25 \times 10^{14}$ Hz and $\nu_2 = 1.5 \times 10^{14}$ Hz,

$$P_b = 1.38 \times 10^{46} \epsilon A \Omega \frac{2h}{c^2} = 7.4 \times 10^{-14} \epsilon \text{ W} = 8.2 \times 10^5 \epsilon \text{ photons}\cdot\text{pixel}^{-1}\cdot\text{s}^{-1}. \quad (3.12)$$

This constant background level can be removed from the final signal, but we will still be left with a noise fluctuation of \sqrt{Nt} photons, where N is the number of background photons received per second, and t is the integration time. With $N = 8.2 \times 10^5$ from (3.12), we find a noise fluctuation per pixel from the thermal background

$$N_{\text{therm}} = 905\sqrt{\epsilon t} \text{ photons}. \quad (3.13)$$

Table 3.5: Magnitude equivalents of the thermal background noise received by the guider camera. The integration times shown are typical for the ISI guiding system. These values were computed using $\kappa = \epsilon = 0.5$.

Integration Time (ms)	m_{κ}
3.7	8.9
7.5	9.3
116	10.7
813	11.8

Using (3.10), we can compute the magnitude equivalent of N_{therm} for a given integration time. Some representative values are shown in Table 3.5. For these calculations, values of $\kappa = \epsilon = 0.5$ have been used, based on a measurement to be discussed later in this section.

As mentioned above, the dimmest star on which the ISI has been able to reliably guide is IRC+10420, at $m_{\kappa} = 3.4$. In order to have sufficiently fast response for position switching (§3.2.3), the guiding system must run the cameras at a frame rate of 7 Hz or more.⁵ Because of this, the longest usable integration time turns out to be 116 ms. Since the thermal background noise for a 116 ms integration is equivalent to a star of $m_{\kappa} = 10.7$, the system is obviously not limited by this source of noise.

Electrical Noise and System Response

The InSb detectors and readout system produce two forms of noise which are independent of the radiation impinging on the array. The first form is read noise, which is a fluctuation associated with reading out the voltage on each pixel's integration capacitor. This fluctuation is equivalent to about 600 electrons for a pixel in the ISI guider cameras. The second form of noise is associated with dark current. Dark current is caused by thermal fluctuations which produce electron-hole pairs in the InSb detectors. The dark current is thus highly dependent on temperature. The measured dark current from the camera test data supplied by Amber is 4×10^7 electrons per second at 77 K, and 1×10^5 electrons per second at 55 K for each pixel. Because of the large dark current at 77 K (enough to exceed the storage capacity from Table 3.2 in less than

⁵The ISI guider PCs run an operating system which only allows one task to be performed at a time. If an image is being acquired or the telescope is being moved, the position switching requests are ignored.

1 second), the cameras are operated slightly above 55 K except for observations of the brightest sources. This is done by lowering the pressure in the camera's liquid nitrogen container until the nitrogen solidifies. Erratic behavior of the array readout at 55 K has prevented the use of the cameras at that temperature. As was the case with the thermal background, the dark current background can be subtracted out of the final signal, but a fluctuation of $\sqrt{N_e t}$ electrons will remain, where N_e is the number of dark current electrons gathered in a pixel in one second, and t is the integration time. The InSb detectors in the Amber camera have a quantum efficiency $\eta \approx 0.75$. This number, which is the ratio of photoelectrons produced to incident photons, can be used to make a comparison between the sources of photon noise discussed earlier and the two sources of electrical noise. When this is done, assuming an integration time of 116 ms, we find that the read noise is equivalent to $m_K = 9.3$, and the dark current fluctuation is equivalent to $m_K = 11.5$ at 55 K.

The relationship between electrons stored in the pixel capacitors and preamplifier (also referred to as the transimpedance amplifier, or TIA) output voltage is given in the Amber camera manual [2]. For a flux of N photons·pixel⁻¹·s⁻¹ and an integration time t , the preamplifier output voltage change due to the received light is:

$$\Delta V_{\text{out}} = \frac{\eta e N t}{1.6C} g_{\text{TIA}}, \quad (3.14)$$

where $\eta \approx 0.75$ is the quantum efficiency, e is the charge of an electron, $C = 7.0 \times 10^{-13}$ F is the storage capacitance of the pixel, and g_{TIA} is the preamplifier gain setting. This voltage change is relative to an offset voltage at the preamplifier output. The offset voltage is adjustable, which is necessary in order to place it properly within the -5 – 0 V window of the analog-to-digital (ADC) converter (§3.4.1). We use a g_{TIA} setting of 2.57, the highest gain for which the output level can be offset to correspond to -5 V when the detector is not illuminated. Substituting known values into (3.14), we have

$$\Delta V_{\text{out}} = 2.8 \times 10^{-7} N t = 3.7 \times 10^{-7} N_e t, \quad (3.15)$$

where $N_e = \eta N$ is the number of electrons collected per pixel per second. The ADC has a range of 0–4095 data numbers (DN) corresponding to input from -5 – 0 V. Thus if the preamplifier output voltage offset is chosen such that an unilluminated pixel produces a preamplifier output of -5 V, the camera control computer will read a value

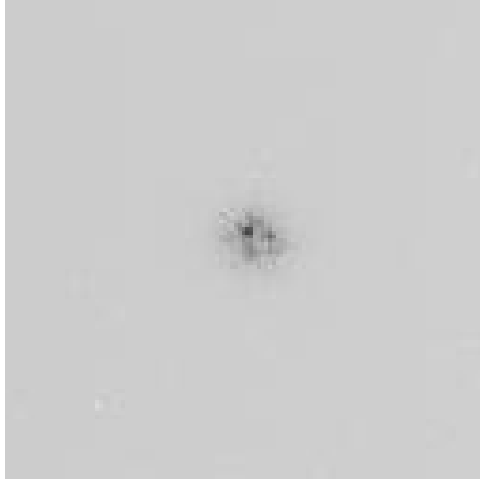


Figure 3.18: Image of α Orionis. The background level of the image was determined by averaging a region far from the center of the field, and is 802 data numbers (DN) per pixel. The total flux from the star, which does not depend on the seeing conditions, is 2.05×10^5 DN. The integration time was 15 ms. Image color has been reversed for clarity.

of

$$2.8 \times 10^{-7} Nt \text{ V} \cdot \frac{4095 \text{ DN}}{5 \text{ V}} = 2.3 \times 10^{-4} Nt \text{ DN} \quad (3.16)$$

for a given pixel.

Using the relation (3.16), we can determine the transmission κ of the guider optical system as follows. Figure 3.18 shows a guider camera image of the star α Orionis. The total flux from the star in the image is 2.05×10^5 DN in 15 ms. At $m_{\kappa} = -3.84$, α Orionis has a flux 33.1 times that of a star with $m_{\kappa} = 0$. The total flux from an $m_{\kappa} = 0$ star into the ISI guider camera is $3.8 \times 10^9 \kappa$ photons per second, so for α Orionis, the total number of photons received in 15 ms is

$$33.1 \cdot 3.8 \times 10^9 \kappa \cdot 0.015 = 1.9 \times 10^9 \kappa \text{ photons.}$$

From (3.16), we see that this corresponds to $4.3 \times 10^5 \kappa$ DN when we sum over all the pixels in the array. Comparing this value with the flux measured in the image, we find

$$\kappa = 0.48.$$

Other measurements taken on the same night show a variation of up to 10% in the measured flux, presumably due to the method of determining the background level of

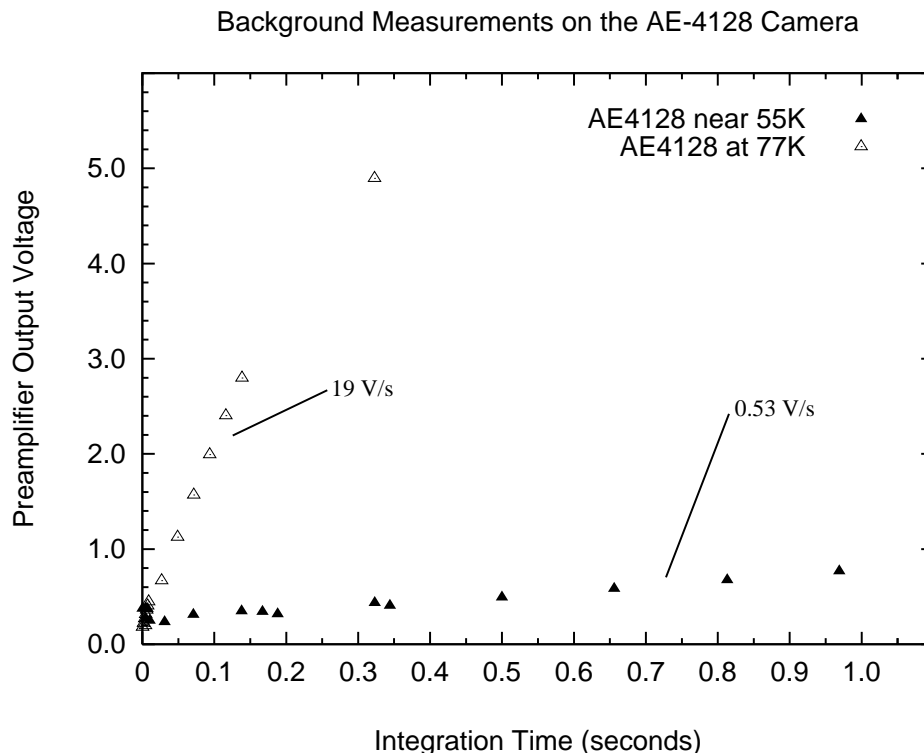


Figure 3.19: Background measurements on the AE4128 camera. The large background at 77 K is dominated by dark current.

the image, which was to average an area far from the center of the field. This value for κ is reasonable, considering that the starlight encounters 11 optical surfaces on the way to the InSb detector. The equivalent average loss per surface is about 6.5%. If we assume that the losses are mostly due to absorption (the transmissive surfaces are all anti-reflection coated), we can estimate that the emissivity $\epsilon \approx 1 - \kappa \approx 0.5$.

Figure 3.19 shows the results of a measurement of the preamplifier output voltage for various integration times at 77 K and just above⁶ 55 K, at the point where the behavior of the readout stabilizes. The background level at 77 K is dominated by dark current. A fit to the points taken near 55 K shows an increase in the background level of 0.53 V/s. We can estimate the theoretical increase in 55 K background voltage with integration time by adding the contributions of the thermal radiation and the dark

⁶This temperature has not been measured, but is thought to be between 55 and 60 K based on the large decrease in dark current readings and time required to reach the optimal temperature as the camera is cooled below 77 K.

current. From (3.12), we expect $8.2 \times 10^5 \epsilon$ photons·pixel⁻¹·s⁻¹ of thermal background. In this case, it is appropriate to use $\epsilon = 1$, since the blackened lens cap was on the camera for these measurements. Using $\eta = 0.75$, we get a contribution of 6.4×10^5 electrons per second in each pixel. The dark current is expected to be 10^5 electrons per second, so the total time-dependent background is 7.4×10^5 electrons per second. Using (3.15), we find an equivalent voltage rise of 0.27 V/s, which is about half the observed value.

Two possible sources of this discrepancy are the temperature of the array and the temperature of the surroundings. The dark current grows exponentially with temperature, and increases by a factor of 400 between 55 K and 77 K. Therefore, it would only be necessary for the array to be at 61 K to produce the 8-fold increase in dark current required to explain the observed voltage. The K band thermal background radiation would roughly double if the temperature of the surroundings increased from 290 to 300 K. Although it was probably not 300 K in the telescope trailer on the evening of 2 May 1997 when the measurements were performed, it might have been 295. Unfortunately this information was not recorded, but the resulting uncertainty could account for part of the observed background excess.

From the measured background, we can calculate the K band stellar magnitude which would yield a signal-to-noise ratio of 1. With a background of N_e electrons per second on one pixel, the noise fluctuation would be $\sqrt{N_e t}$ electrons for an integration of duration t . The background voltage increase of 0.53 V/s is equivalent to $N_e = 1.4 \times 10^6$ electrons per second on one pixel from (3.15), thus the noise fluctuation due to this level is $1200\sqrt{t}$ electrons. Since the lens cap is obviously not used during observations, this value must be adjusted. Reverting to $\epsilon = 0.5$, and assuming that half the total background is due to thermal radiation, we get $N_e = 1.1 \times 10^6$, and the fluctuation becomes $1000\sqrt{t}$ electrons. To this we add the read noise of 600 electrons to get the noise equivalent charge on a pixel

$$q_n = 600 + 1000\sqrt{t} \text{ electrons} \quad (3.17)$$

Noise equivalent K band magnitudes, calculated using (3.17), (3.10), $\kappa = 0.5$, and $\eta = 0.75$, for various values of t , are shown in Table 3.6

Table 3.6: Magnitude equivalents of the total background noise received by the guider camera.

Integration Time (ms)	m_K
3.7	5.5
7.5	6.2
116	8.8
813	10.5

System Limitations and Possible Improvements

In order that tip-tilt corrections take place at a rate fast enough to compensate for atmospheric fluctuations, the guiding system must be able to determine the position of a star in the camera image using a relatively simple algorithm. Such an algorithm, despite its simplicity, must be able to reliably pick out the star from the background. It turns out that the major obstacle to this task does not come from background noise, but rather from “flickering pixels” and non-uniformity in the camera response. Flickering pixels are those which routinely exhibit noise greater than 10 times the mean for the rest of the array. The ISI guider cameras have on the order of 10 such bad pixels each, which are not removed by the camera calibration procedure. Figures 3.20 and 3.21 illustrate a typical image of a dim ($m_K = 3$) star. The camera non-uniformity correction,⁷ which compensates for slight differences in the individual InSb detectors, begins to degrade after a few hours of operation. This degradation can result in small patches with higher than average response, which must be distinguished from the star image. Experience has shown that reliable guiding requires a signal-to-noise ratio (background noise) of between 5 and 10.

If we use this requirement, and say that the ISI can guide on a star 2 magnitudes (a factor of 6.3) brighter than the noise-equivalent magnitude (Table 3.6), we would estimate that for an exposure of 116 ms, the limiting magnitude should be $m_K = 6.8$. The actual limit for the ISI has been $m_K = 3.4$. The cause of this problem turns out to be the limited gain available with the preamplifier in the Amber system. In the present configuration, the image of an $m_K = 3.4$ star on the focal plane array

⁷This procedure, which is described in the Amber camera manual [2], uses a uniformly illuminated array image and a dark image to compute correction values for each pixel in the array. These corrections are then automatically applied by the camera control computer to the level of each pixel before the data are sent to the guider PC.



Figure 3.20: Background-subtracted guider camera image of an $m_K = 3$ star. The star is at the center of the field of view. This image illustrates the flickering pixels and non-uniformity which the guider can mistake for a star. Figure 3.21 shows a histogram of the data from this image. Color has been reversed for clarity. The integration time was 138 ms.

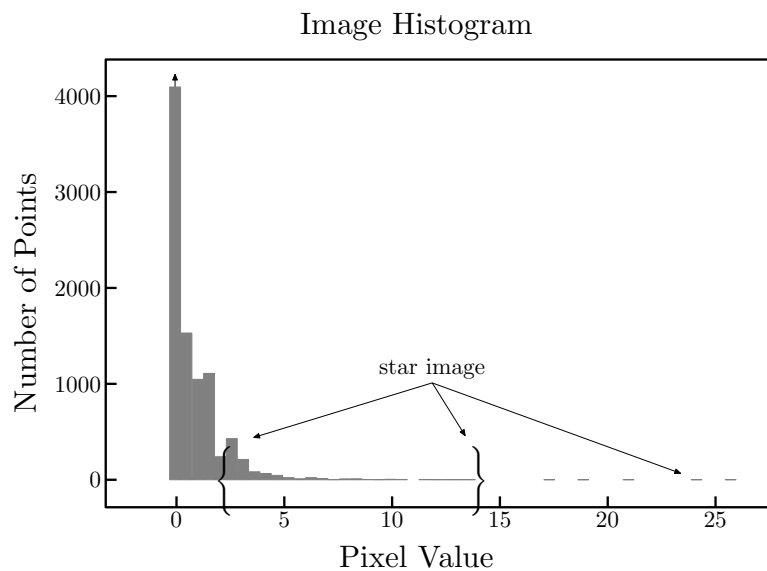


Figure 3.21: Histogram of the image shown in Fig. 3.20. The bins from pixels in the star image fall within the braces, except for one pixel with a data number of 24. The large pixel values not associated with the star are caused by flickering pixels.

results in preamplifier output of about 0.05 V if the seeing is reasonably good. This corresponds to a data number of 41, which is a very small fraction of the maximum 4095. Although this gain is usable over the entire range of stars which the ISI observes, much of the image of a dim star can get lost in the noise, making the few remaining bright pixels difficult to distinguish from flickering pixels and non-uniformity.

If at some point in the future, the cameras are equipped with amplifiers that have higher gain and larger offset range, it should be possible to have an increase of about 3 magnitudes in sensitivity. This would allow observations of a large number of new sources, and would enable tip-tilt correction on stars which are now at the limit of detection for the system.

3.4.3 Guiding System Software

Well over half the time and effort required to build the ISI guiding and tip-tilt correction system was spent designing, writing, testing, and debugging the code which manages the hardware devices described earlier in this chapter. The control software for this system consists of two separate programs, the user interface, which runs on one of the control workstations, and the `isiguide` program, an identical copy of which runs on a personal computer (the guider PC) in each telescope. These programs communicate with each other and with the real-time computers in order to operate the guiding system in synchrony with the star tracking and data collection.

The User Interface

A multithreaded program called `yguider`⁸ provides a graphical user interface to the guiding system functions. This program runs on the control workstation under Sun Microsystems's Solaris variant of the UNIX operating system. Because it is multithreaded, `yguider` can carry out a number of tasks concurrently, such as the delivery of commands to two separate computers. The control panel presented to the user is shown in Figure 3.22.

The function of the `yguider` program is relatively simple. When the operator presses one of the buttons on the control panel, `yguider` sends a command or short sequence of commands (documented in Appendix B) over the network to one or more

⁸`yguider` is the successor to the original version of the program, which was called `xguider`, since it ran under the X window system.

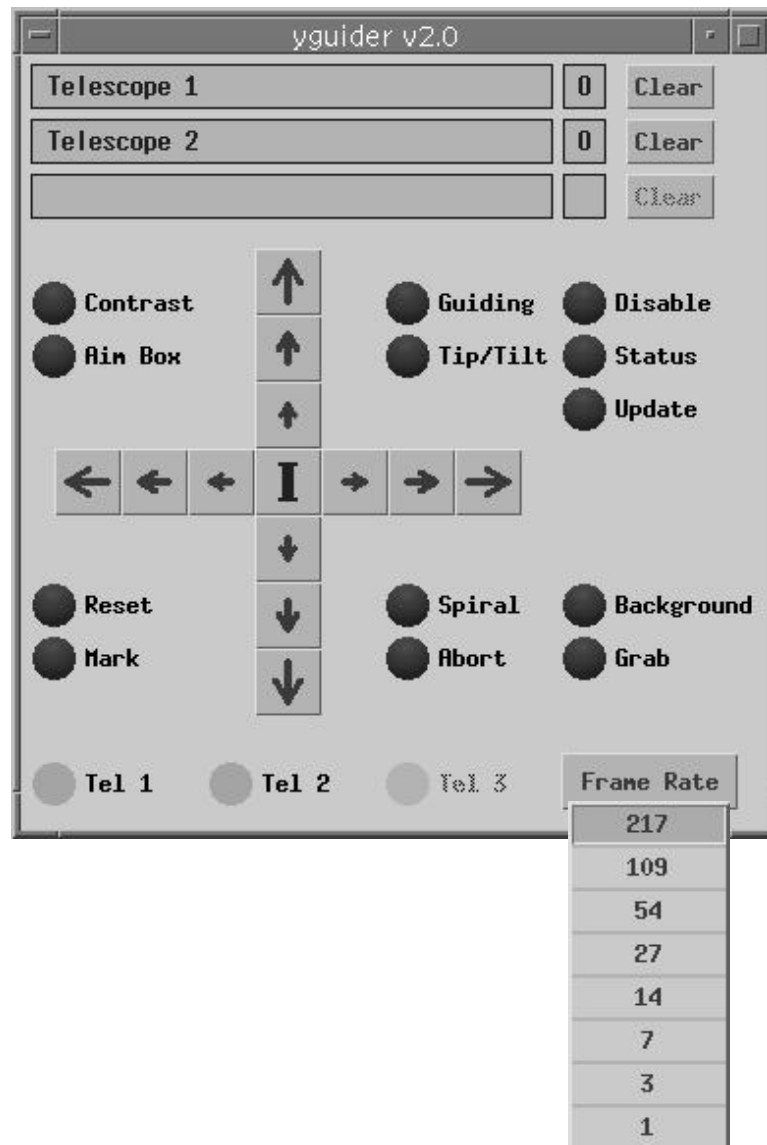


Figure 3.22: The `yguider` interface. The buttons and menu shown here allow the telescope operator to control the guiding and tip-tilt systems remotely. Status messages and queued command counts appear at the top of the control panel.

of the guider PCs. Many of the network commands have keyboard equivalents which can be used at the guider PC console. Error messages and a count of the commands queued for delivery to each PC are shown in small windows at the top of the panel. The arrow buttons allow the operator to move the star image on the guider camera screen (by moving the telescope) when the guiding is disabled.

The isiguide Program

The `isiguide` program runs on the guider PCs, which are currently 66 MHz Intel 486-based personal computers. These computers use the MS-DOS operating system, which, in contrast with UNIX, is a single-tasking environment, where there is only one thread of execution running on the machine at any one time. This limitation presents a number of difficulties, but the alternatives were prohibitively expensive at the time when the system was being designed.

During the design of `isiguide`, care was taken to keep it as independent of the rest of the ISI system as was possible. The program is actually unaware of which telescope it is controlling, and therefore the code can be identical on both guider PCs. All network communication with `isiguide` takes place over transient connections, which are closed after the message has been delivered. This allows the program to continue running even if the other ISI computers must be reset. In its present configuration, `isiguide` operates as a server, which means that it receives requests from other computers, but does not call out on its own. Because the guider PC operating system is single-tasking, when a message comes in from the network, all other functions of the computer are suspended until the message has been received. To maintain independence, a strict 3 second time limit is placed on all network connections. This is normally far more time than is necessary.

Within the constraints imposed by the guiding system hardware and the ISI telescopes, `isiguide` must carry out the following tasks:

- Control the camera. All communication between the camera and any part of the ISI system ultimately goes through `isiguide`. The appropriate frame rate, integration time, and gain and offset parameters for the source under observation are set by the operator using the `yguider` interface. The guider camera image is also made available through the `isiguide` network interface.

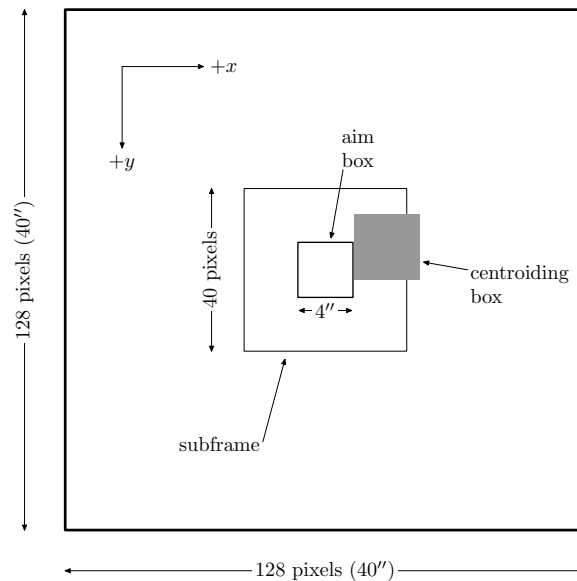


Figure 3.23: Guider camera field of view. The screen is described by a coordinate system with its origin at the upper left of the image (the axes pictured indicate direction). When in the guiding and tip-tilt loops, `isiguide` only acquires the outlined subframe, and computes a centroid about the assumed position of the star (the offset shown here is used for position switching during background measurements). Pixels in the centroiding box which are outside of the subframe are ignored. The aim box can be made visible on a video screen which is fed by the camera control box (Fig. 3.15).

- Locate the star. When properly calibrated, the ISI tracking system is usually able to point accurately enough that the star falls somewhere within the 40'' square guider camera field of view (Fig. 3.23). The `isiguide` program must pick out the star in the camera image and center it by moving the telescope.
- Adjust the telescope. In addition to compensating for small errors in star tracking, `isiguide` must move the telescope for the position switching and beam mapping procedures. During position switching, which is synchronized with data collection and controlled by the real-time computers, the star is moved between the center of the field and an offset position which corresponds to a 5'' motion in azimuth on the sky. This allows a background subtraction in the mid-infrared. Beam mapping, which is managed by the control workstation, checks that the 11 μm and 2.2 μm images are properly aligned relative to one another.

In order to properly control the telescope, `isiguide` must be able to determine the

relationship between the screen coordinate system and the altitude and azimuth directions on the sky. In addition, the program must know the transformation between the telescope altitude and azimuth axes and the sky altitude and azimuth axes. This transformation depends on the current star position, of which `isiguide` is unaware. The necessary information is periodically delivered, in the form of a field rotation angle and a 4-element transformation matrix, to `isiguide` by the real-time computers, which run the star tracking calculations.

- Drive the tip-tilt mirror. The `isiguide` program is solely responsible for driving the tip-tilt mirror in order to stabilize the star image at the center of the camera field of view.

Input and Output

The guider PCs have a number of input and output devices which `isiguide` uses to perform the tasks listed above (see Fig. 3.15):

- Camera control serial line. The camera control computer provides a set of terse commands (documented in the Amber camera manual [2]) by which it can be managed. The `isiguide` program sends these commands over an RS-232 serial line to the control box in order to adjust the frame rate, digital gain and offset coefficients, integration time, and other operating parameters.
- Frame grabber card. The guider PC contains a fast interface card (Dipix P360F) with its own on-board processor and memory. This card receives digital image data, at rates up to 4 million pixels per second, on a parallel cable from the camera control box. The data are stored in card memory until `isiguide` requests a transfer to the guider PC's own memory.
- Telescope servo interface. Communication between `isiguide` and the telescope servo microprocessors takes place through a custom-designed device which uses a microcontroller to simulate the output of a joystick. By sending commands over an RS-232 serial line to this interface, `isiguide` can change the altitude and azimuth of the large flat mirror in units of encoder counts. The encoders, which keep track of the position of the flat mirror, read out in counts which correspond

to a small fraction⁹ of an arcsecond.

- **Tip-tilt DAC.** The tip-tilt mirror (§3.4.1) is controlled with a digital-to-analog converter (DAC). Three 12-bit (0–4095) numbers, sent by `isiguide` to the DAC, determine the voltages (0–100 V) on the three piezoelectric stacks in the tip-tilt actuator (Fig. 3.16). To place the star image at a position (θ_x, θ_y) on the screen (in arcseconds, referenced to the position with no mirror tilt), `isiguide` sends the best integer approximations of the following counts to the three DAC channels:

$$\text{DAC}_0 = 2047.5 + 965.7 \theta_y$$

$$\text{DAC}_1 = 2047.5 - 836.1 \theta_x - 481.2 \theta_y$$

$$\text{DAC}_2 = 2047.5 + 836.1 \theta_x - 481.2 \theta_y$$

These equations constrain the middle of the tip-tilt mirror to a position on the optical axis, $6 \mu\text{m}$ from either end of the range ($12 \mu\text{m}$) of the piezoelectric stacks.

- **Local area network.** All communication between `isiguide`, the real-time computers, and the control workstation takes place over a local area network, which uses the Ethernet protocol. The `isiguide` network interface is discussed in detail in Appendix B.

Modes of Operation

The `isiguide` program runs in one of the following modes, depending on the source under observation, whether the star is in the field of view, and what behavior is desired by the operator.

- **Disabled.** In the disabled mode, `isiguide` acquires images, updates the display, and responds to commands from the network, including requests to move the telescope and tip-tilt stage. It does not attempt to make any changes on its own.
- **Searching.** Once the operator enables the searching mode, `isiguide` goes into the loop pictured in Fig. 3.24. The first step in the search is to adjust the contrast

⁹This fraction, which is $\approx 1/30$ for altitude and $1/35$ for azimuth, is determined accurately when the telescopes are calibrated. This calibration procedure involves pointing at a large number of stars, noting the positional errors, and fitting the free parameters which determine the telescope position (Bester [10]). The real-time computers (§3.3) deliver the necessary information to the guider PCs over the network.

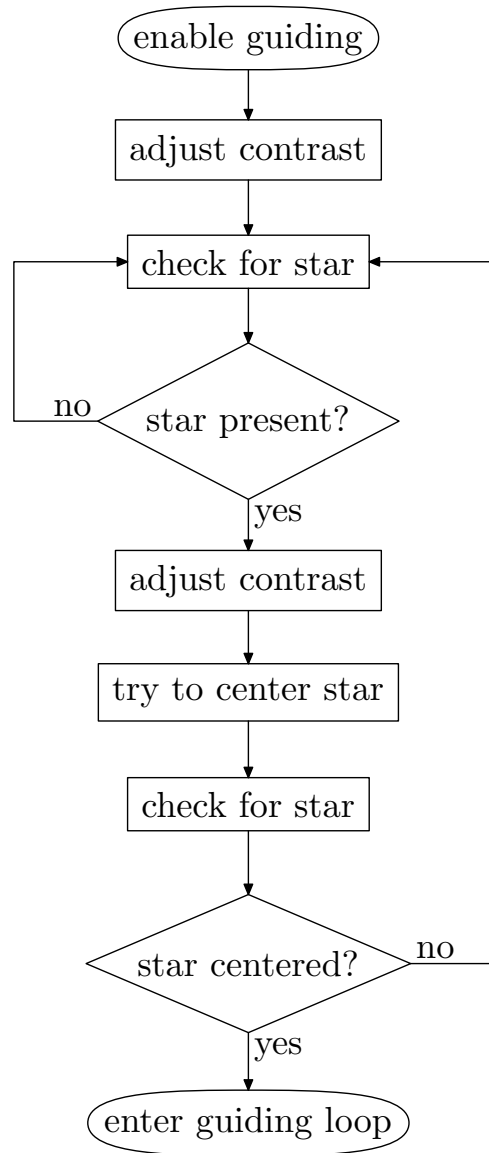


Figure 3.24: Star search flow chart. See the text for a description of this procedure.

by increasing the digital gain applied by the camera control computer. This is especially necessary when switching from a bright to a dim star, since the gain will have been set to a value which would prevent the dim star from being seen. Next, an image is acquired and `isiguide` checks for the presence of a star (the algorithm is described below). If a suitable candidate is found, the contrast is again adjusted in order to prevent the saturation which would be caused by a bright target star. The telescope is then moved such that the star, if real, will appear at the center of the screen. If a centered star is detected, `isiguide` changes its status to “locked,” and enters the guiding loop. Otherwise, it resumes the search. If the star is not initially present on the guider camera screen, the operator can instruct `isiguide` to do a spiral search, as described below.

- Locked. The locked, or guiding, mode is entered after a star has been found and centered. In this mode, as well as in tip-tilt mode, `isiguide` only acquires a small subframe instead of the entire screen image (Fig. 3.23). This cuts down on the number of flickering pixels in the image, and allows the correction loops to run faster. The subframe which was chosen (40 pixels on a side) is the largest which will allow the tip-tilt loop to run faster than 70 Hz.

A cycle of the guiding loop (similar to the tip-tilt loop pictured in Fig. 3.25) begins with the acquisition of a subframe from the guider camera. At any given time when `isiguide` is locked, it has a concept of where the star is supposed to be. Usually, this is at the center of the subframe, but at certain times, for example during position switching (Fig. 3.23), the star is somewhere off-center. A centroid is calculated for the pixels in a small box (presently 16 pixels on a side) about the assumed position, and the offset of the centroid from this position is stored in an array. A number of statistics are then calculated for the image, and these statistics are displayed on the guider PC screen along with the subframe. Finally, `isiguide` checks the keyboard and network for pending commands. Every 3 seconds, the most recent stored offsets in the array (currently the last 10, or however many there are if the frame rate is low) are averaged, and the telescope is moved in order to correct for the average offset. The ISI star tracking drifts only about 5'' in half an hour, so this correction rate is more than adequate to compensate for any such drift.

- **Tip-tilt.** Once `isiguide` is in locked mode, the operator can activate the tip-tilt loop, which is shown in Fig. 3.25. When operating in this mode, `isiguide` executes two nested feedback loops. In the inner loop, which runs at rates up to 73 Hz, a subframe is acquired, a centroid offset is calculated (as described above), and a correction is made to the tip-tilt mirror angle. This cycle repeats a fixed number of times (about 100, depending on frame rate) before the outer loop runs through its cycle. The telescope is adjusted once during each cycle of the outer loop, in order to remove the average angular offset of the tip-tilt mirror. The serial control flow used in the tip-tilt mode is necessary because of the single-tasking operating system. It would be much better to have the inner and outer loops running concurrently, with no pause in the tip-tilt correction.

It has been pointed out by Christou [22] and Close *et al.* [23] that tip-tilt correction for imaging systems is more effective if the brightest pixel, rather than the centroid, is followed. For the ISI, however, centroid tracking has resulted in better performance over a wide range of seeing conditions. With its single-element detectors, the ISI faces a different problem than does an imaging system. A large fraction of the uncertainty in ISI fringe visibility measurements is due to fluctuations in the measured infrared power, and centroiding ensures that the maximum possible energy from the star will consistently fall on the detector.

- **Chopping.** This mode, which has not been carefully tested and should be considered experimental, rapidly throws the star in and out of the center of the field of view using the tip-tilt mirror. It is designed for measuring the infrared power of the star. After 100 chopping cycles, `isiguide` pauses to check for network commands and to adjust the position of the flat mirror to keep the star centered. This pause can be heard as a small glitch in the buzzing of the tip-tilt actuator. It would not be necessary under a multitasking operating system.

Selected Algorithms

Some of the procedures which `isiguide` uses to make decisions and control operation of the guiding system are listed below.

- **Star detection.** Figure 3.26 illustrates the procedure used to pick the star out

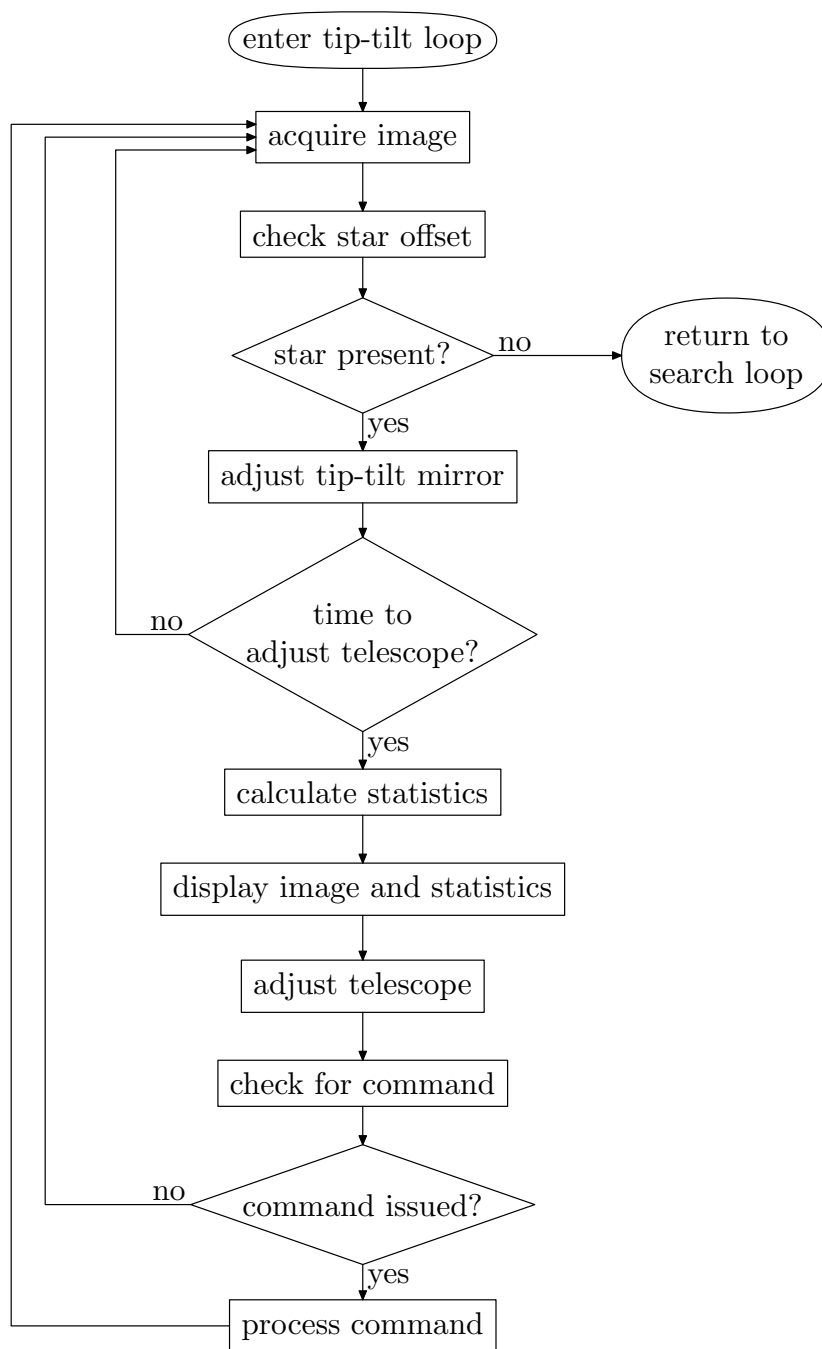


Figure 3.25: Tip-tilt loop flow chart. The guiding loop is similar, except that the calculations, display, and command check are done each time an image is acquired. Also, the tip-tilt mirror is not adjusted in the guiding loop. See the text for more details.

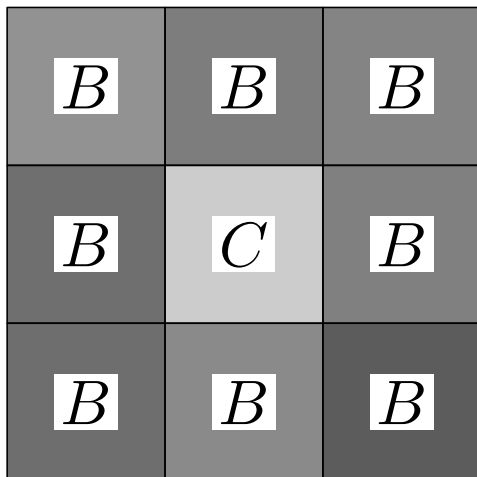


Figure 3.26: Star detection algorithm. To pick a star out of the guider camera image, `isiguide` cycles down through the brightest pixels in descending order of brightness. For each candidate pixel (C in the diagram), the border pixel (B) values are summed, and the first pixel whose border sum is between 3 and 8 times its value is chosen.

of a guider camera image. Starting with the brightest pixel in the image as a candidate,¹⁰ `isiguide` sums the values of the adjacent pixels. If this sum is between 3 and 8 times the value of the candidate pixel, a centroid is computed for a small region around the candidate, and the centroid location is used as the position of the star. If the test fails, the candidate pixel value is set to 0, and the brightest remaining pixel becomes the candidate. Up to 16 pixels are tested in this manner before `isiguide` rejects the image as containing no star. Doubtless there are more sophisticated and robust algorithms possible, but this one is simple and fast, and has proven fairly accurate over a wide range of conditions. As described above, after a star position is chosen, `isiguide` tries to center the candidate by moving the telescope. Success indicates a very high probability of a real star in the field.

- Spiral search. Telescope pointing calibration is typically done once every few months. Between calibrations, the accuracy of the pointing degrades, and eventually, the telescope is unable to place the star image within the 40'' field of view

¹⁰If there are no pixels with data number greater than 5 (out of 4095) at the camera control box ADC, `isiguide` rejects the image as containing no star.

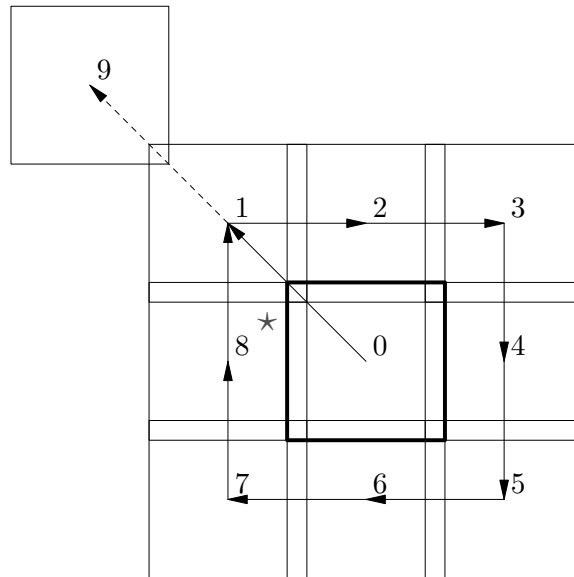


Figure 3.27: Spiral search. The guider camera field of view is moved in the sequence shown above. A star in the indicated position in field 8 would not be found until the end of the first cycle. The edge of the centered field is 40'' wide.

of the guider camera. In order to locate the star when this happens, `isiguide` can execute a spiral search, as shown in Fig. 3.27. If the image is not found in the center position, the telescope is moved so that the field of view shifts to position 1 in the figure. A small overlap is used between the fields. In each field, `isiguide` takes two frames and checks for the presence of a star before moving on. A star in the indicated position in Fig. 3.27 would not be found until the end of first cycle. This can occasionally aggravate the operator, because as the telescope moves to field 1, the star can be seen on the video screen (Fig. 3.15), which is constantly updated by the camera control computer. The guider PC, which is single-tasking, can not acquire an image until it has finished moving the telescope, so it will therefore not see the star until much later. It has been suggested (Monnier [67]) that the spiral begin with field 2, thus avoiding the psychological problem. This would actually be more efficient, and should be implemented in the future, since it prevents the duplication of the check in frame 1. The avoidance of a glimpse of the star is still not guaranteed, however, because the telescope axes are moved one after the other to shift the field, and they do not correspond to the screen

axes upon which the search is based.

- Star loss. During guiding and tip-tilt correction, `isiguide` must be able to detect the loss of the star from the field of view. As described earlier, after the star is locked in, its position is determined by finding the centroid of a small box, centered about the assumed position of the star. While doing this (in the same summation loop), `isiguide` compares the average pixel value in the centroiding box (Fig. 3.23) with the average value in the subframe. If the source is in the centroiding box as expected, the average value for the box should be greater than that for the subframe. If the box mean value is less than $1.25(m_s + 1)$, where m_s is the mean value in the subframe, `isiguide` assumes the star has been lost. If it remains lost for 5 consecutive frames, `isiguide` returns to search mode. This simple check has been extremely robust, regardless of the source under observation.

3.4.4 Guiding System Performance and Data Quality Improvement

Despite a number of shortcomings, the new ISI guiding system has enabled observations on stars which were impossible to detect with the silicon CCD camera. Fringe visibility measurements on IRC +10011 and IRC +10420 will be discussed in detail in Chapter 5. Visibility curves have also been measured for IK Tauri (Hale *et al.* [34]), on which the operator was previously forced to guide by hand, since the CCD image was too dim for autoguiding. Some preliminary work has been done on CIT 6 (see Appendix A) and R Cancri, and more data will be taken on these sources in the near future.

The tip-tilt system has provided a substantial improvement in the quality of data taken on bright targets. The system can be used on sources brighter than magnitude 0 in K band (4.5×10^9 photons per second incident on the primary mirror). Figure 3.28 and Table 3.7 show test results for three nights when the tip-tilt system was turned off for short periods of time during observations of α Orionis.

The fringe visibility values shown for each night are raw data, and were taken consecutively, with no delay between the “on” points and the “off” points. These measurements, taken on a total of 5 nights (two not shown) under varying seeing conditions, demonstrated that the tip-tilt system provides an average increase of 40% in the mid-infrared power received by the signal detectors. As can be seen from the error bars in Fig. 3.28 and the corresponding numbers in Table 3.7, the RMS fluctuations in the

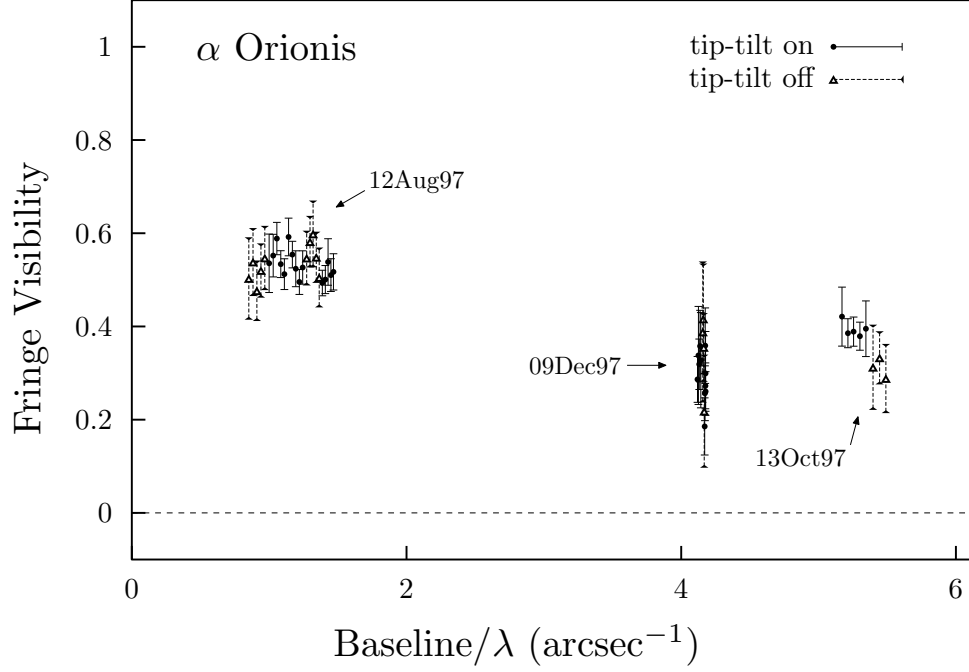


Figure 3.28: Tip-tilt tests on α Orionis. Observations with the tip-tilt system off are shown in gray.

Table 3.7: Results from tip-tilt testing on α Orionis.

Date	Tip-tilt	IR Power		RMS Visibility Fluctuation
		Telescope 1	Telescope 2	
12 Aug 1997	on	35.9	77.0	0.037
	off	27.5	53.2	0.063
13 Oct 1997	on	25.0	85.0	0.043
	off	20.2	65.4	0.071
9 Dec 1997	on	25.2	165.5	0.070
	off	13.5	93.5	0.113
Average ratio on/off		1.41	1.54	0.607

fringe visibility measurement drop by about 40% when the tip-tilt system is on. Although improvement was always seen when the system was in use, the magnitude of that improvement varied widely (e.g. increase of IR power between 12% and 96%) depending on the seeing conditions.

The data at the longest baseline in Fig. 3.28 show a marked increase in fringe visibility when the tip-tilt system is on. This is most likely due to the fact that at the longer baseline, there are more atmospheric fluctuations which are not correlated between the two telescopes. Such fluctuations produce a relative phase shift in the starlight, and a resulting change in visibility. The tip-tilt system compensates for some of these fluctuations, keeping the star images centered on both detectors. This enables a more accurate visibility measurement.

During these tests, the tip-tilt system was run at a closed-loop rate of 73 Hz. No significant difference was seen when the system was run at 55 Hz, and the results at rates lower than this varied depending on seeing conditions.

An illustration of the scientific value of the tip-tilt system is given by Figs. 3.29 and 3.30. Figure 3.29, taken from Bester *et al.* [8], shows data taken on α Orionis during the first six years of operation of the ISI. The short-baseline data are used to distinguish between two different models (see Chapter 4), which demonstrate a change in the surroundings of the star between 1992 and 1994. Although a difference in the overall level of the visibility curve is indicated between 2 and 4 spatial frequency units (0.97–1.9 arcsec⁻¹), the details of the shape of the curve are not as convincing. Figure 3.30 shows the measured visibility curve from the 1997 observing season, taken with the tip-tilt correction system. The resulting uniformly small probable errors and self-consistent shape of the short-baseline visibility curve are readily apparent.

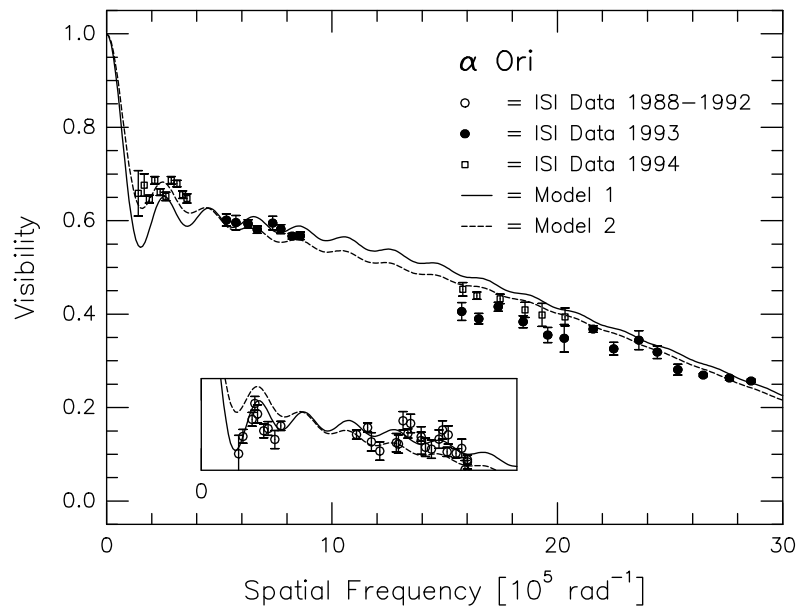


Figure 3.29: α Orionis visibility data from 1988–1994 (Bester *et al.* [8]). These data show a change in the stellar environment between the earlier period (1988–1992) and 1994. The inset shows the short baseline data from the earlier period. The change between the two epochs is indicated by the two differing models. One spatial frequency (effective baseline/wavelength) unit, as used in this plot, is equal to 0.48 arcsec^{-1} .

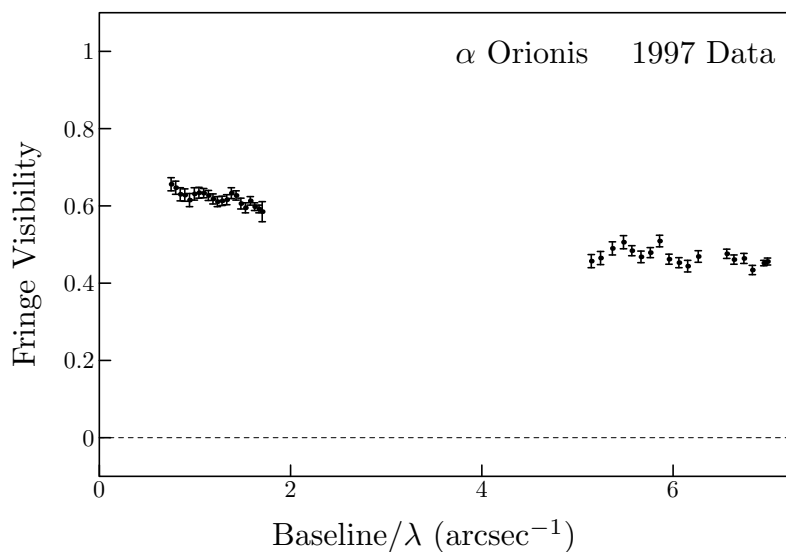


Figure 3.30: α Orionis visibility data from 1997. This partial visibility curve was acquired using the tip-tilt correction system. Compare with Fig. 3.29.

Chapter 4

Reduction of ISI Data

4.1 Obtaining Fringe Visibility Measurements from ISI Data

4.1.1 Theory

The ISI computers digitize and record three signals during observations, the infrared power signals \mathbf{IR}_1 and \mathbf{IR}_2 , and the fringe signal \mathbf{F} (§3.2.1). From these signals and a calibration, we derive the fringe visibility of the source.

As was described in §3.2.3, the fringe signal \mathbf{F} is held at 100 Hz by the lobe rotator. In order to eliminate unwanted noise in \mathbf{F} , the power spectrum of the digitized signal is integrated over a small band about this frequency to determine the *fringe power* \mathbf{FP} . The bandwidth of \mathbf{F} depends on the atmospheric conditions (Fig. 2.5), and power can be present up to 20 Hz from the center frequency on a poor night. A bandwidth of 10 Hz is a good compromise, since it will capture all the fringe power on nights with acceptable conditions, but not let in enough noise to drown weaker fringe signals. The data presented in Chapter 5 were all analyzed using a 10 Hz bandwidth.

It was shown in §3.2.3 that for a point component¹ of the source,

$$\mathbf{F}_p \propto A_{1p}A_{2p} \cos(\phi_{1p} - \phi_{2p}),$$

¹Here subscripts are reintroduced in order to distinguish the signals due to a single point p in the source brightness distribution $B(\xi, \eta)$ from the complete signals resulting from the sum over all such points.

where A_{1p} and A_{2p} are proportional to $E_{sp}E_{LO}$ at the corresponding telescope. Thus,

$$\mathbf{FP}_p \propto A_{1p}^2 A_{2p}^2 \cos^2(\phi_{1p} - \phi_{2p}) \quad (4.1)$$

Also,

$$\begin{aligned} \mathbf{IR}_{1p} &\propto A_{1p}^2 & \text{and} \\ \mathbf{IR}_{2p} &\propto A_{2p}^2. \end{aligned} \quad (4.2)$$

Combining \mathbf{IR}_{1p} , \mathbf{IR}_{2p} , and \mathbf{FP}_p , we can define

$$V_p \equiv \sqrt{\frac{\mathbf{FP}_p}{\mathbf{IR}_{1p} \cdot \mathbf{IR}_{2p}}} \quad (4.3)$$

Using (4.1) and (4.2), we have

$$\begin{aligned} \sqrt{\frac{\mathbf{FP}_p}{\mathbf{IR}_{1p} \cdot \mathbf{IR}_{2p}}} &\propto \sqrt{\frac{A_{1p}^2 A_{2p}^2 \cos^2(\phi_{1p} - \phi_{2p})}{A_{1p}^2 A_{2p}^2}} \\ &= \sqrt{\cos^2(\phi_{1p} - \phi_{2p})} \\ &= |\cos(\phi_{1p} - \phi_{2p})|, \end{aligned}$$

and thus

$$V_p \propto |\cos(\phi_{1p} - \phi_{2p})|. \quad (4.4)$$

From (4.4), we can see that the *measured visibility*

$$V \equiv \sqrt{\frac{\mathbf{FP}}{\mathbf{IR}_1 \cdot \mathbf{IR}_2}} \quad (4.5)$$

is proportional the absolute value of the sum over all points p in $B(\xi, \eta)$ of $\cos(\phi_{1p} - \phi_{2p})$.

It follows from the discussion in (§2.2.3) that

$$V \propto |\mathbf{V}(\mathbf{D}_e)|, \quad (4.6)$$

where the proportionality constant relating V and $|\mathbf{V}(\mathbf{D}_e)|$ can be determined by calibration of the interferometer.

4.1.2 Visibility Values and Calibration

To obtain a visibility curve from ISI data, we compute the raw values of the measured visibility V , and then calibrate these values using the visibility of a source with a known brightness profile. This procedure is done in a number of steps, as follows.

1. Select the bandwidth for fringe power analysis. As was discussed above, a bandwidth of 10 Hz about the 100 Hz central frequency was used.
2. Analyze the data using the `visib` program. The fringe and IR power data are divided by `visib` into small intervals, each of which is analyzed to yield one raw data point. The length of the intervals is chosen such that fluctuations in the IR power average out to give a reliable value. For bright stars, such as α Ori, the interval is approximately 130 seconds, and for dimmer stars, such as IRC +10011 and IRC +10420, it is 260 seconds.

For each data point, `visib` determines a noise level in the fringe signal by integrating the power spectrum in a 10 Hz band around 125 Hz. The program then integrates from 95 Hz to 105 Hz to measure the fringe power, and subtracts the noise to get a **FP** value. The **IR₁** and **IR₂** signals are multiplied on a sample-by-sample basis,² and the products are averaged. The resulting value, **IR₁₂**, can be combined with **FP** to give a raw (uncalibrated) visibility value for the data point:

$$V = \sqrt{\frac{\mathbf{FP}}{\mathbf{IR}_{12}}}$$

Noise in the IR power signals is measured by comparing the levels during position switching, as described in §3.2.3. In order to reduce the effect of IR power fluctuations (§4.1.3), an averaged **IR₁₂**, including the values from the nearest 4 other data points, was used to compute visibilities from the 1997 data.

3. Adjust chopped visibility values if necessary. Stars with sufficient 11 μm flux, such as α Ori, can have large enough signals that fringe data can be taken while the choppers are running (§3.2.3). In this case, there will be a reduction of **FP** by about a factor of 4 because of the chopping. The actual amount of this reduction is determined by averaging the ratio of adjacent chopped and non-chopped fringe

²These signals are sampled at 100 Hz, while the fringe signal is sampled at 500 Hz.

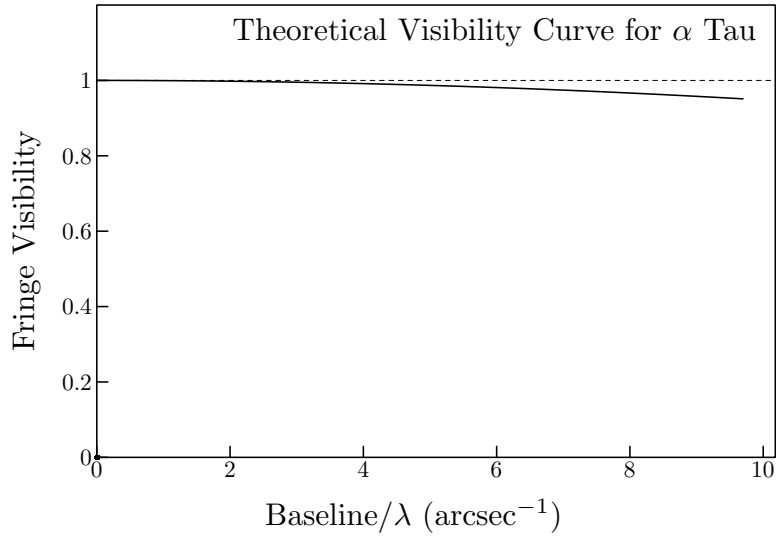


Figure 4.1: Visibility curve for a $0.0207''$ uniform disk. At the longest ISI baseline used in 1997 ($16\text{ m} = 7\text{ arcsec}^{-1}$), the calculated visibility for α Tau is 0.97.

power measurements. Chopped values are then adjusted using the average. This correction is computed on a night-by-night basis for a given source.

4. Compute correction factors to compensate for variations in instrument response. Using a test calibrator, two correlated artificial signals can be injected into the ISI detection system. The resulting visibility values indicate small variations in the response of the system due to factors such as temperature drift. Test calibration data are taken each night, and an average value for all nights on a given baseline is computed. This average is then divided by the measured values to yield a correction factor for each night. During 1997, the magnitude of these corrections averaged 1.3%, and was never more than 6%.
5. Measure the visibility of the calibrator source, and compare with the known visibility curve. The source used to calibrate ISI data during the 1997 observing season was the giant star α Tauri (Aldebaran). This star is not surrounded by a dust shell, and its angular diameter has been measured by lunar occultation and interferometry. Using a diameter of $0.0207''$, which is the average of the limb-darkened values given by Quirrenbach *et al.* [79], and assuming the star is a uniform disk, we compute the $11\text{ }\mu\text{m}$ visibility curve shown in Fig. 4.1

Fringe power for α Tau is measured in the usual way, but because of its lack of dust, the star produces little flux at $11\ \mu\text{m}$. Fluctuations in the IR power signal, caused by scattered local oscillator radiation (see §4.1.3), made it impossible to obtain a reliable \mathbf{IR}_{12} value for this source. Instead, a value is computed using the measured \mathbf{IR}_{12} for α Ori on the same night, and an $11\ \mu\text{m}$ flux ratio for the two stars which is derived using mid-infrared photometry (Monnier *et al.* [69]). The derived \mathbf{IR}_{12} value is combined with the measured \mathbf{FP} value, and the resulting visibility is adjusted using the nightly corrections from step 4.

The measured visibilities for α Tau vary enough from night to night (about 10%), that an average visibility for all the nights on a given baseline must be used. The theoretical visibility value³ is then divided by the average measured visibility on that baseline to give a calibration factor. The calibration factor only changed by about 3% during the 1997 observing season, which indicates that the instrument response is fairly stable.

6. Compute nightly calibration factors. The nightly correction from step 4 is multiplied by the calibration factor from step 5 to give an overall calibration factor for each night.
7. Correct visibility values using calibration factors from step 6. The raw visibility values are multiplied by the overall calibration factor for the night on which they were measured. The data points at this stage are shown for IRC +10011 in Fig. 4.2.
8. Eliminate or correct invalid points. An accurate visibility measurement using the ISI requires that many systems be functioning properly at the time of the measurement. A loose cable, bumped mirror, glitch in the star tracking, spider in the signal path, clouds, or any one of a number of possible malfunctions can result in incorrect visibility values. In order to assure that the final curve is accurate, some data points must be discarded. Often a logbook entry indicates the cause, such as loss of the LO phase lock, of an anomalous point. Certain other problems, such as the loss of the star in one telescope, can be deduced from a careful examination of the relative values of the IR power and fringe signals. If only

³The spatial frequency used for the calculation is an average of all those at which α Tau fringe data were gathered on that baseline.

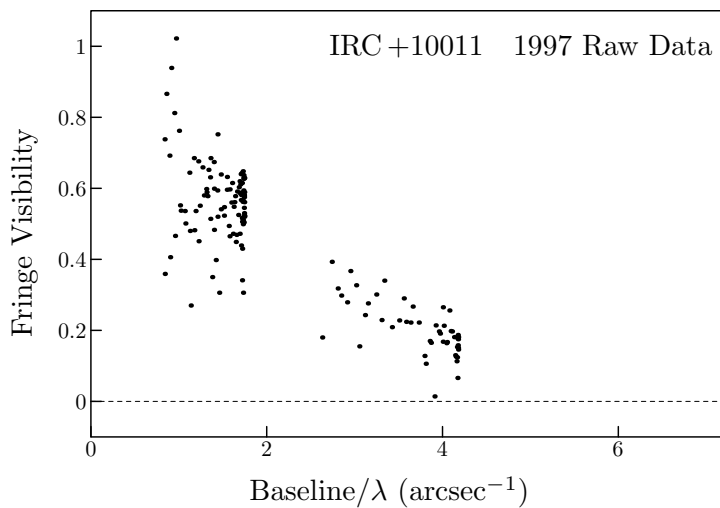


Figure 4.2: 1997 Data points for IRC +10011. Some of these points display the large errors which can be caused by various instrument malfunctions. Compare with the final points in Fig. 4.3.

a single IR power measurement is affected by a problem, it is sometimes possible to correct the data point by using an average of the IR power measurements taken immediately before and after the invalid reading.

9. Average selected points. After the elimination of invalid data points, the remaining visibility values (Fig. 4.3) are averaged in order to reduce the probable error and produce a single value for each spatial frequency. If the visibility is much larger than the probable error, the averaging is straightforward. A spatial frequency interval is chosen which is large enough to contain a number of points, but not too large to blur the finest detail in the visibility curve. The ISI beam (Fig. 3.10) is cut off a little more than $2.5''$ from the center of the field of view. Because of this, the finest oscillation in the visibility curve will have a period of about 0.4 arcsec^{-1} . Accordingly, the averaging interval is chosen to be smaller than about half this if sufficient data are available. In order to determine the probable error, a quadratic fit is done on the data for each baseline, and the RMS deviation of the data about the best-fit curve is computed. This is taken to be the population standard deviation, so the probable error for an averaged point is this quantity divided by the square root of the number of points averaged.

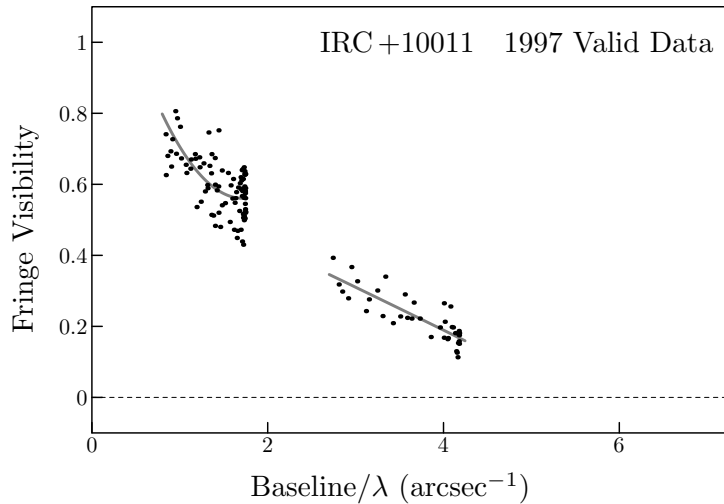


Figure 4.3: Corrected 1997 Data points for IRC +10011. These data were averaged to produce the final visibility values for the 4.0 and 9.6 m baseline measurements of IRC +10011. The probable error in the final points was computed by measuring the scatter about quadratic fits (shown above) to the data from each baseline.

If the visibilities are smaller than the probable error, there will be a number of **FP** values which are negative once the noise background is subtracted. In these cases, it is not possible to compute individual visibility values before averaging, so the **FP** and **IR₁₂** values from many points are averaged, and the visibility value is computed from these averages. This was done for the 16 m data on IRC +10011. Figure 4.4 shows the complete visibility curve measured for IRC +10011 in 1997.

4.1.3 Sources of Uncertainty

The use of heterodyne detection places a fundamental limit on the ability of the ISI to measure IR power from a star (§2.3). This limit corresponds to a star roughly 100 times dimmer than α Ori at $11\ \mu\text{m}$. The practical limit during the 1997 observing season was close to ten times the fundamental limit. This problem has made it necessary to use indirect IR power measurements for the calibration source (see the discussion in §4.1.2), which introduces a large uncertainty in the overall level of the visibility curve. It is instructive to examine some of the sources of measurement error to see what can be done to improve the situation in the future.

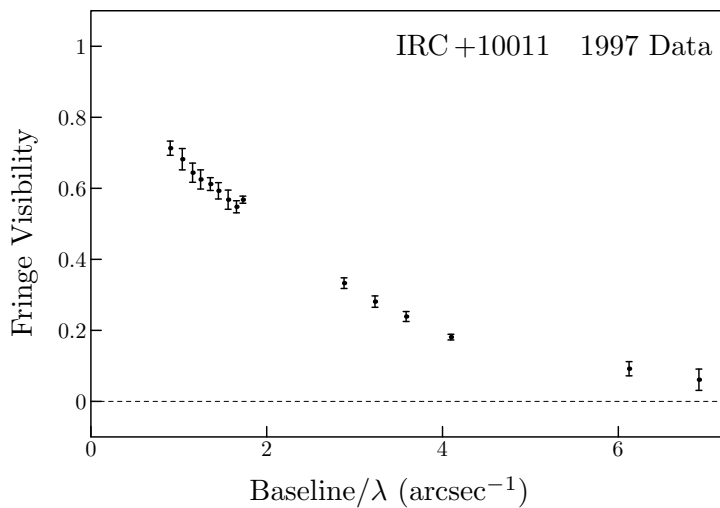


Figure 4.4: Visibility curve for IRC +10011. The points shown here for the 4.0 and 9.6 m baselines are averages of those shown in Fig. 4.3. 16.0 m baseline values result from averages taken of **FP** and **IR₁₂** over many points, some of which have negative **FP** values.

IR Power Fluctuations and Calibration

The most prominent source of error in ISI fringe visibility measurements has been a type of infrared power fluctuation which routinely amounts to 10% of the signal level produced by a bright star such as α Orionis. On occasion, the fluctuations are much larger, and totally eliminate the possibility of making a useful measurement. The fringe signal, which measures correlation between the fields in the two telescopes, is not affected by these fluctuations.

It now seems fairly certain that the cause of this problem has been scattered or back-reflected local oscillator radiation which enters the signal detector dewar. Because the power of the local oscillator exceeds that from the star by about a factor of 10^9 at the detector, even a minuscule fraction of the local oscillator signal can produce a substantial change in the measured power. During the 1998 observing season, a system which monitors slow changes in the detector current has been able to compensate for this false signal and reduce the fluctuations by about a factor of five. It is thought that another factor of two improvement may be possible by fine-tuning this system.

Unfortunately, the fluctuations affect the 1997 data in two major ways. First, they are the dominant source of the random scatter of the visibility values (Fig. 4.3).

Substantial reduction of this scatter will drastically reduce the amount of time necessary to collect a scientifically useful visibility curve for sources such as IRC+10011 and IRC+10420, which are roughly 30% and 60% as bright as α Ori at $11\ \mu\text{m}$, respectively. Secondly, accurate measurement of the IR power of the calibrator source, α Tau, which is only about 10% as bright as α Ori, was not possible with the fluctuations present. In order to obtain an \mathbf{IR}_{12} value, the IR power of α Ori was measured, and the corresponding value for α Tau was computed using photometry data taken with the United Kingdom Infrared Telescope (UKIRT) on Mauna Kea. Recent measurements of α Tau, using the fluctuation compensation system, indicate that the overall calibration of the 1997 data may be as much as 20% low. A possible explanation of this discrepancy is that the beam used in the UKIRT measurements was larger than the ISI beam. This allowed the collection of more flux from extended structure around α Ori, so the derived \mathbf{IR}_{12} value for α Tau was smaller than it should be. The measured α Tau visibility was correspondingly larger than it should be, and the calibration factors for the ISI data are consequently too small.

Atmospheric Fluctuations

Figure 3.28 demonstrates that atmospheric effects can lower the measured fringe visibility for a source. This problem is particularly severe at the shortest effective baselines, when the telescope is pointed near the horizon, and the starlight must travel a much longer path through the atmosphere. This is probably the cause of a systematic drop in visibility which was seen at short effective baselines for a number of sources in 1997. Figure 4.5 illustrates the problem for α Ori and IRC+10420.

The tip-tilt system enables the compensation of some atmospheric fluctuations, and observations of bright stars during 1997 demonstrated a significant improvement in data quality. In order to take maximum advantage of this system, however, the sensitivity of the guider cameras needs to be improved. This would allow correction during observations of stars which are dim in the near-infrared, such as IRC+10011 and IRC+10420.

Some atmospheric effects can not be corrected by the tip-tilt system. Refractive index fluctuations along the line of sight to the star will cause phase modulation of the fringe, even if they do not cause a lateral displacement of the star image. Substan-

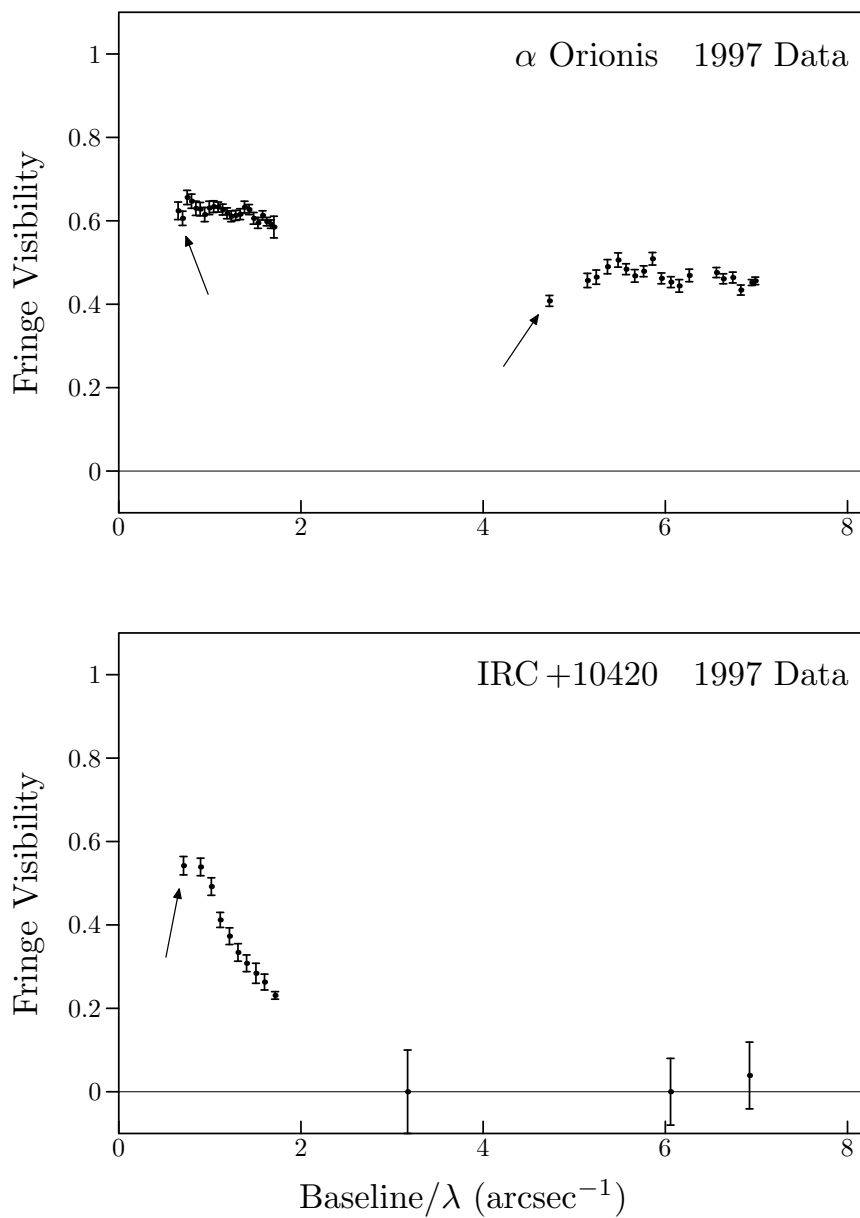


Figure 4.5: Illustration of fringe visibility drop at short effective baselines. The indicated points suggest a systematic drop in visibility, possibly caused by atmospheric fluctuations. These points were discarded before modeling of the sources was done.

tial broadening of the fringe power spectrum was seen on poor nights, even with the tip-tilt system in operation. If this broadening is too severe, fringe power will fall far from the 100 Hz center frequency, and therefore will not be detected. Under poor seeing conditions, the measured visibility typically drops, and data from such nights are often not useful. High order distortions of the star image can also not be remedied with the tip-tilt corrector. On a night when star images resemble that shown on the right-hand side of Fig. 2.7, the signal detectors will not capture all of the power in the star image, and that power which is measured fluctuates wildly. During the period when the poor image in Fig. 2.7 was acquired, infrared power fluctuations averaged about a third of the measured value for α Ori, even though the tip-tilt system was on.

A final problem caused by atmospheric conditions is that of calibration. Because of the placement of sources in the sky, it is often difficult to assure that the calibrator and the star of interest are measured under the same conditions. If there is a systematic difference, it can lead to an overall calibration error.

On the best nights at Mt. Wilson, the seeing does not contribute significantly to the error in an ISI visibility measurement. Various sensitivity improvements which increase the rate at which the instrument can acquire accurate data will allow complete visibility curves to be gathered on a few good nights, rather than many mediocre or poor ones.

Other Possible Improvements

In addition to improvement of guider camera sensitivity and elimination of IR power fluctuations, there are some other changes which could help the ISI approach the theoretical sensitivity limit. The HgCdTe infrared detectors (Bester *et al.* [6]) which are used in the ISI are constantly being improved. The signal detectors presently in the two telescopes have quantum efficiencies of about 40% and 20%. Upgrade of the lower-quality detector could result in a 3 dB gain in signal-to-noise in that telescope.

Certain systematic problems remain in the telescope hardware. On many occasions during the 1997 season, one of the telescopes would bounce in altitude by up to 3'' at rate of about 3 Hz. This problem, which was worst at low altitudes, could completely ruin the data by throwing the star on and off the detector during observations. A number of the bad points, which had to be eliminated from the data, were caused by

this problem.

Although the ISI is a very complicated instrument, with many potential sources of uncertainty, it is not unreasonable to expect that eventually it may be possible to reduce the error in fringe visibility measurements by up to a factor of 10. Such an improvement would greatly decrease the amount of time needed to obtain complete and accurate visibility curves, and would allow the measurement of dim sources which are presently inaccessible.

4.2 Modeling and Source Image Reconstruction

Once a visibility curve has been measured and reduced, a method must be chosen to recover as much of the source image as possible. The available methods can be broadly classified as using either direct inversion or modeling. Direct inversion methods use various types of mathematical interpolation to fill in missing areas of the visibility curve. The curve is then transformed to produce a brightness profile for the source. Modeling methods use physical laws, known quantities from other types of measurement, and various free parameters to construct a theoretical brightness profile. The profile is transformed, and the resulting visibility curve is compared with the data.

4.2.1 Direct Inversion

Methods for direct inversion range from relatively simple polynomial fits and cubic spline interpolation, to the somewhat more involved maximum entropy method (MEM). Polynomial fitting finds the curve of a specified order which has the minimum total RMS distance to the data points. Cubic splines are curves of the form

$$f(x) = ax^3 + bx^2 + cx + d,$$

which can be chosen to have given values and first derivatives at two specified points. Slopes are assigned to each data point (by averaging the slopes of the lines drawn between the point and its nearest neighbors, for example), and splines are used between each pair of points to draw a smooth interpolation of the visibility curve. The MEM (Skilling & Bryan [84]) finds the function which, for a set of N data points f_j , maximizes

the statistic

$$S(f) = - \sum_{j=1}^N p_j \log p_j,$$

where $p_j = f_j / \Sigma f$, while minimizing the total RMS deviation of the curve from the data. This method tends to select a curve with as little structure as possible. If there are no other constraints, the MEM will assign the same value to each point on the curve.

Direct inversion methods can be used to get a general idea of the form or characteristic size of the brightness distribution, or to suggest directions for modeling. The MEM analysis of ISI data on the source NML Cygni (Monnier *et al.* [68]), for example, suggested a two-shell model which fit the data quite well. Ultimately, however, these methods are inferior to modeling for extracting physical information from visibility data. Each of the direct methods makes use of some arbitrary mathematical assumption to complete the visibility curve. Whether such an assumption is appropriate is a matter of chance. For example, the MEM tends to deemphasize structure in a visibility curve. Since all visibility curves approach a value of 1 at zero spatial frequency, they can never match the MEM's ideal of a flat curve, and points at small spatial frequencies tend to be too low in MEM interpolations.

4.2.2 Radiative Transfer Modeling

Radiative transfer modeling provides the opportunity to incorporate ISI data into a comprehensive picture of the source which draws from other sorts of measurements, such as spectroscopy, speckle imaging, polarimetry, and radio interferometry. Conjecture about the stellar environment, based on physical law, provides a more realistic way to deal with sparse data than do the mathematical assumptions of direct inversion.

The modeling of ISI data was described extensively in a paper by Danchi *et al.* [25]. A summary of the modeling procedure, along with a discussion of selected parameters, will be presented here. The ISI radiative transfer code is adapted from one developed by Wolfire and Cassinelli [94] for studying accretion flows. The model consists of a star, taken to be an ideal blackbody at the specified temperature T_* , and a spherically symmetric dust shell, as pictured in Fig. 4.6. The dust is assumed to be composed of silicates, based on the prominent $9.7 \mu\text{m}$ feature in the mid-infrared spectra

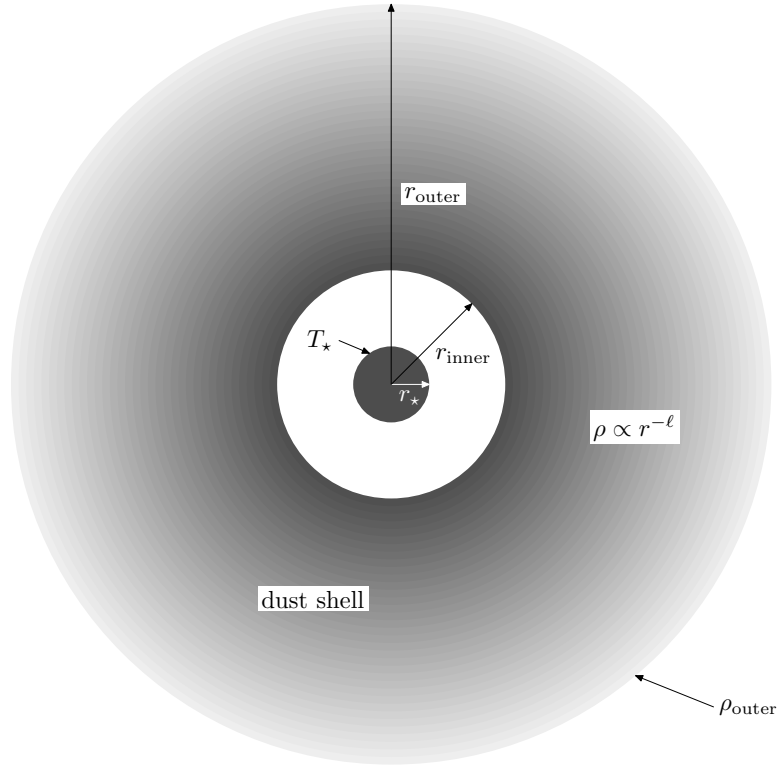


Figure 4.6: Illustration of the radiative transfer model. The star, shown at the center of the diagram, has a radius r_* , and a photospheric temperature T_* . At the inner radius r_{inner} , the temperature has dropped enough to allow the formation of dust. An arbitrary outer radius r_{outer} is chosen, and the corresponding density ρ_{outer} determines the density for the rest of the shell, which is proportional to $r^{-\ell}$.

of most of the stars observed by the ISI.⁴ Various other properties of the dust, such as the size distribution, optical characteristics, and fractional density compared with circumstellar gas, are taken from studies of the interstellar medium (Mathis *et al.* [61]) and measurements of circumstellar silicate opacities (Ossenkopf *et al.* [73] and references therein). The dust condenses at the inner radius r_{inner} , and the combined density of the gas and dust falls off according to a specified power law ($\rho \propto r^{-\ell}$). The density ρ_{outer} is specified at r_{outer} , in order to set the scale for ρ . The outer radius r_{outer} was taken to be $3''$, which is beyond the edge of the ISI beam.

Given the physical model of the star and its surroundings, the radiative transfer code computes a self-consistent radial temperature profile using an iterative procedure.

⁴The code is also capable of including graphites and two phases of amorphous carbon if appropriate.

From this profile and the optical properties of the dust shell, the code produces a mid-infrared spectrum and radial brightness profile. The brightness profile is multiplied by the telescope beam pattern (§2.2.3), and processed using a fast Hankel transform algorithm (Hansen [36]) to yield a model visibility curve, which can be compared with ISI data.

The process of finding the best model parameters is as follows. First, the distance to the star and effective temperature are chosen. The distance D sets the actual length scales in the model, since only the angular extent of the star is indicated by the data. Fortunately, the model is not very sensitive to D , as the probable errors in measurements of D are often as large or larger than stated value. The model chosen for the source IRC +10011 (see Chapter 5) was essentially unaffected by a 40% change in D . The effective temperature T_\star is selected to match the spectral type of the star. The modeling is also not very sensitive to T_\star , since r_\star can be changed to vary the total amount of flux from the source.

Once D and T_\star have been chosen, typical values are assigned to r_{inner} and ρ_{outer} , and ℓ is set to be 2, which corresponds to the density profile for a uniform outflow from the star. The stellar radius r_\star is then varied in order to match the total flux in the model spectrum with that in a measured spectrum, such as those from Monnier *et al.* [69].

At this point, r_{inner} and ρ_{outer} are varied to produce the best possible fits to the mid-infrared spectrum and the visibility curve. If satisfactory fits can not be obtained, ℓ is changed and the procedure is repeated.

Each time the model is run, two values are computed which facilitate the comparison between the model and the data. The agreement between a model and the measured visibility curve can be characterized by the parameter (Bevington [12])

$$\chi^2 \equiv \sum_{i=1}^N \frac{[y_i - f(x_i)]^2}{\sigma_i^2},$$

where y_i are the N visibility values at spatial frequencies x_i , σ_i are the probable errors in y_i , and $f(x)$ is the visibility curve generated by the model. Although χ^2 provides a convenient measure of the quality of the fit, it should not be regarded as an absolute indicator of this quality. For ISI data, χ^2 tends to emphasize the fit at short baselines, since the data are denser there.

The optical depth τ is a measure of the opacity of the dust shell. For radiation

of intensity I , traveling a distance s in an absorbing medium,

$$\frac{dI}{ds} = -\alpha I,$$

where $\alpha(s)$ is the absorption coefficient. Thus,

$$I(s) = I(s_0) \exp \left[- \int_{s_0}^s \alpha(s') ds' \right]. \quad (4.7)$$

The optical depth is defined as the integral in (4.7):

$$\tau = \int_{s_0}^s \alpha(s') ds'.$$

This parameter of the dust shell is determined primarily by ρ_{outer} and ℓ , which together specify the amount of dust between the star and the observer. There is also an effect on τ when r_{inner} is changed, since the highest density of dust is at r_{inner} . The shape of the mid-infrared spectrum is strongly influenced by the optical depth. Whether the dust shell is optically thick (opaque) with $\tau > 1$, or optically thin (transparent to some degree), will determine if spectral features, such as the $9.7 \mu\text{m}$ silicate peak, will be seen in absorption or emission, and to what extent. The constraint placed on τ by the spectral data provides a useful check of the assumption of spherical symmetry. If the visibility curve can not be fit well under conditions which match the spectrum, it may indicate that the source is actually surrounded by a disk or other more complicated dust distribution instead of a spherical shell.

Results from the modeling of ISI data taken in 1997 on the sources IRC +10011 and IRC +10420 are presented in the next chapter.

Chapter 5

IRC +10011 and IRC +10420

Completion of the ISI near-infrared guiding system enabled observations of a number sources which had been inaccessible in the past. Efforts during the 1997 observing season were concentrated on two sources, IRC +10011 (also known as CIT 3) and IRC +10420.¹ Properties of these two objects are shown in Table 5.1.

Visibility data were collected on a total of 21 nights for IRC +10011, and 18 nights for IRC +10420, between 12 August 1997 and 10 December 1997. Three baselines were used, 4.0 m until 5 October, 16.0 m until 6 November, and 9.6 m for the rest of the season. Table 5.2 shows the position angles of the effective baselines for the

¹In these identifiers, “IRC” stands for the Caltech Infrared Catalog (Neugebauer *et al.* [72]). The sign and first two digits of the number indicate the range of declination in which the source lies. For example, both IRC +10011 and IRC +10420 lie between +5 and +15 degrees declination, so their identifiers begin with “IRC +10.” The last three digits identify the source by number, in increasing order of right ascension within the declination band.

Table 5.1: Properties of IRC +10011 and IRC +10420. The spectral type of IRC +10420 has changed over the past 20 years. 1 Jansky (Jy) = $10^{-26} \frac{\text{W}}{\text{m}^2 \cdot \text{Hz}}$.

Property	IRC +10011	IRC +10420	Reference
Right Ascension (2000.0)	1h 6m 25.92s	19h 26m 48.00s	[20]
Declination (2000.0)	+12° 35' 53.2"	+11° 21' 16.6"	[20]
Visible Magnitude	9 @ 1 μm	8.5	[32],[20]
K band Magnitude	2.0	3.4	[32]
11 μm Flux Density	1200 Jy	2500 Jy	[32]
Spectral Type	M9	F8–A5	[20], [49]
Effective Temperature	2700 K	7000 K	[77], [75]
Distance	500 pc	5000 pc	[16], [43]

Table 5.2: Position angles for measurements of IRC +10011 and IRC +10420. If one takes the baseline vector \mathbf{D} , and projects it onto a plane perpendicular to the vector which points at the star, the projected vector \mathbf{D}_e will point at an angle ϕ_p from north. The position angle ϕ_p , tabulated below, is defined such that due east corresponds to $\phi_p = 90$ degrees.

Baseline (m)	Position Angle (degrees)	
	IRC +10011	IRC +10420
4.0	260–297	240–274
9.6	296–307	297–303
16.0	303–315	303–308

measurements. Although spherical symmetry was assumed for all modeling purposes, the position angles are needed when making comparisons with measurements that have 2-dimensional coverage.

5.1 IRC +10011

5.1.1 Background

IRC +10011 is an oxygen-rich long-period variable star of spectral type M9. It has a K band magnitude of 2.0 and a flux density at $11\ \mu\text{m}$ of $1200\ \text{Jy}$,² making it an ideal candidate for study by the ISI. This source exhibits maser emission on both SiO (Cho *et al.* [21]) and OH lines. Outward flow of material from the star causes the OH maser emission to have a double-peaked spectrum, with a red-shifted component due to the receding material on the far side, and a blue-shifted component from the approaching material on the near side. As the luminosity of the star varies, the masers on either side of the star will vary synchronously in intensity. As seen from Earth, however, the intensity variations in the red-shifted and blue-shifted components will be out of phase because of the extra time required for light to travel from the far side of the star. By measuring this phase lag, Jewell *et al.* [40] determined the linear diameter of the OH emission region around IRC +10011 to be $(6.6 \pm 1.4) \times 10^{16}\ \text{cm}$.

Using the linear OH shell diameter in combination with their angular diameter data from the Very Large Array radio interferometer, Bowers *et al.* [16] found a distance

²1 Jansky (Jy) = $10^{-26}\ \frac{\text{W}}{\text{m}^2\cdot\text{Hz}}$. By comparison, the flux from α Orionis is approximately 4300 Jy at $11\ \mu\text{m}$.

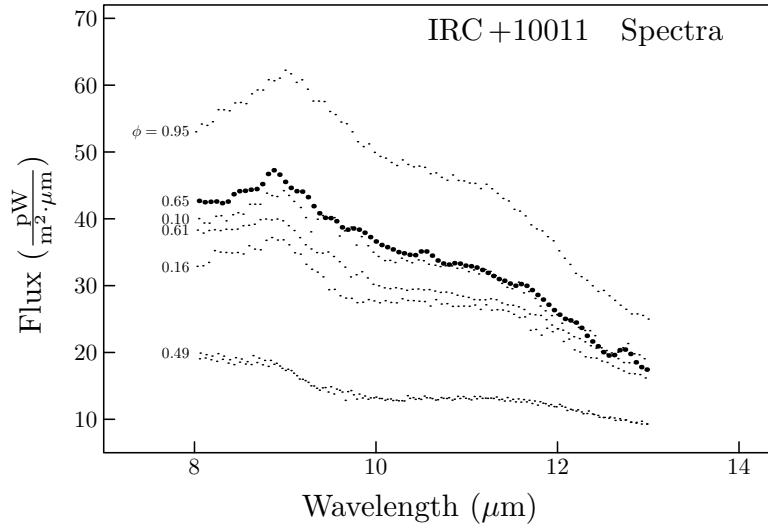


Figure 5.1: IRC +10011 mid-infrared spectra. These measurements, taken from Monnier *et al.* [69], illustrate the variability of IRC +10011. At left is indicated the luminosity phase, in cycles, of each spectrum, with maximum luminosity corresponding to a phase $\phi = 1$. The highlighted spectrum was used for the modeling of IRC +10011, since its phase is close to the average phase (0.67) during the period of ISI observations. The flux calibration of each spectrum has a stated uncertainty between 5 and 10%, though excellent agreement can be seen between the two spectra at $\phi = 0.49$, taken 660 days apart.

of 500 pc to IRC +10011. This distance was adopted for the modeling of ISI data. Although the stated uncertainty in the measurement was a factor of two, it agrees with other estimates, such as that from a period-luminosity relation (650 pc, as given by LeBertre & Winters [56]). CO line emission observations (Knapp & Morris [50]) have also been done on this source, yielding an outflow velocity of $23.0 \pm 0.9 \text{ km}\cdot\text{s}^{-1}$ for circumstellar material. Based on the work of Perrin *et al.* [77] and the spectral type M9, the effective temperature for modeling of IRC +10011 was taken to be 2700 K.

The variation in luminosity of IRC +10011 can be seen in its mid-infrared spectra, taken at various times over a 3 year period (Fig. 5.1). The luminosity cycle has a period of 660 days (LeBertre [55]). ISI measurements during 1997 spanned a range of phases between 0.59 and 0.76 cycles, where the maximum luminosity occurs at a phase of 1 (or 0). In addition to the substantial change in overall mid-infrared flux during a cycle, there is also a noticeable variation in the shape of the silicate feature just below $10 \mu\text{m}$. This feature is seen in absorption, indicating an optical depth greater

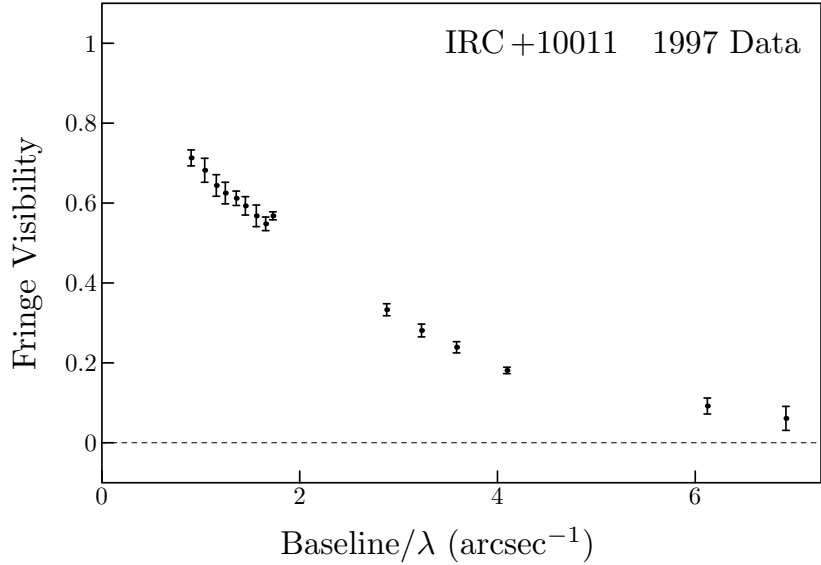


Figure 5.2: IRC +10011 1997 visibility data.

than 1 (compare with the spectrum of IRC +10420 in Fig. 5.7, which shows the feature in emission). The characteristics of these spectra are discussed in detail in a paper by Monnier *et al.* [69]. Within a few years, enough ISI data should be available to see how the visibility curve for this source changes with the star's luminosity.

A measurement of the diameter of IRC +10011 at three infrared wavelengths was done in the early 1970s by Zappala *et al.* [95] using lunar occultation. The results were modeled with a combination of two uniform disks. The best-fit model at $10\ \mu\text{m}$ consisted of an outer disk with angular radius $0.068''$ producing 85% of the observed flux, and an inner disk of radius $0.033''$ contributing the remaining 15%. They also concluded that not more than 15% of the flux originated from a region more than $0.2''$ from the center of the source. The fraction of power contained in extended dust emission led the authors of this study to suggest that the optical depth of the shell at $10\ \mu\text{m}$ was between 1 and 3.

5.1.2 ISI Results and Models

1997 fringe visibility data for IRC +10011 are shown in Fig. 5.2 and Table 5.3. Some measurements of this source were also taken at the end of the 1996 season on the 4 m

Table 5.3: 1997 visibility values for IRC +10011.

Baseline/ λ (arcsec $^{-1}$)	Fringe Visibility
0.90	0.713 ± 0.020
1.04	0.682 ± 0.030
1.16	0.644 ± 0.027
1.25	0.625 ± 0.027
1.36	0.612 ± 0.018
1.45	0.593 ± 0.023
1.56	0.568 ± 0.027
1.66	0.548 ± 0.017
1.73	0.568 ± 0.010
2.88	0.333 ± 0.015
3.23	0.281 ± 0.016
3.59	0.239 ± 0.014
4.10	0.181 ± 0.008
6.12	0.092 ± 0.020
6.92	0.061 ± 0.030

baseline. Although the quality of the 1996 data was extremely poor (probable error in the fringe visibility was approximately 0.25) because the new guiding system had not yet been optimized, the results were consistent with the 1997 values. The visibility curve shows a gradual but steady drop out to the longest measured baseline. This drop indicates the presence of a dust shell with an extent on the order of $0.1''$.

The best-fit spherical-shell radiative transfer model for IRC +10011 is shown in Fig. 5.3, and Fig. 5.4 is a reconstructed image, based on the radial profile from the model. Superposed on the image is a circle, indicating the diameter of the first null of the $11\ \mu\text{m}$ Airy pattern for a 10 m telescope. This model has a central star with angular radius $r_\star = 0.0036''$, which, at $D = 500\ \text{pc}$, corresponds to a linear distance of about 390 solar radii. This is large, but reasonable for an asymptotic giant. The inner radius of the dust shell is $0.033''$, or about $9r_\star$. A 10% increase in r_{inner} for this model results in a 3% increase in χ^2 , and a 5% drop in the optical depth. A 10% increase in ρ_{outer} produces a 44% increase in χ^2 , and a 10% increase in τ .

A good match to the curve implied by the visibility data could only be obtained using a dust shell density, proportional to $r^{-1.5}$, which falls off slower than the r^{-2} expected of the shell around a star with constant, uniform dust outflow. The best uniform outflow model is shown in Fig. 5.5. This model produced a much higher optical

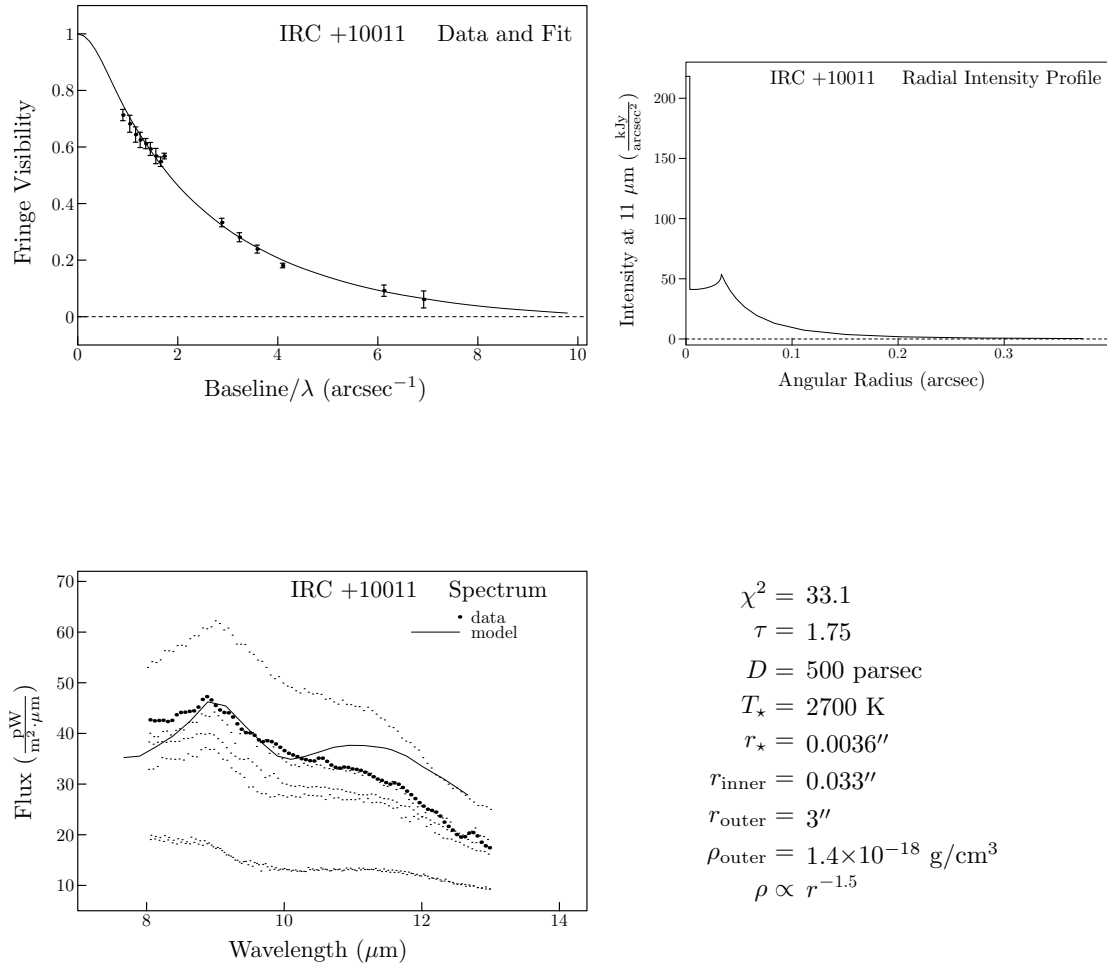


Figure 5.3: IRC +10011 best-fit model.

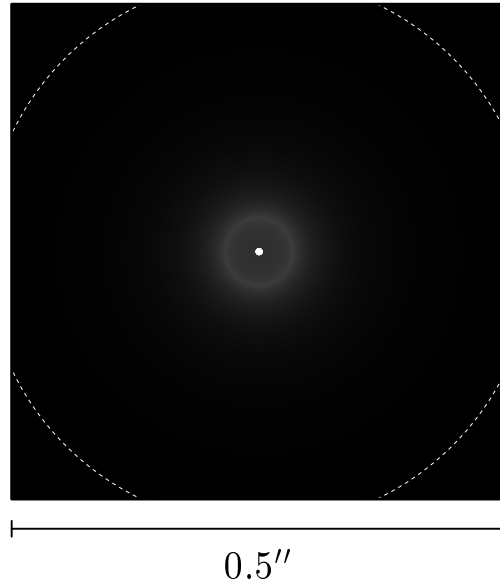


Figure 5.4: IRC +10011 $11 \mu\text{m}$ model image. The star can be seen at the center of the image, surrounded by its dust shell. Indicated with a dashed line is the $11 \mu\text{m}$ Airy disk diameter for a 10 m telescope.

depth ($\tau = 2.95$ as opposed to $\tau = 1.75$ in the best-fit model), and consequently the fit to the spectrum was considerably worse.

The model spectrum for IRC +10011 does not match the data at wavelengths beyond $10 \mu\text{m}$. An alternative model which fits the spectrum in this region is shown in Fig. 5.6. This model required a lower dust density, and the resulting optical depth produced a spectrum with a poor match to the shape of the silicate feature. In addition, the visibility curve in the alternative model is too high. Even when a possible calibration error of 10% (§4.1.3) is taken into account, as illustrated by diamonds above the visibility points in the figure, the model is clearly unacceptable.

A number of factors could be responsible for the poor fit of the spectrum from the best model (Fig. 5.3) at wavelengths beyond $10 \mu\text{m}$. First, data on IRC +10011 were taken over a range of luminosity phases between $\phi = 0.59$ and $\phi = 0.76$. Figure 5.1 clearly shows that the shape of the spectrum changes with luminosity phase. The spectrum chosen for comparison with the model is simply that at an average phase, and does not take into account the amounts of data taken at any particular phase, nor whether various parts of the spectrum change at different rates. Secondly, Monnier

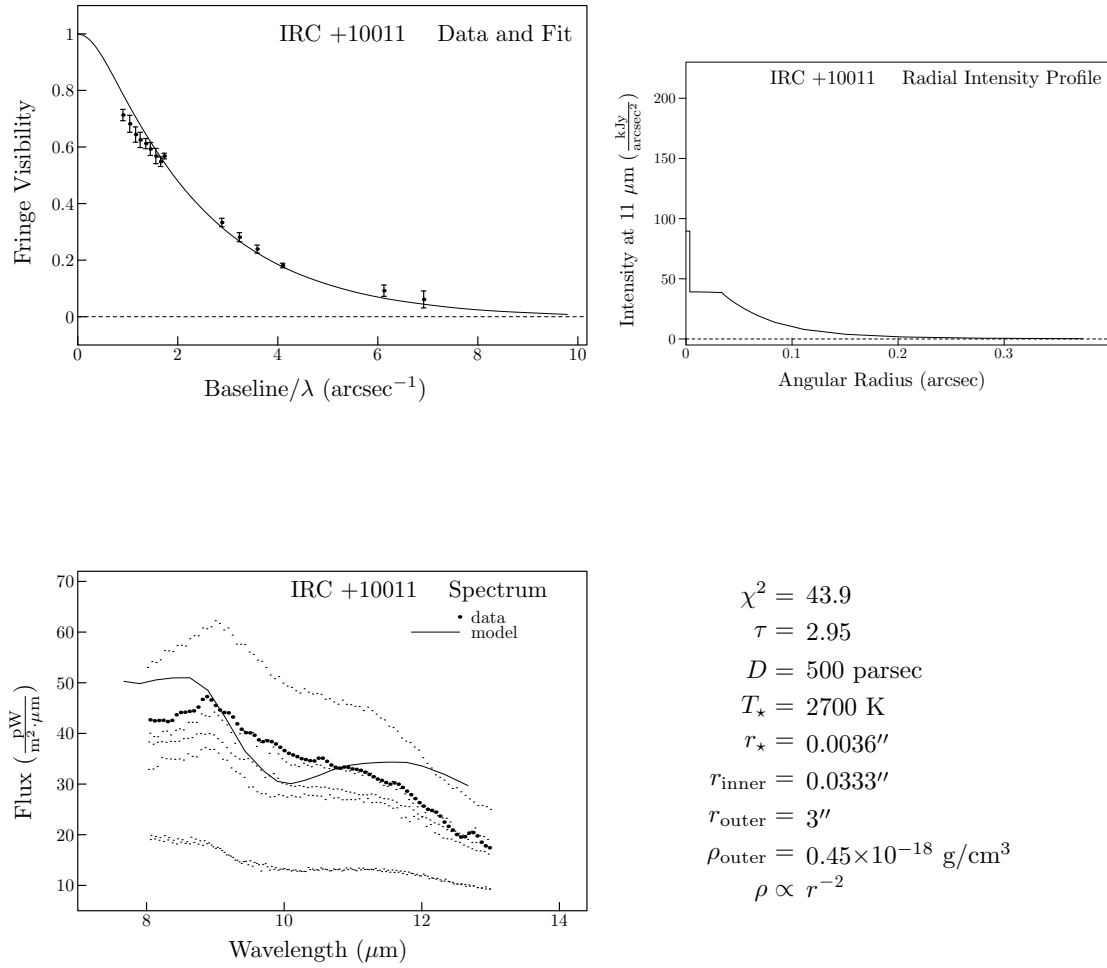


Figure 5.5: IRC +10011 best uniform outflow model.

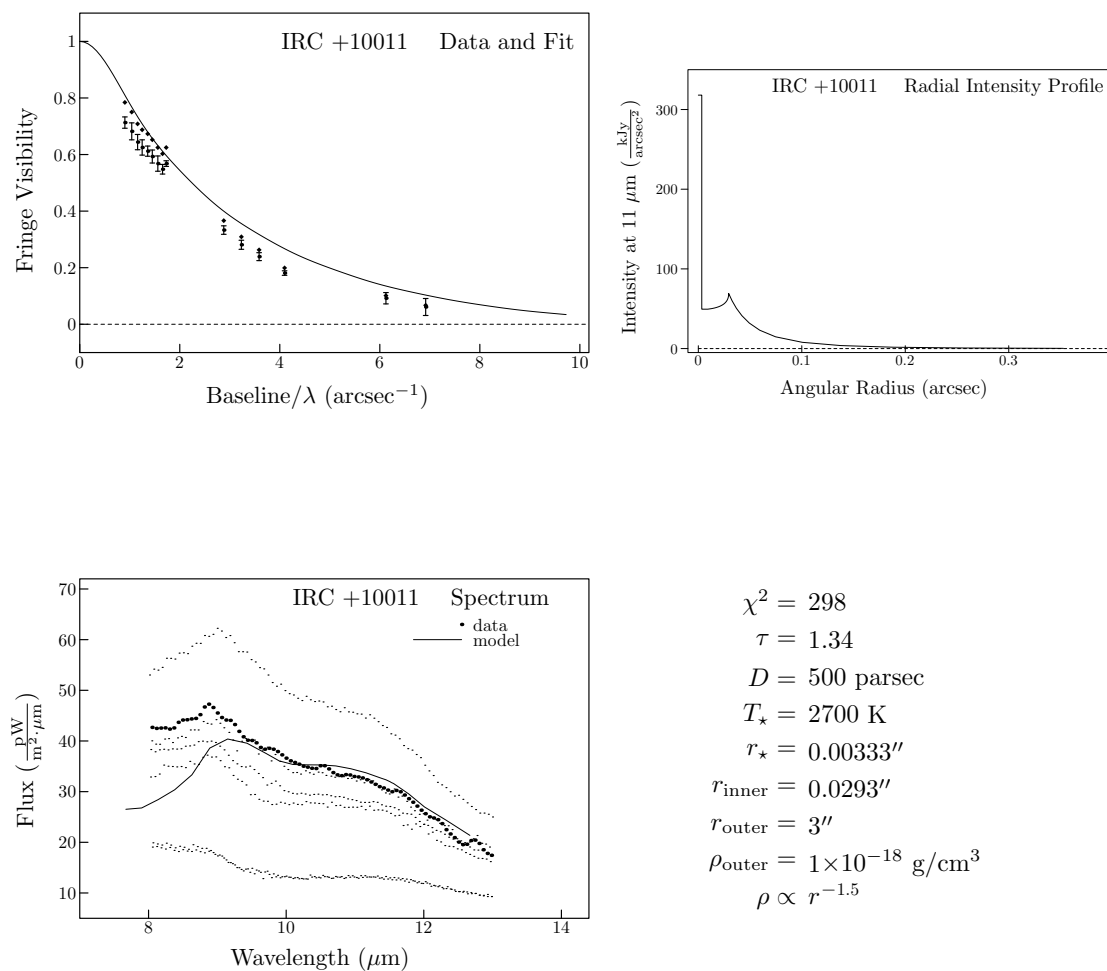


Figure 5.6: Model fit to tail of mid-infrared spectrum for IRC +10011. Small diamonds are drawn at points 10% higher in visibility than the data points in order to illustrate the effect of a possible miscalibration.

et al. [69] suggest that dust properties may change during the luminosity cycle. Such a change would not be accounted for in the ISI radiative transfer model, which assumes constant optical properties and location of formation (r_{inner}) for the dust grains. Finally, the assumption of spherical symmetry may be naive. If the dust is actually in the form of a disk, for example, then the observed radiation could be a combination of direct light, which has traveled through relatively little dust, and scattered light from the disk. Thus the resulting spectrum could exhibit features of shells with different optical depths.

5.1.3 Discussion of Results

The model fit to ISI data on IRC +10011 produces a picture of the star and its surroundings which is certainly reasonable, and in good agreement with the other available observations. The inner dust shell radius of $0.033''$ corresponds to that of the inner disk chosen by Zappala *et al.* to model their lunar occultation data. Recent near-infrared results from aperture masking at the Keck telescope (Monnier [67]) indicate an inner radius within 5% of the value from the ISI model. As was pointed out by Ivezić & Elitzur [39], the inner radius should not be wavelength dependent. The aperture masking results also find no ellipticity or other substantial deviations from axial symmetry in the near-infrared image of the source. This lends credence to the assumption of spherical symmetry, although it is still possible that the dust shell is actually a disk, seen pole-on from the Earth.

The model optical depth $\tau = 1.75$ yields a good fit to the silicate feature of the spectrum at a phase which matches the average during ISI observations. It is consistent with the prediction of Zappala *et al.* that the $10\ \mu\text{m}$ optical depth should lie between 1 and 3. Monnier *et al.* [69] also predict that τ for IRC +10011 should be “only slightly smaller than that of NML Cyg,” which has an optical depth of about 2.

A number of radiative transfer models have been done for IRC +10011 (Justtanont *et al.* [45], Le Sidaner & Le Bertre [57]). By assuming uniform, spherically symmetric mass outflow, and using a mass loss rate inferred from infrared spectra, Justtanont *et al.* derived a radial temperature profile for the source. Although the general shape of the profile approximates that resulting from the ISI model, the overall level of the ISI profile is substantially higher, due to the fact that Justtanont *et al.* adopted an

effective temperature of 2000 K for IRC +10011. Their infrared modeling (Justtanont & Tielens [46]) did, however, produce values for r_* and r_{inner} within 50% of those in the ISI model, which is not unreasonably far off, considering the assumptions used in the modeling, such as a somewhat arbitrary luminosity of $10^4 L_{\odot}$, and uniform dust outflow. The lack of measured parameters in these models frustrates attempts at meaningful quantitative comparison with ISI data.

The mass density $\rho \propto r^{-1.5}$ implies that there is more dust farther from the star than would be expected from a uniform dust outflow. This has been the case in other ISI models, such as those for IRC +10216 (Danchi *et al.* [25]). Two possible explanations for the slow drop in density are time-varying dust emission and deviation from spherical symmetry. If dust was produced at a greater rate in the recent past, there will be a region of relatively high density moving away from the star. Circumstellar dust in some form other than a spherical shell, for example a disk or some sort of lobe structure, could also cause the model density to mimic a time-varying outflow. Future interferometric measurements at a variety of wavelengths should shed more light on the form of the material around this and other evolved stars.

5.2 IRC +10420

5.2.1 Background

IRC +10420 is a luminous supergiant which has been extensively studied over the past 25 years. Like IRC +10011, it is oxygen-rich, however the two objects differ in a number of respects. As is illustrated by its mid-infrared spectra (Fig. 5.7), IRC +10420 does not exhibit periodic luminosity variations. In addition, it has a much earlier spectral type than IRC +10011. The initial measurement, which was done in 1973 by Humphreys *et al.* [37], yielded a spectral type of F8Ia. Recent observations by Oudmaijer [74] indicate that the spectral type is now much earlier, and that the effective temperature of IRC +10420 increased by 1000–2000 K between 1973 and 1994. Klochkova *et al.* [49] find a spectral type of A5 based on recent spectral data. Dramatic changes in the OH maser emission over the same time period have been reported by Nedoluha & Bowers [71].

IRC +10420 is often characterized as “peculiar” (Diamond *et al.* [26], Oudmaijer *et al.* [75]). This source is indeed unusual in that it is the only known OH maser

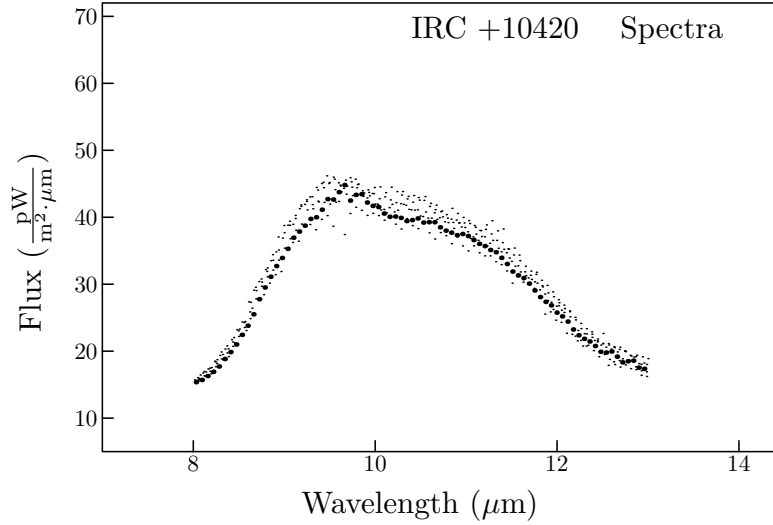


Figure 5.7: IRC +10420 mid-infrared spectra from Monnier *et al.* [69]. The stated uncertainties in the flux calibrations for these spectra were between 5 and 15%. The highlighted spectrum was taken on 28 August 1997, closest to the time of the ISI observations, and was used in modeling the source.

source with spectral type earlier than K (Lewis *et al.* [58]), and its maser spectrum does not exhibit the common double-peaked velocity signature at 1612 MHz from stellar outflow (Bowers [15]). In addition, the $9.7\ \mu\text{m}$ silicate feature (Fig. 5.7) is seen in emission in the spectrum of IRC +10420. OH maser sources are frequently surrounded by optically thick dust shells, and show this feature in absorption.

Maser emission from this star has been studied by a number of authors. Based on his analysis of 1612 and 1667 MHz data, Bowers [15] concluded that there has been “extensive mass loss” within about the last 500 years, and that the distribution of material around the star is in a “clumpy” sphere. Diamond *et al.* [26] found that their 1612 MHz observations, taken at roughly the same time, could best be explained with a bipolar outflow model. Later results by Nedoluha & Bowers [71] still indicated evidence for clumps of emitting material, despite changes in maser intensity and angular distribution. They modeled the region of emission as an oblate spheroid.

In 1993, Jones *et al.* [43] presented a review of a number of different observations of IRC +10420, including optical and infrared spectra, imaging, photometry, and polarimetric data. In their paper, a strong case is made for a distance of between 4000 and 6000 pc to IRC +10420, based on interstellar reddening and polarization, in

addition to observations of sodium D lines in the spectrum. These lines are blue-shifted with respect to the stellar spectrum, and therefore thought to originate in the interstellar medium. Furthermore, this distance estimate is consistent with the kinematic distance based on galactic rotation, and results in an intrinsic luminosity of $5 \times 10^5 L_{\odot}$, which is normal for such a supergiant. For ISI modeling, a distance of 5000 pc was chosen, along with an effective temperature of 7000 K based on the work of Oudmaijer *et al.* [75]. Jones *et al.* combined their results in a model which consists of a central star surrounded by an equatorial disk which is tilted with respect to our line of sight. Recent imaging work by this group (Humphreys *et al.* [38]), using the Hubble Space Telescope and a 3.6 m ground-based infrared telescope, shows complex structure surrounding the star, including jets, arcs, and condensations. Their infrared images display bipolar emission along a northeast-southwest axis in a $4 \times 4''$ field of view.

Other imaging work has been done on IRC +10420. Early near-infrared speckle interferometry by Dyck *et al.* [27] indicated the presence of a dust shell which has approximately the same size along north-south and east-west baselines at a given wavelength (FWHM of a Gaussian fit to the shell was $0.072''$ at $2.2 \mu\text{m}$, and $0.154''$ at $4.8 \mu\text{m}$). Ridgway *et al.* [80] modeled near-infrared speckle measurements and found an inner radius of $0.125 \pm 0.015''$ for a spherical dust shell. In 1987, Cobb & Fix [24] published visibility curves from $10 \mu\text{m}$ speckle interferometry on IRC +10420, and concluded that in the north-south and east-west directions, the source is symmetric to within their experimental errors. Direct imaging has been done by Bloemhof *et al.* [13] using a scanned linear array of $10 \mu\text{m}$ detectors and a 3 m telescope. They found a FWHM of $0.36''$ for a Gaussian fit to the dust shell. Polarimetric imaging in the near-infrared by Kastner & Weintraub [47] revealed roughly circularly symmetric emission out to $9''$.

5.2.2 ISI Results and Models

The measured visibility curve for IRC +10420 is shown in Fig. 5.8 and Table 5.4. These points were generated from ISI data taken on three baselines during 1997. Raw data from the shortest baseline, 4.0 m, are shown in Fig. 5.9. Fringe power and IR power values taken on the longer baselines (9.6 m and 16.0 m) had to be averaged separately before the fringe visibility could be computed, since after subtraction of the background noise, many of the fringe power values were negative. The visibility curve

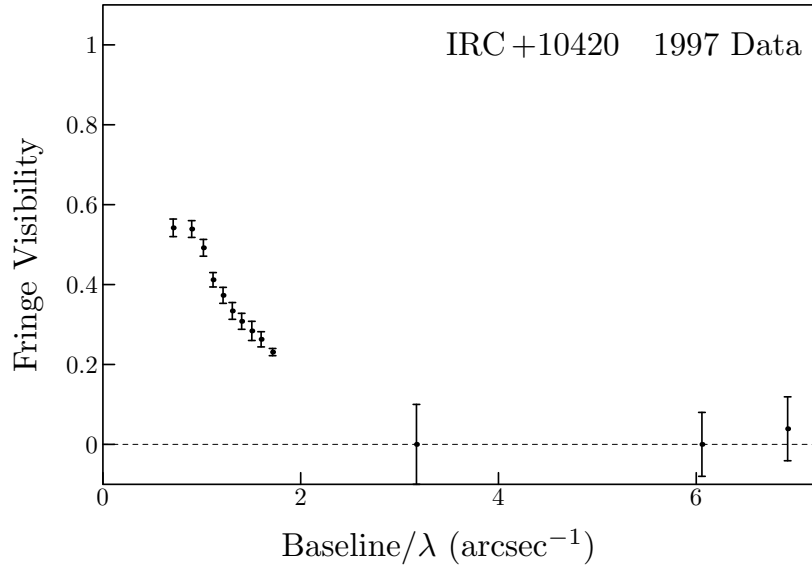


Figure 5.8: IRC +10420 1997 visibility data.

Table 5.4: 1997 visibility values for IRC +10420.

Baseline/λ (arcsec ⁻¹)	Fringe Visibility
0.71	0.542 ± 0.022
0.90	0.539 ± 0.021
1.02	0.492 ± 0.021
1.11	0.412 ± 0.018
1.21	0.373 ± 0.020
1.31	0.334 ± 0.021
1.40	0.308 ± 0.020
1.51	0.284 ± 0.024
1.60	0.263 ± 0.019
1.72	0.231 ± 0.009
3.17	0.000 ± 0.100
6.06	0.000 ± 0.080
6.92	0.039 ± 0.080

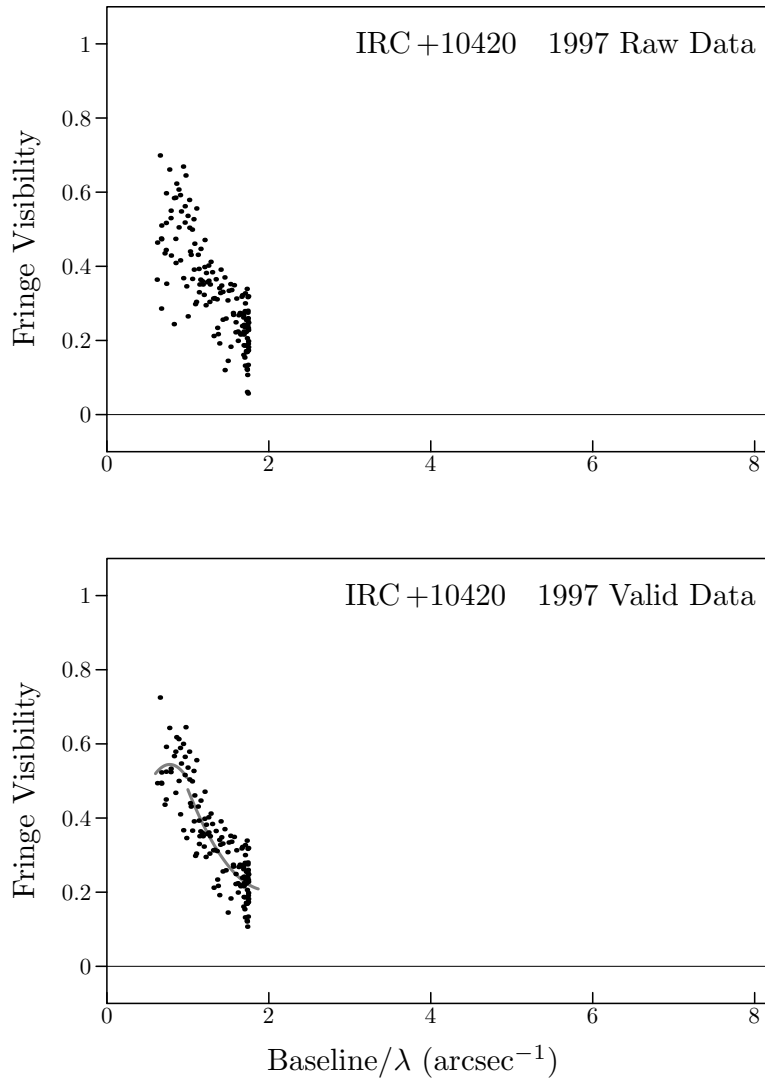


Figure 5.9: Raw and valid data points for IRC +10420. The curves shown in the bottom plot were used to determine the probable errors in the final visibility curve. Points with spatial frequency less than 0.97 arcsec^{-1} were analyzed separately. 9.6 and 16.0 m baseline data (not shown) contained negative fringe power values, and were averaged without first computing individual visibility values.

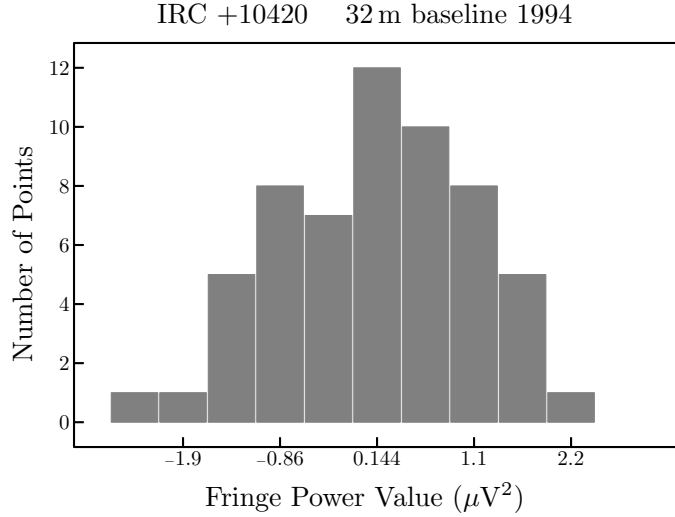


Figure 5.10: Histogram of 32 m baseline background-subtracted fringe power measurements on IRC+10420. The plot is centered about the mean of the distribution, $0.144 \mu V^2$, which corresponds to a fringe visibility of about 0.1. The width of each bin is half the standard deviation of the distribution. This measurement is consistent with a fringe visibility of zero.

for IRC+10420 can be seen to drop off very rapidly, and by the time the spatial frequency reaches 3 arcsec^{-1} , there is little or no power left to be resolved. This indicates that the mid-infrared emission comes from an extended region around the star, and that the fraction of power received from the central point, which corresponds to the star itself, is insignificant.

A small amount of data was acquired on IRC+10420 during the 1994 observing season by guiding the telescopes manually. At the time, the interferometer was at its maximum available baseline of 32 m. A histogram of the measured fringe powers is shown in Fig. 5.10. It can be seen that the fringe visibility at this long baseline, if not zero, is very small. The average \mathbf{IR}_{12} was approximately $11 \mu V^2$ for this measurement, and the visibility resulting from a fringe power of $0.144 \mu V^2$ would be about 0.1.

The point at the shortest effective baseline, 0.71 arcsec^{-1} , was not used during the modeling of IRC+10420. In addition to the systematic drop seen at the shortest effective baselines (§4.1.3), there is uncertainty in this value due to the fact that at 0.71 arcsec^{-1} , which corresponds to 1.6 m, one telescope is in the field of view of the other. This overlap could adversely affect the accuracy of the IR power measurement.

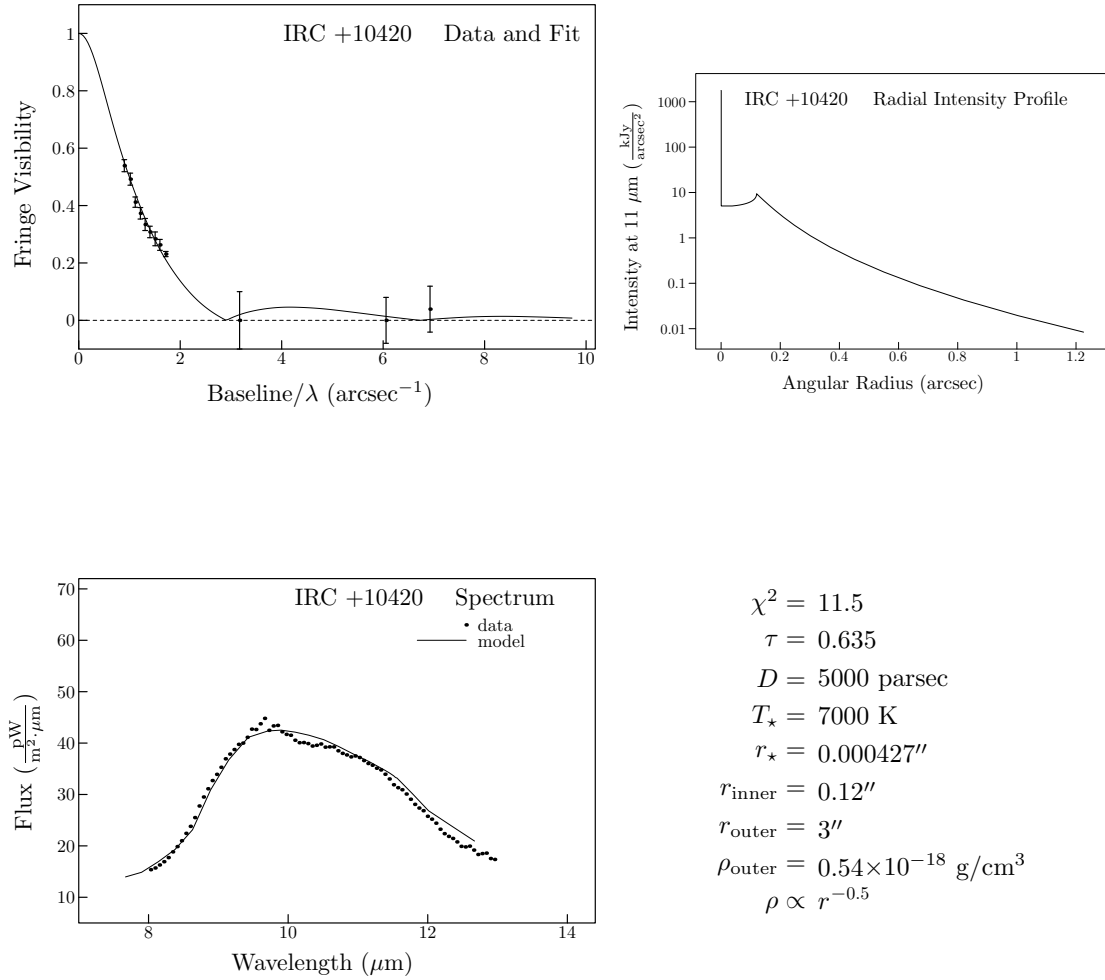


Figure 5.11: IRC +10420 best-fit model. Note the logarithmic scale used for the intensity profile (compare with Fig. 5.3).

The best-fit model for IRC +10420 is shown in Fig. 5.11. Even though the central star is extremely bright compared to the dust shell, far more power is delivered by the shell because of its vastness. The stellar radius $r_\star = 0.000427''$, which corresponds to 460 solar radii. The dust shell inner radius is much larger than for IRC +10011, at $280 r_\star$. Because of the high temperature of IRC +10420, the region where it is cool enough for dust to condense lies far from the photosphere. For this model, an increase of 10% in r_{inner} results in a 230% increase in χ^2 , and a 1% decrease in τ . An increase of 10% in ρ_{outer} produces a 30% increase in χ^2 , and a 10% increase in τ .

Although the best-fit model for IRC +10420 matched very well with the fringe

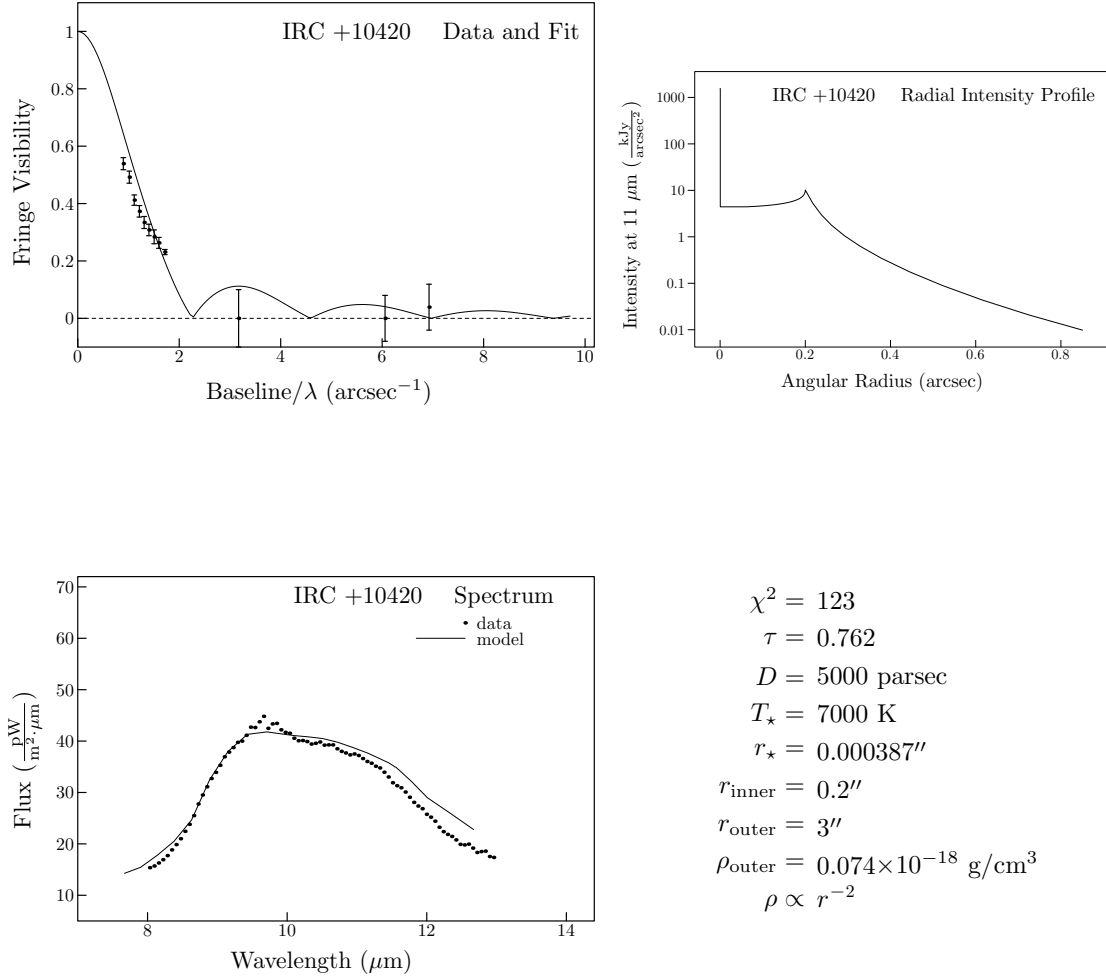


Figure 5.12: IRC +10420 best uniform outflow model.

visibility and spectral data, it was necessary to use a radial density profile proportional to $r^{-0.5}$, which is substantially different from that resulting from uniform dust outflow. Figure 5.12 shows the best model that was possible assuming uniform outflow. It is clearly inferior. Thus we can infer that either the assumption of spherical symmetry is incorrect, or else the production of circumstellar dust has decreased over time.

5.2.3 Discussion of Results

The ISI visibility curve for IRC +10420 can be compared at the shortest baselines with the mid-infrared speckle data of Cobb & Fix [24]. At a spatial frequency of 0.9 arcsec^{-1} ,

the ISI fringe visibility is 15% lower than that measured by Cobb & Fix. This could indicate miscalibration of the ISI data, as discussed in §4.1.3, although there is also a possibility that the value from the speckle data is too high, since that measurement seemed to have a systematic problem which resulted in rapidly rising visibility values past 1 arcsec⁻¹.

The ISI radiative transfer model seems to compare well with other available measurements. The overall size of the radial profile in Fig. 5.11 matches fairly well with the size of the Gaussian model given by Bloemhof *et al.* [13], and the inner radius $r_{\text{inner}} = 0.12''$, which should not be wavelength dependent (Ivezić & Elitzur [39]), matches almost perfectly with that derived by Ridgway *et al.* [80]. The optical depth $\tau = 0.635$ provides an excellent fit to the mid-infrared spectrum, with the silicate feature in emission.

The fact that the dust shell density in the IRC +10420 radiative transfer model is radically different from that produced by uniform outflow certainly deserves consideration. The model power law $\rho \propto r^{-0.5}$ requires that there be a large amount of dust far from the inner radius. Humphreys *et al.* [38] point out that the silicate feature and large fraction of extended emission in the mid-infrared argue against a uniform outflow. Mutel *et al.* [70] suggested that the dust shell surrounding IRC +10420 might be a remnant from an earlier stage in the star's evolution. Based on a spectroscopically measured outflow velocity, Bloemhof *et al.* estimated that the dust emission occurred on the order of 100 years ago. Nedoluha & Bowers [71] interpret their data as possibly supporting the hypothesis of a large emission during a previous epoch, and Humphreys *et al.* conclude, using an outflow velocity derived from measurements of CO lines, that the dust within 1'' of the star was ejected within the last 600 years. A relatively recent dust emission event thus seems to be a likely explanation for the density profile in the ISI model.

The explanation of the model density profile must also take into consideration the assumption of spherical symmetry. Although a number of the measurements mentioned in §5.2.1 suggested that the source is fairly close to being axially symmetric, images collected by Humphreys *et al.* show much complex structure, as well as bipolar mid-infrared emission oriented in such a fashion that north-south and east-west baselines could measure the same dust shell size, even though the shell is not circular. If the dust around IRC +10420 is in the form of a disk, a bipolar outflow, or clumps, this could certainly affect the model parameters. Future ISI observations with two dimen-

sional coverage should eliminate this ambiguity and provide a complete picture of the circumstellar environment.

Chapter 6

Future Directions

6.1 Improvements to the ISI

Unlike many astronomical telescopes which function as “facility instruments,” the ISI has always been, and continues to be, a work in progress. The improved guiding system is only one of a number of upgrades performed in the recent past. A filter bank has been installed in order to measure visibility curves at different wavelengths, and new detectors with higher quantum efficiency have doubled the fraction of the $11\ \mu\text{m}$ signal detected, so that it is now about 40%. At the beginning of the 1998 observing season, a circuit was installed to compensate for fluctuations, due to scattered local oscillator radiation, in the infrared power signal. These fluctuations have been the dominant source of error in visibility measurements of weaker sources, and initial results indicate that a reduction of the fluctuations by at least a factor of 10 should be possible.

Many improvements to the interferometer are anticipated in the near future. The Amber camera preamplifier was not designed for low background applications (§3.4.2), and replacement of this component could potentially increase the sensitivity of the guiding system by a few stellar magnitudes. This would allow the observation of a number of new sources, and would enable the use of tip-tilt correction on dimmer sources such as IRC +10011 and IRC +10420.

Two projects are under way which will significantly enhance the capabilities of the ISI. The site at Mt. Wilson is being prepared for a baseline roughly twice as long as the longest one (32 m) presently available. In addition, a third telescope is being built. With three telescopes, the array will have three baselines, one between

each pair of telescopes. Various arrangements of the telescopes will allow measurement of the source brightness distribution in two dimensions. If three baselines of differing length are used, it will be possible to map out large portions of a source's visibility curve without any change in telescope configuration. The third element will also make it possible to compute a quantity known as the *closure phase* (Thompson *et al.* [89]), which is independent of the atmosphere, and contains fringe phase information which is not available to a two-element interferometer.

The above mentioned upgrades provide major improvements in three areas. First, the longer baselines will give the ISI higher resolution. This will enable accurate measurement of angular diameters and will yield details about structure on stellar surfaces. Secondly, the new phase information and coverage of more than one dimension will eliminate the need to assume axial symmetry about the line of sight to the source. Finally, the availability of three simultaneous baselines, along with sensitivity improvements due to tip-tilt correction and elimination of infrared power fluctuations, will drastically reduce the time necessary to map out a complete visibility curve for a star.

The visibility curves presented in Chapter 5 took an entire observing season (about 6 months) to map out. If the average quality of the data is low, it becomes necessary to spend many nights on the same region of the visibility curve in order to reduce the probable error to such a level that meaningful conclusions can be drawn. In addition, it requires at least a week to change the telescopes to a new baseline. It is conceivable that with three operating telescopes and a good signal-to-noise ratio, such curves could be measured in a week. Since it is apparent that many of the typical ISI targets change over time (see, for example, Hale *et al.* [34] or Bester *et al.* [8]), such rapid measurements would have substantial scientific value.

6.2 Optical and Infrared Interferometry

Although optical and infrared stellar interferometry are still relatively immature as compared with radio interferometry, rapid progress is being made, and the future looks very promising. Optical interferometers with more than two elements are now producing two-dimensional maps of stars. The first such result was produced by the Cambridge Optical Aperture Synthesis Telescope (Baldwin *et al.* [4]). A number of good measure-

ments have recently been made by the Navy Prototype Optical Interferometer (Benson *et al.* [5], Armstrong *et al.* [3]). At Mt. Wilson observatory, another near-infrared and visible interferometer, the CHARA array (McAlister *et al.* [62]), is under construction.

Early in the next century, ambitious efforts as part of NASA's Origins program may result in an interferometer using the Keck telescopes (Swanson *et al.* [85]), or even an interferometer in space (Unwin *et al.* [91]). Mid-infrared observations will play a prominent role in this program. Scattering by dust is much reduced at such relatively long wavelengths, allowing the observation of enshrouded objects. In addition, at $10\ \mu\text{m}$, the ratio between the Planck function for an object at 5800 K (a star) and that for an object at 290 K (a planet) is about 500. At 550 nm, in the visible, this ratio is 10^{37} ! Using the relative sizes of the Sun and the Earth, one can calculate that at $10\ \mu\text{m}$, an Earth-like planet would produce about 10^{-7} times as much radiation as its star. In the visible, thermal radiation from the planet is negligible. If 10% of the visible starlight hitting the planet is scattered, it will be about 10^{-10} times as bright as the star. Thus, it will be much easier to distinguish a planet from its star in the mid-infrared, although it will still be quite a challenge.

Even if planet detection is an elusive goal, it is clear that continued progress in stellar interferometry will allow us to overcome the limitations of conventional telescopes and expand our knowledge of the universe.

Appendix A

1997 Results on CIT 6

The observing season at Mt. Wilson typically lasts from early May through early November. During this period, the weather and seeing conditions are usually quite good, and though there are occasionally high clouds, rain and fog are quite rare. There can be a few good nights outside of this window, but most of the useful data gathered by the ISI have been obtained during the normal observing season.

This situation results in a preference for sources which are available all night during the summer months. Other sources, which appear closer to the Sun during the summer, are more difficult to collect a complete set of data on in one season. CIT 6, in the constellation Leo Minor, is one of these latter sources. We had originally hoped to measure the complete fringe visibility curve for CIT 6 in 1997, since the new guiding system is able to track this source, which was inaccessible to the old silicon CCD guider camera. Unfortunately, by the time the telescope servo system was repaired after a failure in the spring, CIT 6 was setting with the Sun. When it emerged later in the summer, observations of other sources (mainly IRC +10216) were given precedence.

Despite this unfortunate situation, CIT 6 was observed on the nights of October 20, November 22, and November 24. Valid data were obtained on October 20 and November 22, and the resulting points are shown in Figs. A.1 and A.2. The average position angle of the effective baseline during the measurements at 4.2 arcsec^{-1} was 305.6 degrees, where 0 degrees is north and 90 degrees is east. For the point at 6.5 arcsec^{-1} , the average position angle was 340.5 degrees.

The paucity of data on this source does not prevent us from drawing some conclusions from the visibility values which we have. The two relatively low values

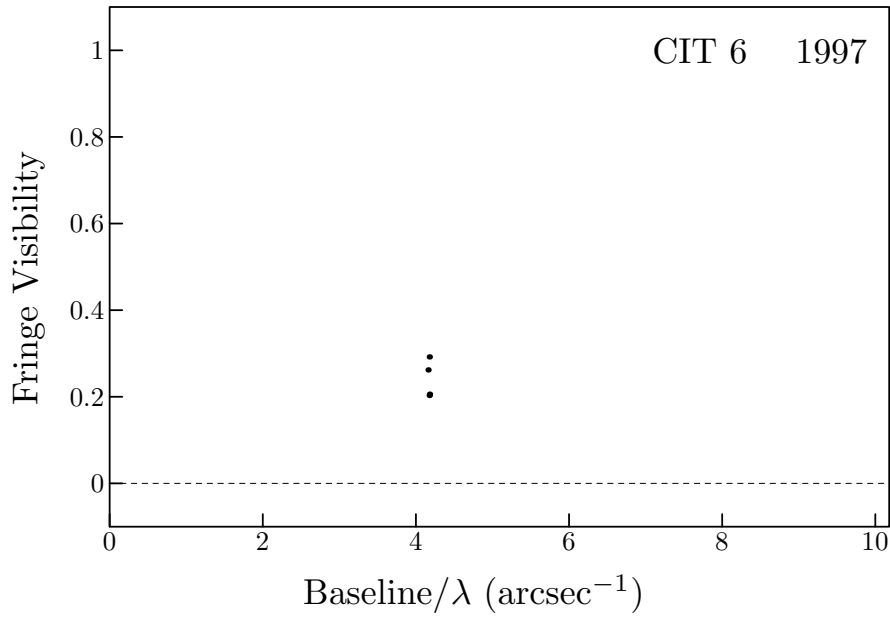


Figure A.1: Data points taken on CIT 6 with the interferometer on a 9.6 m baseline. Points taken on the 16.1 m baseline are not shown, since some negative fringe power measurements prevented the calculation of individual visibility values.

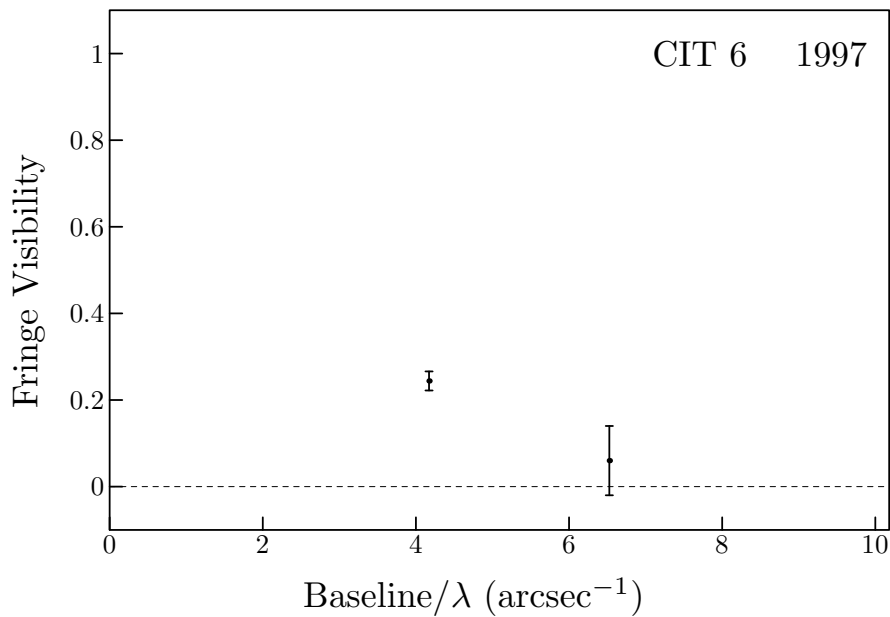


Figure A.2: Averaged fringe visibility values for CIT 6. The point at 4.2 arcsec^{-1} is the average of the points shown in Fig. A.1. The visibility value at 6.5 arcsec^{-1} was derived from the averages of the 16.1 m baseline fringe power and infrared power measurements.

shown in Fig. A.2 indicate that a substantial fraction of the power from the star and its dust shell has been resolved by the time the spatial frequency reaches 6.5 arcsec^{-1} . This puts some constraint on the spatial extent of the $11 \mu\text{m}$ emission.

In Fig. A.3 a simple Gaussian fit is shown with the two data points. The resulting $11 \mu\text{m}$ radial intensity profile (strictly valid only for a position angle of 306 degrees, unless spherical symmetry is assumed) is shown in the lower half of the figure. As can be seen, the flux at angular radii beyond $0.25''$ is negligible. At an estimated distance of 380 parsec to CIT 6 [60], $0.1''$ corresponds to 38 au, which is roughly the same as Pluto's average distance from the Sun. The data therefore demonstrate the enormous extent of the dust shell around this star.

More detailed information about the dust shell surrounding CIT 6 will become available in the near future, either from further ISI observations or from images taken with a mid-infrared camera on the Keck or another comparably sized telescope.

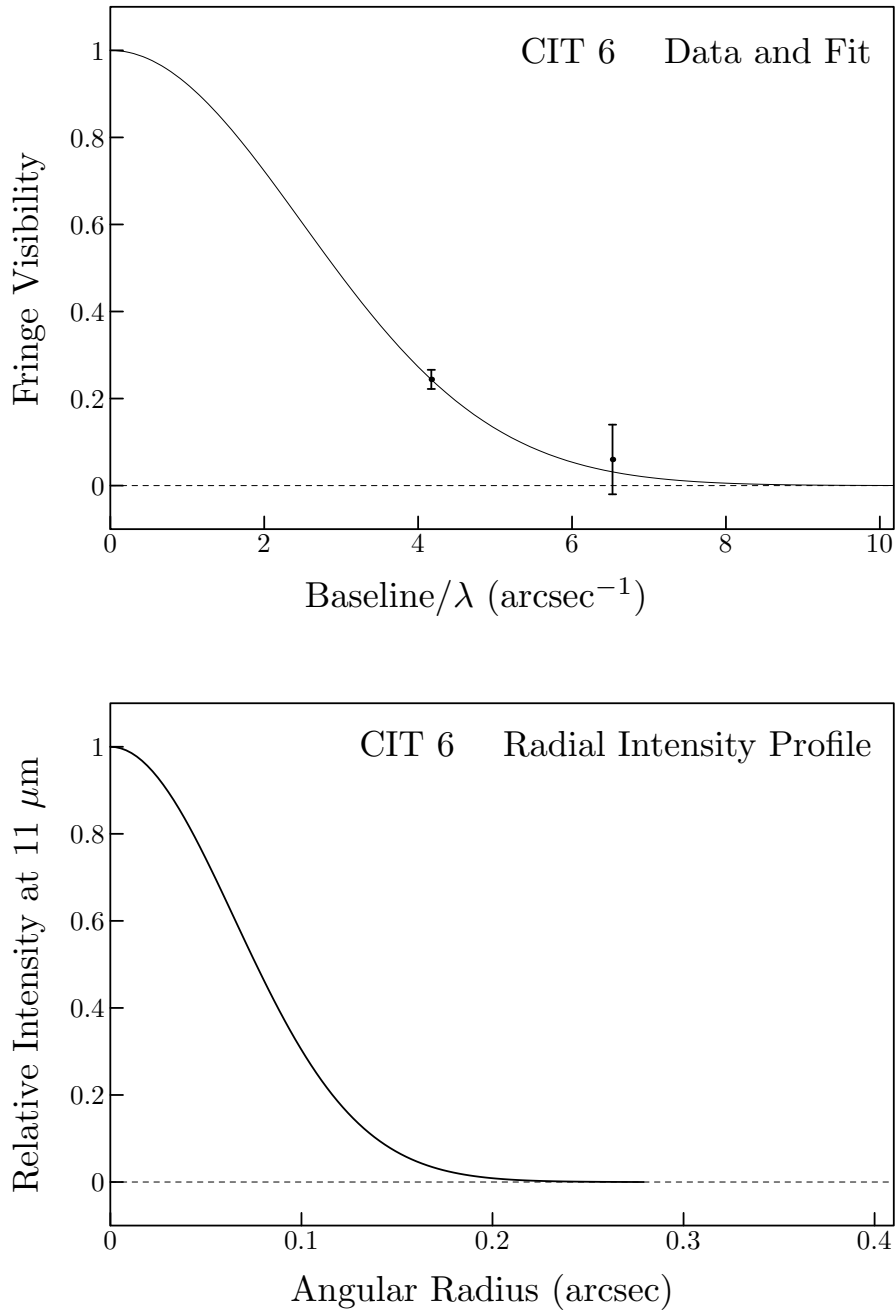


Figure A.3: CIT 6 data with a simple Gaussian fit and the corresponding 11 μm intensity profile. The model Gaussian, with a full-width at half-maximum (FWHM) of 6.0 arcsec $^{-1}$ corresponds to a Gaussian radial intensity profile with a FWHM of 0.15".

Appendix B

ISI Guiding System Manual

This manual describes the operating procedures, source code, network control interface, and computer hardware of the ISI telescope guiding system. The information presented here is specific to the ISI guiding system, and it is assumed that the reader has some familiarity with routine operation of the ISI, as well as some understanding of TCP/IP computer networks. For more detailed information about the operation of the guider camera and its control interface, see the Amber 4128 Infrared Camera System manual.

B.1 Startup and Shutdown Procedures

Startup:

1. **Cool the guider camera.**

After checking that the **guider lens and dewar window are properly covered**, remove the gold-colored plug from the top of the camera dewar. Insert the fill funnel into the dewar and fill with LN₂ **poured from the green thermos bottle. The guider camera takes approximately 30 minutes to cool to 77 K.**

2. **Turn on the guider camera control box.**

Boot-up takes approximately 100 seconds.

3. **Remove the dewar window cover.**

Reach over the front of the dewar with your left hand and pull on the knurled knob with your thumb and forefinger while holding the top of the cover with your right hand. **Do not turn the knob.**

4. **Remove the covers from the guider lens and dichroic beamsplitter.**

5. **Start the isiguide program on the guider PC.**

Turn on the monitor and computer if necessary. **If the computer is running the ftp server, press the d key to exit.** At the prompt, type isiguide to start the program.

Shutdown:**1. Quit the isiguide program.**

Type **Q** on the guider PC. Note that the **Q** must be capital. Type **f** followed by the **Enter** key to restart the ftp server.

2. Replace the gold-colored plug in the dewar.**3. Replace the dichroic beamsplitter and guider lens covers.****4. Replace the dewar window cover.**

Make sure the cover is completely inserted. **Do not turn the knob.**

5. Turn off the camera control box.

B.2 Panic Abatement Guide

- **The isiguide program froze or quit when I tried to start it.**

Make sure that the camera control box is on and has booted up. The isiguide program will not run if the control box is off. After boot-up, the message ADJUST CAMERA should appear in the control box display. **Make sure that the FPA CLOCK switch on the camera control box is set to 'INT'**. Type isiguide to restart the program. If you do not have a prompt, type Control-C or Control-Break, or reboot (press the reset button on the front of the computer) if necessary.

- **I'm pumping on the liquid nitrogen, and vertical stripes are starting to appear in the image, ruining the guiding.**

The best present theory is that this problem is caused by erratic behavior of the silicon readout electronics on the focal plane array at temperatures near 55 K. Momentarily vent the vacuum system with the finger-operated valve, then close off the pumping valve a bit so that the camera stabilizes at a slightly higher temperature.

- **The gray levels on the video screen are all messed up.**

Check to see that the LUT SELECT switch on the camera control box is set to 'A'.

- **Something went wrong with the PC and now it is talking to me in big, ugly letters.**

Type textmode or restart the isiguide program.

- **There are bad pixels on the PC screen which do not appear on the video monitors.**

Run the getvtab1 program on the guider PC. This program gets the correction table from the control box. It takes approximately 3 minutes to run.

- **The isiguide program quits and says it can't find the vector table file.**

See previous item.

- **The camera dewar fill funnel is not draining, and the LN₂ is calm in the funnel.**

Check for blockage with the wire dipstick.

- **The camera dewar fill funnel is not draining, and the LN₂ is spurting all over the place.**

Wait for about a minute while the dewar cools. This problem typically occurs when the dewar is almost full and the LN₂ contacts the warmer upper section of the container. The dewar should be topped off when the spurting stops. If the spurting does not stop, the dewar may need to be pumped out.

- **The isiguide screen is all messed up from error messages.**

Press `r` to refresh the screen. Check to make sure that the requests coming from the network are correct.

- **The isiguide program hung and said that there was an I/O card parity interrupt.**

Turn off the guider PC. Wait 10 seconds. Turn the PC on and try again.

- **I turned on the camera control box and it came up with an error message instead of the usual ADJUST CAMERA.**

Turn off the camera control box. Wait 10 seconds. Turn the control box back on.

B.3 Camera Calibration Procedure

This section contains step-by-step instructions for calibrating one of the Amber cameras. For more information about what is actually happening when you carry out these instructions, see the section on 'Calibration and System Start Up' in the Amber manual.

1. Place the calibration target in front of the guider lens.

Use caution when working near the guider optics. The target post should sit in the short post holder on the optics table. When properly mounted, the target should be about 66 mm from the front surface of the guider lens, with the 1 cm diameter white circle facing the camera. Make sure that the target is perpendicular to the axis of the guider optics, and that the covers have been removed from the guider optics. The target is kept in a post holder near the camera on the optics table.

2. Make sure that the camera control box is on and has booted up.

3. Quit any program which is running on the guider PC.

If `isiguide` is running, type `Q` to quit. At this point, you should have a DOS prompt.

4. On the guider PC, type

```
telnet -s amber
```

Wait for the telnet program to start, then press the left arrow key to get a menu. If the menu does not appear, try typing a capital `Y`, followed by the `Enter` key. Then press the left arrow.

5. Using the arrow keys, select INIT SYSTEM and press the Enter key.

Respond with `y` to the request for confirmation. Wait for initialization to complete.

6. Using the menu system, select the desired frame rate and integration time.

7. Make sure the camera is looking at the white circle at the center of the target.

8. Place the incandescent lamp so that the guider camera field of view is uniformly illuminated. THIS SHOULD BE CHECKED ON THE

VIDEO MONITOR. If using a frame rate lower than 109 per second, turn off the room lights.

- 9. Using the arrow keys, select 2-PT CALIBRATE and press the Enter key.**

Respond with y to the request for confirmation.

- 10. Hit a key on the guider PC to begin calibration.**

The camera will take 8 cold frames.

- 11. Turn on the incandescent lamp and hit a key on the PC.**

The camera will take 8 hot frames and recalculate the correction tables.

- 12. After calibration (about 20 seconds), press a key for confirmation.**

If there is an error, such as '>1024 BAD', check all optics and hardware (especially the lamp and target), and repeat the calibration.

- 13. Type Alt-X to exit the telnet program.**

- 14. Return the target to the storage location.**

- 15. Run the getvtabl program on the guider PC.**

Do this by typing

```
getvtabl
```

at the DOS prompt. If you do not do this, the calibration will not be taken into account by the PC. The `getvtabl` program takes approximately 3 minutes to run.

B.4 Pumping on the Liquid Nitrogen for Weak Star Observations

1. **Fill the camera dewar with liquid nitrogen.** When finished, you should have about 4 inches of LN₂ in the dewar, as measured by the dip stick.
2. **Turn on the camera control box.**
3. **After the box has booted up,** run
`init system`
 from either the camera control box front panel, or a
`telnet -s amber`
 session on the guider PC.
4. **Make sure that the guider camera lens cap is properly inserted** so that no stray light can reach the array.
5. **Start isiguide on the guider PC,** change the frame rate to 1 frame per second, the global gain to 1, and the global offset to 0. This can be accomplished from the guider PC console by typing, in slow succession, the lower case letters
`c f h z`
 You will use the mean pixel value displayed on the PC screen as a measure of the dark current as you pump on the camera.
6. **Assemble the pumping seal and insert the pumping hose into the seal and dewar mouth.** The seal is assembled with the o-ring on the bottom, touching the rim of the dewar mouth, the o-ring positioner above the ring, and the screw top holding them down.
7. **Turn on the rough vacuum pump.**
8. **Open the pumping valve about 1/4 turn** until you see LN₂ just start to boil up into the hose, then close the valve off a little to stop the boiling.
9. **Pump for about 10 or 15 minutes,** open the valve again until you see boiling, then close it off just enough to stop the boiling.

10. **By this time, you should be seeing the mean pixel value drop** on the guider PC screen. Wait until the mean drops below about 850 counts, then close the valve down until it is only open by about a 70-80 degree turn.
11. **Wait about 10 minutes** to see if the mean pixel value is stable. If not, close the valve off a bit if the counts are falling, and open it a bit if the counts are rising.
12. **Once the mean value is stable, quit isiguide**, change the camera frame rate to 7 frames per second, remove the lens cap, and do a two-point calibration of the guider camera. A good hot source for this calibration is one of the standard incandescent lights shining at the ceiling across the room.
13. **Run getvtabl on the guider PC.**
14. **Start isiguide and switch to 7 frames per second.**

NOTE: If while you are observing, twinkling vertical lines appear on the guider screen, open the pumping valve all the way and let in some air through the rough pump vent. The lines should disappear almost immediately. As soon as they are gone, close down the valve to a position slightly more closed off than you had it before removing the lines.

B.5 Camera Dewar Evacuation

In order to maintain their rated hold time of 10 hours, the guider camera dewars must occasionally be pumped out. The Amber dewars have performed very well, and this procedure has typically been carried out only twice per observing season. Detailed instructions for this procedure are in the Amber camera manual in the “Operation” section on page 16. The attachment for the hose to pump out the dewar is closed off with a blank flange, and is mounted on the vacuum hose connecting the cold load, signal, and phase lock (or path length compensator) dewars. Although in step 4 of the pumping procedure, it says to evacuate the foreline before threading the knob extension into the dewar plug, experience has shown that **The knob extension should be threaded into the dewar plug before the pumping is started.** The plug can then be removed (by pulling on the knob) after the foreline is evacuated.

B.6 Control Program and Network Interface

B.6.1 Source Code Description

The source code of `isiguide` is a C language program of approximately 4500 lines. The code is divided into 10 source modules (files) and a header file. There is also an associated `makefile` for building the program. The code can be found under the `isisoft` home directory in the `gdr` subdirectory on the UNIX workstations. The code must be compiled (and run) on the guider PCs, where it is kept in the `guider` subdirectory under the `C:` drive root directory. The current operational versions of the executables are kept in a directory called `custom`, also under the `C:` root directory. **This should be kept in mind when modifying the guider code**, since `C:\CUSTOM` precedes `C:\GUIDER` in the guider PC execution path. The executables are named `isiguide.exe` and `getvtabl.exe`.

It **should be noted** that there is a function in the `isiguide` code called `ms_pause()`. This function, defined in the module `serial.c`, pauses for a given number of milliseconds. This function is currently implemented as a loop, and is thus dependent on processor speed. This was done to obtain improved accuracy in timing, but **must be changed** if the code is ported to a machine other than a 66 MHz Intel 486-based PC. It should also be noted that this approach to implementing a delay would not be acceptable under a multitasking operating system.

Communication with the camera control box is carried out over an RS-232 serial line using commands which are documented in the Amber camera manual. The frame grabber card, manufactured by Dipix, is responsible for acquiring the digital image data, which is sent over a ribbon cable from the camera control box. The Dipix card came with a library of C language routines which are used to transfer the image from the card to the guider PC memory. The card and accompanying software are thoroughly described in the Dipix documentation.

The tip-tilt stage is driven via a simple digital to analog converter (DAC) card, the output of which is sent to amplifiers which multiply the DAC voltage by a factor of 10.

Communication between `isiguide` and the servo system is accomplished using an interface box containing a microcontroller. The new servo system, which will accept commands over the ethernet, will make this box obsolete. The box is driven over an

RS-232 serial line.

Since the guider PCs are running the MS-DOS operating system, which does not support networking, the Sun Microsystems PC-NFS package and the associated programmer's toolkit are used to provide the networking services. Slight differences exist between calls in this toolkit and the standard UNIX equivalents. The toolkit manuals can be consulted if confusion should arise about the network code. The PC-NFS package is now obsolete, and is no longer available.

B.6.2 Network Interface General Information

The `isiguide` program runs as a network server, and **does not know** which guider PC it is running on, nor which telescope it is controlling. This allows the guider code to be identical on all PCs. It is the responsibility of the central computers (the control workstation and the real-time computers) to determine which PC is to receive which commands. In the event that this situation needs to be changed, as for example when the guider code must be modified to communicate with the new servo system over the ethernet, it is **strongly suggested** that the `isiguide` program be modified to determine its identity dynamically so that the guider code remains identical on all machines.

The `isiguide` program responds to command requests made over Transmission Control Protocol (TCP) connections to one of four ports, `PICPORT`, `TBPORT`, `VMEPORT` and `CMDPORT`, all defined in `isiguide.h`. The command protocol is the same for the four ports, and is described below. All TCP connections are closed immediately after execution of the requested command. While this strategy may slightly increase response time, it has the overwhelming advantage of keeping the guider PCs independent of the other ISI computer systems during startup and operation.

During normal operation of the telescopes and guiding system, trackball and some guider commands are sent over the network from the control workstation by the `yguider` user interface program. This program provides a graphical interface for controlling the guiding system. The `yguider` program is a multi-threaded Motif-based C language program of approximately 2500 lines. The source code for `yguider` can be found under `~isisoft/els/` on the UNIX workstations.

The procedure for handling a network request is as follows. When a connection request comes in from the network, `isiguide` calls the function `answer_call()`, located in the module `network.c`. This routine accepts connections from any machine with an `'isi'` or a `'vme'` in its name. (NOTE: Access control has been disabled as of 20 September 1996 in order to improve response time and prevent Domain Name Service requests from the PCs, which must be sent outside of the ISI telescope network segment.) Once the calling host has been verified, the connection is made, and a file descriptor for the open connection is returned. At this point, the connection is directed to the appropriate service routine, all of which are located in `control.c`. The service routine

then calls the function `read_command()`, also located in `control.c`. `read_command()` reads the command request from the network. It has various features to prevent an errant command request from stopping the guiding (this can happen because MS-DOS is a single-tasking operating system). If the network connection stalls for more than 3 seconds, it is closed. Also, the command requests are limited to 64 characters. The command is read up to the first linefeed or carriage return character. After the command is read, the service routine either performs the command if the request is valid, or sends back an error message over the network if the command is not valid.

For debugging or other purposes, commands to `TBPORT` and `CMDPORT` may be sent directly to the guider PC using the `sock` program, which is available on the SPARC workstations. For example, to send a command to `TBPORT` on `isicam1`, one might log in to `isi10` and type

```
sock -v -h isicam1 56804
```

where here `TBPORT` is 56804. After the connection is made, one could type a command, such as

```
rset
```

followed by a return. For `CMDPORT` commands, there are scripts available on `isi5` and `isi10` called `gc1`, `gc2`, and `gc`, which send a command to guider 1, guider 2, or both guiders, respectively. For example,

```
gc1 x
```

issued from the prompt on `isi10` would toggle the aim box on guider 1. There are also scripts available on `isi10` called `tb1` and `tb2` for sending commands to `TBPORT`.

B.6.3 Picture Request

A request to the `isiguid` program to return the current image from the guider camera can be made by opening a TCP connection to `PICPORT`. Requests to this port are handled by the routine `service_picrequest()`, located in the module `control.c`. The three character request `'pic'`, in lower case letters, plus a terminating linefeed or carriage return, must be sent over the TCP connection. If the correct request is received, `isiguid` returns the image over the TCP connection, one byte per pixel, with values from 0 to 255, where 255 represents the brightest possible pixel. The image is sent row by row starting at the upper left hand corner. With the current array size of 128×128 , the returned image is 16,384 bytes. The connection is then closed. If an incorrect request is received, a brief error message is returned, and the connection is closed.

B.6.4 Trackball Commands

The trackball interface to the `isiguide` program is accessed by opening a TCP connection to `TBPORT`. Requests made to `TBPORT` are handled by the routine `service_trackball()`, located in the module `control.c`. A request sent to `TBPORT` must consist of 4 or more characters plus a terminator, in the following form:

```
cccc[n... ]t
```

where the first four characters (`cccc`) are the command to be executed. If required by the command, the subsequent characters (`n...`) represent a floating point number, and the last character (`t`) is a terminating linefeed or carriage return. An example of a valid command is `"+scy20.0\n"` which would move the telescope such that the image on the guider screen would move down by 20.0 arc seconds (The guider screen coordinates are positive to the right in x and positive down in y).

The trackball commands are as follows. A number equal to the angle to be moved in arc seconds and a trailing linefeed or carriage return are to be appended to each command (except for `mark` and `rset`, which require no number) listed here before it is sent over the TCP connection:

`+alt` This command moves the telescope so that it is looking at a position greater in altitude on the sky by the specified angle in arc seconds. For example, `+alt23.2` would move the telescope to a position 23.2 arc seconds greater in altitude on the sky. Note that increasing altitude on the sky will not necessarily move the star parallel to one of the screen axes, will not necessarily move only one telescope axis, and will usually make the star move down on the camera screen.

Technical Note: In order to send pure **telescope** azimuth and altitude counts, one must set the field rotation angle to 0 with the guider command `'OR0'`, and one must also set the guider coordinate transformation matrix to be diagonal, for example with the guider command `'OE230 0 0 150'`. `alt` and `azi` commands will then result in pure movements of the corresponding telescope axis. **After this is done, the guider coordinate transformations and rotation angle must be updated before the guiding will work again.**

`-alt` This command moves the telescope down in altitude on the sky by the specified angle in arc seconds.

- +azi** This command moves the telescope to a position greater in azimuth on the sky by the specified angle in arc seconds. The azimuth angle on the sky increases as one moves from north through east and south to west and back to north.
- azi** This command moves the telescope to a position smaller in azimuth on the sky by the specified angle in arc seconds.
- +scx** This command moves the telescope such that the x coordinate of the star image on the guider camera screen increases by the specified angle in arc seconds. The guider camera screen coordinate system uses two coordinates, x and y , such that when one is facing the screen, x increases to the right, and y increases downward. For example, the command '+scx7.5' would have the effect of moving the star image 7.5 arc seconds to the right on the guider camera screen. The screen is 128×128 pixels, with each pixel corresponding to 0.3106 arc seconds on the sky (this is the `SECSPERPIXEL` constant, defined in `isiguide.h`), so the width and height of the screen are both $0.3106 \times 128 = 39.8$ arc seconds.
- scx** This command moves the telescope such that the x coordinate of the star image on the guider camera screen decreases by the specified angle in arc seconds.
- +scy** This command moves the telescope such that the y coordinate of the star image on the guider camera screen increases by the specified angle in arc seconds. For example, the command
- ```
tb1 +scy10.0
```
- issued from the UNIX workstation would have the effect of moving the star image 10.0 arc seconds **down** on the guider camera screen in telescope 1. See the **+scx** command above for an explanation of screen coordinates.
- scy** This command moves the telescope such that the  $y$  coordinate of the star image on the guider camera screen decreases by the specified angle in arc seconds.
- mark** This command incorporates the currently added counts in the servo microprocessor and sets the added counts to zero. This command should not be followed by a number. For example, one could send the string "mark\n" over the TCP connection.

**rset** This command removes the added counts in the servo microprocessor. This command should not be followed by a number.

### B.6.5 Guider Commands

An extensive set of commands is accepted over a TCP connection to CMDPORT or VMEPORT in order to allow remote control of the guiding system by xobserve and the real-time computers. Command requests to the two ports are treated identically. VMEPORT was only created in order to prevent a problem which was caused by a flaw in the PC-NFS network software. All programs which run on the UNIX workstations use CMDPORT, and the real-time computers use VMEPORT. The commands issued to these ports are interpreted by the `service_command_request()` routine, located in module `control.c`. The commands consist of a variable length message sent over the TCP connection in the following format:

NL[L...][n...]t

N is a single digit which usually indicates which telescope the command is meant for. This digit is ignored by the `isiguide` program, but **MUST** be present for spacing purposes. **This digit is automatically supplied by the gc scripts!**

L[L...] represents one **or more** characters which indicate what the command is. See descriptions below.

[n...] represents one **or more** characters which make up a number to be read by either the `atof()` or the `atoi()` function. This field is **not always present**.

t is a termination character which may be a linefeed or a carriage return.

**The commands (L[L...] field above) are as follows:**

@ **Spiral search.** This command begins the spiral search. **During the spiral search, the only recognized command is '@'.**

~ **Abort spiral search.** This command causes the spiral search to be aborted with the telescope left in its current position. **This command is not recognized except during a spiral search.**

& **Enter chopping mode** This switches the guiding system into an experimental mode where the tip-tilt mirror is used to chop on and off the star using the mirror's maximum possible throw. The system will leave chopping mode upon receipt of the 7 command.

7 **Exit chopping mode.** This command is used to exit the experimental chopping mode. See the `&` command for more information.

a **Automatic contrast adjustment.** This command adjusts the contrast by taking 4 frames and then changing the global gain and offset in the Amber camera control box. See the Amber manual for more information about the global gain and offset adjustments.

eb **Toggle background subtraction.** Background subtraction is performed on the guider PC. Although the subtraction is taken into account by the PC, **you will not see a change on the video display.**

eg **Grab background frame.** Grabs a frame to be used as the background when background subtraction is activated.

E **Set values in the coordinate transformation matrix.** This command is used to provide the guider PC with values for 4 variables, `azAzCountsG`, `azAltCountsG`, `altAzCountsG`, and `altAltCountsG`. These values tell `isiguide` how many encoder counts to move each telescope axis in order to move a given distance on the sky. Since `isiguide` is not aware of where the star is in the sky, these values must be supplied by the real-time computers. For compatibility reasons, the numbers supplied in the command represent the number of counts required to move 10 arc seconds on the sky. Internally, however, `isiguide` stores the number of counts required to move 1 arc second. In other words, `isiguide` divides the supplied numbers by 10 before storing them in the variables. For example, to reset the transformation matrix to its default values, one would send the command `'0E230 0 0 150'`. The command specifies 4 numbers, separated by spaces. These numbers correspond to the 4 variables listed above in the order given there. If the example command were received, therefore, the number 230 would be divided by 10, and the value 23.0 would be stored in the variable `azAzCountsG`. `isiguide` would then know that in order to move 1 arc second in azimuth **on the sky**, it would have to send 23.0 counts to the telescope azimuth servo. Likewise, `azAltCountsG` stores the number of telescope altitude axis encoder counts required for a 1 arc second movement in azimuth on the sky, `altAzCountsG` stores the number of telescope azimuth axis counts required for a 1 arc second movement

in altitude on the sky, and `altAltCountsG` contains the number of telescope altitude counts necessary for a 1 arc second altitude movement on the sky. Although the default matrix is diagonal (the `altAzCountsG` and `azAltCountsG` cross terms are 0), in general this will not be the case, and both telescope axes will need to be moved in order to move along a given sky coordinate. In order to manually set the transformation matrix, one could type

```
gc 'E230 0 0 150'
```

on the UNIX command line. Note that quotes are necessary in the UNIX command because of the spaces in the guider command message. See the `R` command for related information.

**f Set frame rate.** This command sets the frame rate for the guider camera. The following values, in frames per second, are accepted: 1, 3, 7, 14, 27, 54, 109, and 217. The default value upon startup is 109. Example:

```
gc1 f27
```

would set the frame rate to 27 frames per second for guider 1. See the `i` command for information about the integration time.

**gn Turn off guiding.** `isiguide` will disable the guiding. This also works in tip-tilt mode.

**gy Turn on guiding.** `isiguide` will enable the guiding loop. After a star has been located in the field of view, it will be moved to the center of the aim box, and the `'locked'` indication will appear on the video screen and the guider PC monitor.

**gt Turn on tip-tilt.** If locked on a star, `isiguide` will enter the tip-tilt loop.

**hc Remove guiding offset.** This will center the star during position switching. The current guiding offset is stored in the global variables `guidingOffsetG[0]` and `guidingOffsetG[1]`, which hold the screen  $x$  coordinate offset and screen  $y$  coordinate offset, respectively.

**hd Set guiding offset to the 'down' position.** This causes guiding about a position which is `SMALLMOVE` arc seconds down **on the sky** from the center of the screen. Rarely will a motion in a particular direction on the sky correspond to motion in the same direction on the guider screen. The screen  $x$  and screen

$y$  offsets are computed using the rotation angle, `fieldRotAngleG` and stored in `guidingOffsetG[0]` and `guidingOffsetG[1]`. `BIGMOVE` and `SMALLMOVE` are defined in `isiguide.h`.

**hD Set guiding offset to the 'far down' position.** This causes guiding about a position which is `BIGMOVE` arc seconds down **on the sky** from the center of the screen. See the `hd` command for more information.

**hL Set guiding offset to the 'close left' position.** This causes guiding about a position which is `SMALLMOVE` arc seconds left **on the sky** from the center of the screen. See the `hd` command for more information.

**hL Set guiding offset to the 'far left' position.** This causes guiding about a position which is `BIGMOVE` arc seconds left **on the sky** from the center of the screen. `BIGMOVE` is defined in `isiguide.h`. See the `hd` command for more information.

**hq Hotspot query.** The response to this command is a string containing the current values of the IR guiding offset (see the `hx` command below). Example:

```
gc hq
```

will show the values of the IR guiding offset. The IR guiding offset is often referred to as the 'hotspot'.

**hr Set guiding offset to the 'close right' position.** This causes guiding about a position which is `SMALLMOVE` arc seconds right **on the sky** from the center of the screen. See the `hd` command for more information.

**hR Set guiding offset to the 'far right' position.** This causes guiding about a position which is `BIGMOVE` arc seconds right **on the sky** from the center of the screen. See the `hd` command for more information.

**hu Set guiding offset to the 'up' position.** This causes guiding about a position which is `SMALLMOVE` arc seconds up **on the sky** from the center of the screen. See the `hd` command for more information.

**hU Set guiding offset to the 'far up' position.** This causes guiding about a position which is `BIGMOVE` arc seconds up **on the sky** from the center of the screen. See the `hd` command for more information.

**hx Set IR guiding offset x component.** The IR guiding offset, often referred to as the 'hotspot,' is stored in the global variables `irOffsetG[0]` and `irOffsetG[1]`, which contain the screen  $x$  and  $y$  components of the offset, respectively. This offset is independent of, and in addition to, the guiding offset described above. Unlike the guiding offset, the IR guiding offset is specified in **screen coordinates**. The IR guiding offset is stored on disk, and can be reloaded when `isiguide` starts up. This feature is currently disabled in order to prevent confusion about the behavior of the guiding system. The values of the IR guiding offset are returned by the `hq` command (see above). The number field of the `hx` command consists of a single floating point number which is the offset from the center of the screen in arc seconds. Example:

```
gc hx-2.3
```

would, in the absence of a guiding offset, cause the guiding to be centered about a position 2.3 arc seconds to the left of center **on the screen** for both guiders.

**NOTE:** The use of an IR guiding offset is discouraged by the author until such time as a reliable and repeatable method for determining the proper value of the offset is found. The usual beam mapping procedure does not seem as reliable as a simple realignment, and the author does not know what field rotation angle is used to compute the suggested offset produced by the `beammap` program. There is a very good chance that the angle is incorrect.

**hy Set IR guiding offset y component.** See the `hx` command above.

**i Set integration time.** This command sets the fraction of the inverse frame rate during which the guider camera collects light. The `n` field of this command is an integer between 0 and 62, which is the integration time in 64ths of the inverse frame rate. The default value upon startup is 52. Example:

```
gc i61
```

would set the integration time to 61/64 of the inverse frame rate for both guider PCs. See the `f` command for more information about the frame rate.

**n Normalization control.** This command turns the normalization of the PC display image brightness on or off. It has no effect on the video monitor display and is rarely used over the network.

**R Set field rotation angle.** This angle, which is stored in the global variable `fieldRotAngleG`, is the angle between the guider screen vertical direction and the vertical direction on the sky (toward the zenith from where the telescope is pointed). In the `isiguide` program, this angle ranges from -180 degrees to +180 degrees, with 0 degrees meaning that down on the guider screen ( $+y$ ) is the direction on which a line in the sky from the star (at the center of the guider field of view) to the zenith would lie if imaged onto the screen. The rotation angle increases as the imaged line from the sky moves clockwise on the guider screen. If this angle is zero, then an increase in elevation of the observed point on the sky will result in a pure vertical motion on the guider screen. This definition of the field rotation angle differs by a sign from that calculated by the real-time system, so the sign of the angle specified in the command is flipped before the rotation angle is stored in `fieldRotAngleG`. The number field of this command is an integer specifying the angle in degrees. Example:

```
gc2 R74
```

would set the field rotation angle for guider 2 to 74 degrees. See the **E** command for related information about the guider coordinate transformation.

**s Status Request.** This command has the `isiguide` program return the value of its `statusFlagG` global variable over the TCP connection. As an example, to send this command, one would write the string `"0s\n"` to the file descriptor representing the TCP connection to `CMDPORT`. Alternatively, one could use the `gc1` script:

```
gc1 s
```

`statusFlagG` is a single character which can be

'S' Searching for star.

'L' Locked on star.

'D' Disabled.

'T' Tip-tilt loop running.

**t Set tip-tilt position.** This command, which requires two space-separated numbers, sets the screen  $x$  and  $y$  positions of the star using the tip-tilt mirror. For example, if the guiding were disabled and the command

```
gc2 't1.0 -1.5'
```



were issued on the UNIX command line, The star on guider screen 2 would move 1.0 arc second to the right and 1.5 arc seconds up. The maximum throw of the tip-tilt mirror in any direction is 2.12 arc seconds, so  $\sqrt{x^2 + y^2}$  should be  $\leq 2.12$ .

**x Toggle aim box.** This command turns the 4 arc second aim box on or off (depending on its current state) on the guider display.

### B.6.6 Guider PC Hardware Configuration

This section contains miscellaneous technical details about the hardware configuration of the guider PCs. The ISI guiding system currently runs on two 66 MHz Intel 486-based PCs, one for each telescope. The PCs each contain 4 expansion cards:

1. **CD-ROM interface card.** IRQ: 15, memory address: 0x170.
2. **3COM network interface card.** IRQ: 10, memory address: 0x300.
3. **Dipix P360F frame grabber.** Memory address: 0x310. No interrupt level. Jumpers are set as specified for the Amber Camera in the Dipix Camera Interface Manual.
4. **DAC (tip-tilt driver).** Memory address: 0x330. No interrupt level. DIP switches on this card are set as follows, with U being up and D being down:

Address selector: DDUUDD

Gain Selector: DUUUDD (all gains set to 0–10 Volts)

The wait state was left off. Jumpers were moved to the position closest to the DIP switches in order to select simultaneous update of all channels. The outputs of the DAC are on pins 18, 16, and 14 of the D-shell connector for channels 0, 1, and 2 respectively. Ground is on pins 19, 17, and 15. Although the three channels are also referred to as A, B, and C and 1, 2, and 3, the same order is maintained all the way through the amplifiers to the piezoelectric stage.

# Bibliography

- [1] C. W. Allen. *Astrophysical Quantities*. Athlone Press, third edition, 1976.
- [2] Amber Engineering, Incorporated. *AE4128 Infrared Imaging System*. Amber Engineering, Goleta, CA, 1992.
- [3] J. T. Armstrong, D. Mozurkewich, L. J. Rickard, D. J. Hutter, J. A. Benson, P. F. Bowers, N. M. Elias II, C. A. Hummel, K. J. Johnston, D. F. Buscher, J. H. Clark III, L. Ha, L. C. Ling, N. M. White, and R. S. Simon. The Navy Prototype Optical Interferometer. *Astrophysical Journal*, 496:550+, March 1998.
- [4] J. E. Baldwin, M. G. Beckett, R. C. Boysen, D. Burns, D. F. Buscher, G. C. Cox, C. A. Haniff, C. D. Mackay, N. S. Nightingale, J. Rogers, P. A. G. Scheuer, T. R. Scott, P. G. Tuthill, P. J. Warner, D. M. A. Wilson, and R. W. Wilson. The first images from an optical aperture synthesis array: mapping of Capella with COAST at two epochs. *Astronomy and Astrophysics*, 306:L13+, February 1996.
- [5] J. A. Benson, D. J. Hutter, N. M. Elias II, P. F. Bowers, K. J. Johnston, A. R. Hajian, J. T. Armstrong, D. Mozurkewich, T. A. Pauls, L. J. Rickard, C. A. Hummel, N. M. White, D. Black, and C. S. Denison. Multichannel optical aperture synthesis imaging of Lambda1 Ursae Majoris with the Navy Prototype Optical Interferometer. *Astronomical Journal*, 114:1221–1226, September 1997.
- [6] M. Bester, W. C. Danchi, C. G. Degiacomi, and P. R. Bratt. The U.C. Berkeley Infrared Spatial Interferometer—recent system upgrades and analysis of atmospheric fluctuations. *Proc. SPIE*, 2200:274–285, 1994.
- [7] M. Bester, W. C. Danchi, C. G. Degiacomi, L. J. Greenhill, and C. H. Townes. At-

- mospheric fluctuations—empirical structure functions and projected performance of future instruments. *Astrophysical Journal*, 392:357–374, June 1992.
- [8] M. Bester, W. C. Danchi, D. Hale, C. H. Townes, C. G. Degiacomi, D. Mekarnia, and T. R. Geballe. Measurement at 11 micron wavelengths of the diameters of Alpha Orionis and Alpha Scorpii: Changes in effective temperature of Alpha Orionis and very recent dust emission. *Astrophysical Journal*, 463:336+, May 1996.
- [9] M. Bester, W. C. Danchi, and C. H. Townes. Long baseline interferometer for the mid-infrared. *Proc. SPIE*, 1237:40–48, 1990.
- [10] Manfred Bester. Astronomical coordinate transformations, pointing and interferometry calculations for the U.C. Berkeley Infrared Spatial Interferometer. Technical report, U.C. Berkeley Space Sciences Laboratory, 1990.
- [11] Albert Louis Betz. *Infrared Heterodyne Spectroscopy of Carbon Dioxide in Planetary Atmospheres*. PhD thesis, University of California at Berkeley, 1977.
- [12] Philip R. Bevington. *Data Reduction and Error Analysis for the Physical Sciences*. McGraw-Hill, 1969.
- [13] E. E. Bloemhof, W. C. Danchi, and C. H. Townes. Spatially resolved dust around IRC +10420. In G. Wallerstein, editor, *Proceedings of the Sixth Cambridge Workshop on Cool Stars, Stellar Systems, and the Sun*, Seattle, WA, 1989.
- [14] Max Born and Emil Wolf. *Principles of Optics*. Pergamon Press, sixth edition, 1980.
- [15] P. F. Bowers. VLA observations of 1612 and 1667 MHz OH masers associated with IRC +10420. *Astrophysical Journal*, 279:350–357, April 1984.
- [16] P. F. Bowers, K. J. Johnston, and J. H. Spencer. Circumstellar envelope structure of late-type stars. *Astrophysical Journal*, 274:733–754, November 1983.
- [17] Ronald N. Bracewell. *The Fourier Transform and Its Applications*. McGraw-Hill, 2<sup>nd</sup> edition, 1986.
- [18] R. Hanbury Brown, J. Davis, and L. R. Allen. The angular diameters of 32 stars. *Mon. Not. R. Astron. Soc.*, 167:121–136, 1974.

- [19] R. Hanbury Brown and R. Q. Twiss. Correlation between photons in two coherent beams of light. *Nature*, 177:27–29, 1956.
- [20] Centre de Données astronomiques de Strasbourg. SIMBAD database.
- [21] Se-Hyung Cho, Hyun-Soo Chung, Hyo-Ryoung Kim, Bob-Young Oh, Chang-Hoon Lee, and Seog-Tae Han. Observations of SiO ( $v = 0, 1, 2$ )  $J = 3-2$  and  $J = 2-1$  emission in late-type stars. *Astrophysical Journal Supplement*, 115:277+, April 1998.
- [22] Julian C. Christou. Image quality, tip-tilt correction, and shift-and-add infrared imaging. *Pub. Astr. Soc. Pac.*, 103:1040–1048, 1991.
- [23] L. M. Close and D. W. McCarthy, Jr. High-resolution imaging with a tip-tilt cassegrain secondary. *Pub. Astr. Soc. Pac.*, 106:77–86, 1994.
- [24] Michael L. Cobb and John D. Fix. Infrared speckle interferometry and imaging of several OH/IR stars. *Astrophysical Journal*, 315:325–336, April 1987.
- [25] W. C. Danchi, M. Bester, C. G. Degiacomi, L. J. Greenhill, and C. H. Townes. Characteristics of dust shells around 13 late-type stars. *Astronomical Journal*, 107:1469–1513, April 1994.
- [26] P. J. Diamond, R. P. Norris, and R. S. Booth. The peculiar circumstellar envelope around IRC+10420. *Astronomy and Astrophysics*, 124:L4–L6, July 1983.
- [27] H. M. Dyck, B. Zuckerman, Ch. Leinert, and S. Beckwith. Near-infrared speckle interferometry of evolved stars and bipolar nebulae. *Astrophysical Journal*, 287:801–813, December 1984.
- [28] A. S. Eddington. The internal constitution of the stars. *Nature*, 106:14+, 1920.
- [29] H. Fizeau. Prix Borodin: Rapport sur le concours de l’année 1867. *Comptes Rendus de l’Académie des Sciences*, 66:932–934, 1868.
- [30] D. L. Fried. Statistics of a geometric representation of wavefront distortion. *J. Opt. Soc. Am.*, 55:1427–1435, 1965.
- [31] David L. Fried. Optical heterodyne detection of an atmospherically distorted signal wave front. *Proc. IEEE*, 55:57–67, 1967.

- [32] Daniel Y. Gezari, Marion Schmitz, Patricia S. Pitts, and Jaylee M. Mead. *Catalog of Infrared Observations*. NASA Reference Publication 1294, Greenbelt, MD, 1993.
- [33] Michel Goossens, Frank Mittelbach, and Alexander Samarin. *The L<sup>A</sup>T<sub>E</sub>X Companion*. Addison-Wesley, 1994.
- [34] David D. S. Hale, M. Bester, W. C. Danchi, S. Hoss, E. Lipman, J. D. Monnier, P. G. Tuthill, C. H. Townes, M. Johnson, B. Lopez, and T. R. Geballe. Multiple dust shells and motions around IK Tauri as seen by infrared interferometry. *Astrophysical Journal*, 490:407–411, 1997.
- [35] C. J. Hansen and S. D. Kawaler. *Stellar Interiors*. Springer-Verlag, 1994.
- [36] Eric W. Hansen. Fast hankel transform algorithm. *IEEE Transactions on Acoustics, Speech, and Signal Processing*, ASSP-33:666–671, 1985.
- [37] R. M. Humphreys, D. W. Strecker, T. L. Urdock, and F. J. Low. IRC +10420—another Eta Car. *Astrophysical Journal Letters*, 179:L49+, January 1973.
- [38] Roberta M. Humphreys, Nathan Smith, Kris Davidson, Terry Jay Jones, Robert T. Gehrz, Christopher G. Mason, Thomas L. Hayward, James R. Houck, and Joachim Krautter. HST and infrared images of the circumstellar environment of the cool hypergiant IRC +10420. *Astronomical Journal*, 114:2778+, December 1997.
- [39] Z. Ivezić and M. Elitzur. Infrared imaging of late-type stars. *Mon. Not. R. Astron. Soc.*, 279:1011–1018, April 1996.
- [40] P.R. Jewell, J.C. Webber, and L.E. Snyder. The linear shell diameter of IRC+10011. *Astrophysical Journal Letters*, 242:L29+, November 1980.
- [41] M. A. Johnson, A. L. Betz, and C. H. Townes. 10  $\mu$ m heterodyne stellar interferometer. *Phys. Rev. Lett.*, 33:1617+, 1974.
- [42] Michael Allan Johnson. *An Infrared Stellar Interferometer Using Heterodyne Detection*. PhD thesis, University of California at Berkeley, 1975.
- [43] Terry Jay Jones, Roberta M. Humphreys, Robert D. Gehrz, Geoffrey F. Lawrence, Franz-Josef Zickgraf, Harvey Moseley, Sean Casey, William J. Glaccum, Carol J.

- Koch, Robert Pina, Barbara Jones, Kim Venn, Otmar Stahl, and Sumner G. Starfield. IRC +10420: A cool hypergiant near the top of the H-R diagram. *Astrophysical Journal*, 411:323–335, July 1993.
- [44] M. Jura. Dust particle size distributions around oxygen-rich mass-losing red giants. *Astrophysical Journal*, 472:806+, December 1996.
- [45] K. Justtanont, C. J. Skinner, and A. G. G. M. Tielens. Molecular rotational line profiles from oxygen-rich red giant winds. *Astrophysical Journal*, 435:852–863, November 1994.
- [46] K. Justtanont and A. G. G. M. Tielens. Mass loss from OH/IR stars: Models for the infrared emission of circumstellar dust shells. *Astrophysical Journal*, 389:400–412, April 1992.
- [47] Joel H. Kastner and David A. Weintraub. The massive post-red supergiants IRC +10420 and HD 179821. *Astrophysical Journal*, 452:833+, October 1995.
- [48] R. H. Kingston. *Detection of Optical and Infrared Radiation*. Springer-Verlag, 1978.
- [49] V. G. Klochkova, E. L. Chentsov, and V. E. Panchuk. Optical spectrum of the IR source IRC+10420 in 1992-1996. *Mon. Not. R. Astron. Soc.*, 292:19–26, November 1997.
- [50] G. R. Knapp and M. Morris. Mass loss from evolved stars. III. Mass loss rates for fifty stars from CO J = 1-0 observations. *Astrophysical Journal*, 292:640–669, May 1985.
- [51] Donald E. Knuth. *The T<sub>E</sub>Xbook*. Addison-Wesley, 1984.
- [52] Donald E. Knuth. Remarks to celebrate the publication of computers & typesetting. *TUGboat*, 7(2):95–98, 1986.
- [53] Leslie Lamport. *L<sup>A</sup>T<sub>E</sub>X: A Document Preparation System*. Addison-Wesley, 1986.
- [54] Peter R. Lawson, editor. *Selected Papers on Long Baseline Stellar Interferometry*, volume MS 139 of *Milestone Series of Selected Reprints*. SPIE Optical Engineering Press, Bellingham, WA, 1997.

- [55] T. Le Bertre. Oxygen-rich late-type star lightcurves in the 1-20 microns range. *Astronomy and Astrophysics Supplement Series*, 97:729–753, February 1993.
- [56] T. Le Bertre and J. M. Winters. On the relations between infrared colors and mass loss rates for Mira stars. *Astronomy and Astrophysics*, 334:173–180, June 1998.
- [57] P. Le Sidaner and T. Le Bertre. Optical and infrared observations of 27 oxygen-rich stars. Modelling of the circumstellar dust shells. *Astronomy and Astrophysics*, 314:896–908, October 1996.
- [58] B. M. Lewis, Y. Terzian, and J. Eder. New OH observations of the supergiant IRC +10420. *Astrophysical Journal Letters*, 302:L23–L26, March 1986.
- [59] S. G. Lipson, H. Lipson, and D. S. Tannhauser. *Optical Physics*. Cambridge University Press, 1995.
- [60] C. Loup, T. Forveille, A. Omont, and J.F. Paul. CO and HCN observations of circumstellar envelopes. A catalogue—mass loss rates and distributions. *Astron. Astrophys. Suppl.*, 99:291–377, 1993.
- [61] John S. Mathis, William Rumpl, and Kenneth H. Nordsieck. The size distribution of interstellar grains. *Astrophysical Journal*, 217:425+, 1977.
- [62] Harold A. McAlister, William G. Bagnuolo, Theo Ten Brummelaar, W. I. Hartkopf, N. H. Turner, Allen K. Garrison, William G. Robinson, and Stephen T. Ridgway. CHARA array. *Proc. SPIE*, 2200:129–139, June 1994.
- [63] A. A. Michelson. On the application of interference methods to astronomical measurements. *Phil. Mag.*, 30:1–20, 1890.
- [64] A. A. Michelson. Measurement of Jupiter’s satellites by interference. *Nature*, 45:160–161, 1891.
- [65] A. A. Michelson and F. G. Pease. Measurement of the diameter of  $\alpha$  Orionis with the interferometer. *Astrophysical Journal*, 53:249–259, 1921.
- [66] Peter W. Milonni and Joseph H. Eberle. *Lasers*. John Wiley & Sons, 1988.
- [67] J. D. Monnier. Private communication.



- [68] J. D. Monnier, M. Bester, W. C. Danchi, M. A. Johnson, E. A. Lipman, C. H. Townes, P. G. Tuthill, T. R. Geballe, D. Nishimoto, and P. W. Kervin. Nonuniform dust outflow observed around infrared object NML Cygni. *Astrophysical Journal*, 481:420+, May 1997.
- [69] J. D. Monnier, T. R. Geballe, and W. C. Danchi. Temporal variations of midinfrared spectra in late-type stars. *Astrophysical Journal*, 502:833+, August 1998.
- [70] R. L. Mutel, J. D. Fix, J. M. Benson, and J. C. Webber. High-resolution OH maser observations of IRC +10420. *Astrophysical Journal*, 228:771–779, March 1979.
- [71] G. E. Nedoluha and P. F. Bowers. VLA observations of 1612 and 1665 MHz OH masers associated with IRC +10420. *Astrophysical Journal*, 392:249–263, June 1992.
- [72] G. Neugebauer and R. B. Leighton. Two-micron sky survey. A preliminary catalogue. In *NASA SP-3047*, Washington, DC, 1969.
- [73] V. Ossenkopf, Th. Henning, and J. S. Mathis. Constraints on cosmic silicates. *Astronomy and Astrophysics*, 261:567–578, Aug 1992.
- [74] R. D. Oudmaijer. High resolution spectroscopy of the post-red supergiant IRC+10420. I. The data. *Astronomy and Astrophysics Supplement Series*, 129:541–552, May 1998.
- [75] Rene D. Oudmaijer, M. A. T. Groenewegen, H. E. Matthews, J. A. D. L. Blommaert, and K. C. Sahu. The spectral energy distribution and mass-loss history of IRC+10420. *Mon. Not. R. Astron. Soc.*, 280:1062–1070, June 1996.
- [76] Frank L. Pedrotti and Leno S. Pedrotti. *Introduction to Optics*. Prentice-Hall, 1987.
- [77] G. Perrin, V. Coude du Foresto, S. T. Ridgway, J. M. Mariotti, W. A. Traub, N. P. Carleton, and M. G. Lacasse. Extension of the effective temperature scale of giants to types later than M6. *Astronomy and Astrophysics*, 331:619–626, March 1998.
- [78] A. H. Pfund. An infrared spectrometer of large aperture. *J. Opt. Soc. Am.*, 14:337+, 1927.

- [79] A. Quirrenbach, D. Mozurkewich, J. T. Armstrong, D. F. Buscher, and C. A. Hummel. Angular diameter measurements of cool giant stars in strong TiO bands and in the continuum. *Astrophysical Journal*, 406:215–219, March 1993.
- [80] S. T. Ridgway, R. R. Joyce, D. Connors, J. L. Pipher, and C. Dainty. The dust shells of NML Cygnus and IRC 10420: Inner radius, temperature, and optical thickness. *Astrophysical Journal*, 302:662–674, March 1986.
- [81] F. Roddier. The effects of atmospheric turbulence in optical astronomy. *Progress in optics (North-Holland Publishing Co.)*, 19:281–376, 1981.
- [82] M. Ryle. A new radio interferometer and its application to the observation of weak radio stars. *Proc. R. Soc. A*, 211:351–375, 1952.
- [83] Frank H. Shu. *The Physical Universe*. University Science Books, Mill Valley, California, 1982.
- [84] J. Skilling and R. K. Bryan. Maximum entropy image reconstruction: general algorithm. *Mon. Not. R. Astron. Soc.*, 211:111–124, 1984.
- [85] P. Swanson, M. Colavita, A. Boden, G. Van Belle, and M. Shao. Keck interferometer. *American Astronomical Society Meeting*, 191:0912+, December 1997.
- [86] W. J. Tango and R. Q. Twiss. Michelson stellar interferometry. *Progress in optics (North-Holland Publishing Co.)*, 17:239–277, 1980.
- [87] M. C. Teich. Infrared heterodyne detection. *Proc. IEEE*, 56:37–46, 1968.
- [88] M. C. Teich. Field-theoretical treatment of photomixing. *Applied Physics Letters*, 14:201–203, 1969.
- [89] A. Richard Thompson, James M. Moran, and George W. Swenson, Jr. *Interferometry and Synthesis in Radio Astronomy*. John Wiley & Sons, 1986.
- [90] Robert N. Treuhaft, Stephen T. Lowe, Manfred Bester, William C. Danchi, and Charles H. Townes. Vertical scales of turbulence at the Mount Wilson Observatory. *Astrophysical Journal*, 453:522+, November 1995.
- [91] S. C. Unwin, J. W. Yu, and M. Shao. An introduction to the Space Interferometry Mission. *American Astronomical Society Meeting*, 191:2302+, December 1997.

- [92] Richard J. Wainscoat and Lennox L. Cowie. A filter for deep near-infrared imaging. *Astronomical Journal*, 103:332–337, January 1992.
- [93] Robert C. Weast, editor. *CRC Handbook of Chemistry and Physics*. CRC Press, 69<sup>th</sup> edition, 1988.
- [94] Mark G. Wolfire and Joseph P. Cassinelli. The temperature structure in accretion flows onto massive protostars. *Astrophysical Journal*, 310:207–221, November 1986.
- [95] R. R. Zappala, E. E. Becklin, K. Matthews, and G. Neugebauer. Angular diameter of IRC +10011 at 2.2, 10 and 20 microns. *Astrophysical Journal*, 192:109–112, August 1974.



# Colophon

This dissertation was created using the `ucthesis` document class and  $\LaTeX$  macro package (by L<sup>A</sup>mpport [53] and others [33]) for Donald Knuth's  $\TeX$  typesetting program [51]. The fonts used are from the Computer Modern family, designed by Knuth for use with  $\TeX$ . Despite the obsolete U.C. Berkeley formatting guidelines (responsible for the wasteful and unattractive double spacing throughout the official version of this document), one can see that  $\TeX$ , which was completed in 1986 [52], produces printed output of a quality still unrivaled by widely available commercial word processors.

The illustrations and graphs were created either in MetaPost, an extension of Knuth's METAFONT language by John Hobby, or in the Adobe PostScript page description language. Previewing of the text and illustrations was done with the `xdvi`, `ghostscript`, and `ghostview` programs, and final conversion to PostScript for printing was done using the `dvips` program. These programs were all run on a Sun SPARCstation under Sun's Solaris variant of the UNIX operating system.

It is interesting to note that even though every one of the programs used to produce this document is available free of charge, not once did any one of them crash or display any sort of errant behavior. Not coincidentally, no Microsoft products were used at any stage during the writing of this dissertation.

I would like to express my gratitude to the authors of the above mentioned software for the care which they put into their work, and for demonstrating that as far as software is concerned, the best things in life really are free.